UNIVERSITÀ DEGLI STUDI DI MILANO

DOTTORATO DI RICERCA IN INFORMATICA — XXXIV CICLO
DIPARTIMENTO DI INFORMATICA "GIOVANNI DEGLI ANTONI"

# Atrial Complex Networks in Endocavitary Recordings During Atrial Fibrillation

INF/01


Doctoral Dissertation of:
Muhamed Vila

Supervisor:
Prof. Roberto Sassi

Co-Supervisor:
Dr. Massimo Walter Rivolta

Doctorate School's Director:
Prof. Paolo Boldi



Academic Year 2020 – 2021

# Acknowledgements

First of all, I want to thank Prof. Roberto Sassi, head of the Biomedical Signal and Image Processing Lab, for providing me with the opportunity to pursue doctoral research and for his endless support during my studies. Likewise, I am thankful to Dr. Massimo Walter Rivolta who was always available to share his expertise and provide invaluable suggestions. Their guidance, patience, and trust have been incredibly valuable. I really appreciate the support of my ideas and the freedom they provided me.

I would like to thank all members of the MY-ATRIA (MultidisciplinarY training network for ATrial fibRillation monItoring, treAtment and progression) consortium, coordinated by Prof. Luca Mainardi, who enriched the presented research by stimulating discussions or by direct contributions. I am appreciative of all my former and current colleagues at the Department of Computer Science as well. Especially, I am deeply grateful to Prof. Adnan Tahirović for introducing me to the academic world and establishing my first connection with this research group.

Furthermore, I want to express my gratitude to Prof. Javier Saiz for hosting me at Valencia, and for his guidance with atrial computational models and simulations. The collaboration with them was the most pleasant and broadening experience.

The presented research would not have been possible without the close collaboration with the clinical partners. My gratitude goes to Prof. Dr. Federico Lombardi and Dr. Lorenzo Gigli from Milan, as well as Dr. Armin Luik from Karlsruhe for their extensive support during the years. I highly enjoyed discussing our ideas and this teamwork tremendously augmented the relevance of the presented research.

Of course, I would like to thankfully acknowledge the funding support from the European Union's Horizon 2020 research and Innovation program under the Marie Skłodowska-Curie grant agreement No. 766082.

In the end, my deepest gratitude goes to my wife Adna, parents Meliha and Haris, brothers Alija and Naim, and the rest of my family, for always believing in me and for their immense love and selfless support.

# Abstract

The incidence and prevalence of atrial diseases, particularly atrial fibrillation (AF), are today reaching pandemic proportions. Despite the considerable research efforts and progress regarding the understanding of mechanisms driving AF, the ability to treat it remains to be problematic. This thesis aims to contribute to reducing the burden of atrial arrhythmia from the technical point of view by processing the electrical signals coming from the heart. Specifically, the main objective of this thesis is to investigate signal processing techniques of invasive atrial signals that provide useful tools for helping electrophysiologists and technicians in the decision process during ablation treatment procedures or arrhythmia studies.

First, we proposed a new algorithm, for ventricular activity cancellation in atrial signals during AF. The methodology combines two common techniques, average beat subtraction (ABS) and interpolation, in a unified framework. Such framework was able to refine and improve the ventricular activity estimate, under the stationary assumption of the atrial activity in very short time windows. Briefly, the local atrial activity is first modeled with an autoregressive (AR) process, then the estimate is refined by maximizing the log maximum a posteriori of the atrial residual activity according to the fitted AR model. The new algorithm was tested on both synthetic and real atrial signals, and the performance was compared with the other five algorithms. The proposed algorithm outperformed all the others in terms of average root mean square error (0.038 vs 0.045 for interpolation; $p < 0.05$) on synthetic data. On real data, it outperformed two variants of ABS ($p < 0.05$) and performed similarly to interpolation when considering the high power residues left (both $< 3\%$), and the log-likelihood with the fitted AR model.

Second, we investigated a novel approach to atrial propagation pattern analysis based on directed networks (graphs). The networks are generated by processing signals collected during electrophysiologic studies. Network vertices represent the locations of the recordings and edges are determined by computing measures between recorded signals. The algorithm automatically identifies potential targets for treatment, such as rotational activity, spreading from electrode to electrode creating a closed loop, or focal activity, manifesting as a divergence of excitation from a given region. The method was tested on two subjects in sinus rhythm, seven in an experimental model of in-silico simulations, and ten subjects diagnosed

with complex atrial tachycardia who underwent catheter ablation. The algorithm correctly detected the electrical propagation of both sinus rhythm cases and all in-silico simulations. Regarding the clinical cases, arrhythmia mechanisms were identified in most of the cases (9 out of 10), i.e., cycles around the mitral valve, tricuspid valve, and figure-of-eight macroreentries.

Third, we proposed a recommender system, built as a solution to an optimization problem, able to suggest the optimal ablation strategy for the treatment of complex atrial tachycardia. The problem was designed on top of directed network mapping. The optimization problem modeled the optimal ablation strategy as that one interrupting all reentrant mechanisms while minimizing the ablated atrial surface. Considering the exponential complexity of finding the optimal solution to the problem, we introduced a heuristic algorithm with polynomial complexity. The proposed algorithm was applied to the data of i) 6 simulated scenarios including both left and right atrial flutter; and ii) 10 subjects that underwent a clinical routine. The recommender system suggested the optimal strategy in 4 out of 6 simulated scenarios. On clinical data, the recommended ablation lines were found satisfactory on 67% of the cases according to the clinician's opinion comparing to the actual treatment performed, while they were correctly located in 89% considering the mechanism in place. The algorithm made use of only data collected during mapping and was able to process them nearly real-time.

# Contents

# List of Figures

# List of Tables

# List of Abbreviations

**3D** . . . . . three-dimensional

**AF** . . . . . atrial fibrillation

**ABS** . . . . . average beat subtraction

**AFL** . . . . . atrial flutter

**AR** . . . . . autoregressive

**AV** . . . . . atrioventricular

**BSM** . . . . . body surface mapping

**CFAE** . . . . . complex fractionated atrial electrogram

**CS** . . . . . coronary sinus

**CT** . . . . . computed tomography

**CTI** . . . . . cavotricuspid isthmus

**DFS** . . . . . depth-first search

**DF** . . . . . dominant frequency

**EAM** . . . . . electroanatomic mapping

**ECG** . . . . . electrocardiogram

**ECGI** . . . . . electrocardiographic imaging

**EGM** . . . . . electrogram

**EP** . . . . . electrophysiology

**FIRM** . . . . . focal impulse and rotor modulation

**HPR** . . . . . high power residue

**IVC** . . . . . inferior vena cava

**LA** . . . . . left atrium

**LAT** . . . . . local activation time

**MAP** . . . . . maximum a posteriori

**MIL** . . . . . mitral isthmus line

**MSC** . . . . . magnitude-squared coherence

**MV** . . . . . mitral valve

**PV** . . . . . pulmonary vein

**PVI** . . . . . pulmonary vein isolation

**RA** . . . . . right atrium

**RF** . . . . . radio frequency

**RMSE** . . . . . root mean square error

**SA** . . . . . sinoatrial node

**SR** . . . . . sinus rhythm

**SRD** . . . . . sampling rate decimation

**STAR** . . . . . stochastic trajectory analysis of ranked signals

**SVC** . . . . . superior vena cava

**TV** . . . . . tricuspid valve

**VDR** . . . . . ventricular depolarization reduction

# 1 Introduction

## Contents



## 1.1 Motivation

Cardiovascular diseases are the leading cause of death globally, accounting for 32% of deaths worldwide, according to the World Health Organization [1]. Among these diseases, the incidence and prevalence of atrial diseases, particularly atrial fibrillation (AF), are today reaching pandemic proportions. AF is the most common

sustained cardiac arrhythmia in adults and is estimated to affect between 2% and 4% of the population, with a prevalence that increases with age, and reaches nearly 10% in octogenarians. As an age-related arrhythmia, a 2.3-fold rise is expected in the coming decades, largely owing to the extended longevity of the general population and intensifying search for undiagnosed AF [2]. With more than 11 million people affected in the European Union alone, AF represents a huge socioeconomic burden [3]. Besides the higher mortality and impaired quality of life, AF causes estimated healthcare costs of up to 2.6% of total healthcare expenditure in the European Union [4]. Therefore, it is of absolute importance to have valid therapeutic and preventive strategies for AF.

Despite the high incidence of AF, as well as the considerable research efforts and progress regarding the understanding of mechanisms driving AF, the ability to treat AF remains to be problematic. Patients suffering from severe atrial dysfunctions are usually eligible for pharmacological and/or interventional treatment called "catheter ablation". In the last few years, long-term success rates of ablation procedures have stood between 60% and 80% for paroxysmal AF and between 50% and 60% for persistent AF, depending on the treatment strategy [5]. Current international consensus has established the minimal acceptable 12-month AF-free rate off antiarrhythmic drugs after AF ablation at 40% [5]. Therefore, state-of-the-art therapy is not effective in the long run. Moreover, the development of post-ablational atrial flutter (AFL), which is another arrhythmia type, poses a particular problem [6].

In current clinical practice, ablation treatment of AF is mainly restricted to a standard procedure called "pulmonary vein isolation" (PVI). During this procedure, a certain region of atrial tissue, which has been observed to trigger AF, is destroyed in a controlled manner. However, recognizing that AF mechanisms may vary from patient to patient, recent progress indicates that the future treatment of AF should be tailored to the individual patient in an attempt to achieve an optimal success rate [7, 8]. Even though new technologies and techniques are emerging in recent years, these findings have not been consistent and it has become apparent that such a development will not be possible without further advancement of signal processing

techniques [7, 8]. Therefore, novel methods which can improve the understanding of AF mechanisms are required. Such methods could accurately guide the ablation to the specific atrial sites at which the arrhythmia originates or which represent arrhythmia substrates. Methods for propagation pattern analysis are of particular interest as they have the capability to point out the ectopic foci or identify reentrant activities, which are described as AF mechanisms. It is clear that patient-specific signal-guided approaches to ablation are expected to gain further importance in the future, requiring novel methods which can handle the strongly variable organization of AF signals, as well as the increasing number of simultaneously recorded signals.

## 1.2 State of the art of cardiac mapping

An engineering approach to the problem makes use of information technology and is able to deepen the understanding of AF mechanisms and provide a quantification of AF patterns and properties. Initially, AF has been widely described as a random phenomenon, but the arrival of more sophisticated atrial mapping techniques at the turn of the century has revealed the presence of an underlying order sustained by numerous factors such as cardiac muscle anatomy, electrophysiological properties, and autonomic innervation [9–11]. Signal processing methods have been thence applied to analyze atrial recordings, known as electrograms (EGM), to characterize the level of organization of the fibrillating atrium [12, 13]. The derived measures convey meaningful clinical information and can be of relevance for electrophysiologists. Cardiac mapping refers to identifying temporal and spatial distributions of cardiac electrical potentials during a particular heart rhythm. It aims to clarification of the cardiac rhythm mechanism, description of the activation propagation, and identification of a critical site of conduction to serve as a target for catheter ablation.

Novel strategies that are able to identify atrial regions associated with AF maintenance were reported as a result of recent developments in mapping tools and computational methods for advanced signal processing during AF [14, 15]. These novel tools, although mainly limited to research series, represent a significant step

forward towards the understanding of complex patterns of propagation during AF and the potential achievement of patient-specific AF ablation strategies for the near future. The rest of this section summarizes the state-of-art methodologies to map atrial activity during atrial arrhythmia, as well as the most recent ablation approaches aimed at increasing the specificity of ablation strategies, in a quest for a more personalized AF treatment.

### 1.2.1 Optical mapping

Cardiac optical mapping is a fluorescent imaging method to study electrical behavior and calcium handling in the heart (Figure 1.1). The introduction of optical mapping more than 2 decades ago enabled the visualization of atrial propagation dynamics with submillimeter resolution [16]. The use of voltage-sensitive dyes and high-resolution video imaging in isolated animal hearts has provided support for the hypothesis that AF may be driven by a single or a few high-frequency functional reentrant sources called rotors [17–19]. Rotors can be identified as a wave of excitation propagating around a point of the uncertain phase called a phase singularity (the tip of their rotational axis) [20]. Although the high spatio-temporal resolution of optical mapping would be the ideal scenario to map propagation dynamics during AF, current optical mapping strategies require the use of potentially toxic voltage-sensitive dyes that preclude their use for human in vivo studies. For this reason, in vivo optical mapping is still at the early development stages in experimental settings, and we are still far from achieving further technological advances for clinical application [21].

### 1.2.2 Sequential activation and voltage mapping

The analysis of the sequence of cardiac activation during a certain rhythm is referred to as activation mapping. Activation mapping became one of the essential diagnostic tools for guiding ablation procedures in cardiac arrhythmia [23]. It is performed by inserting a mapping catheter into the cardiac chamber and recording the electrical activity of the tissue at a given location. This process is sequentially repeated at

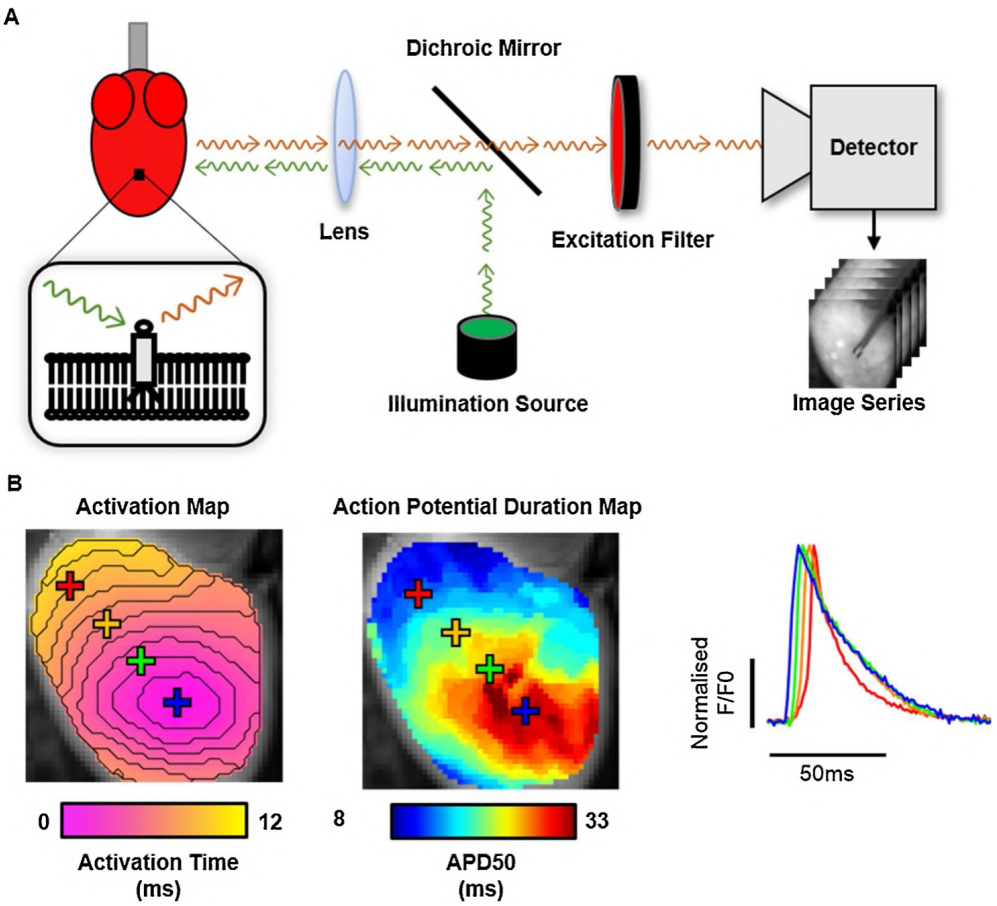


**Figure 1.1:** Cardiac optical mapping setup, data and analysis. **(A)** Schematic representation of a typical optical mapping setup for imaging a potentiometric dye loaded cardiac preparation (left). Inset shows the fluorescent indicator embedded within the cellular membrane. The potentiometric dye is excited by photons (green arrows) from an illumination source. This causes the release of fluorescent photons (red arrows) whose spectral properties depend on the transmembrane voltage. Fluorescent photons are filtered from the illumination photons and directed to a high-density imaging detector to produce a time series dataset. **(B)** Example of analyses possible from optical mapping datasets, including activation and signal morphology mapping (left panel). Right panel shows examples of the raw signals produced at each pixel of an optical mapping dataset, in this case optical action potentials from mouse ventricles. Y axis denotes normalised fractional fluorescence change (F/F0) from baseline fluorescence level (F0). Reprinted with permission from [22].

multiple sites in order to cover the entire cardiac chamber being mapped. Activation times are obtained from these measurements and are interpolated to construct a complete activation map of the heart chamber (see Figure 1.2). The activation map aids the doctors in localizing the target sites for catheter ablation. Even though this method works well in other types of arrhythmia, there are major drawbacks

to its application in AF. Identifying the point of local activation is significantly more challenging during AF, where double potentials and fractionated signals present great challenges [24]. Double potentials occur at sites of slow conduction or conduction block, and fractionated signals result from regions with heterogeneous conduction properties, such as fibrosis. Cardiac fibrosis is a process of pathological extracellular matrix remodeling, and regions of fibrosis often result in a reduced signal amplitude [25]. Therefore, fibrillatory activation maps are highly sensitive to different types of noise, and often disagree with other optical mapping modalities.

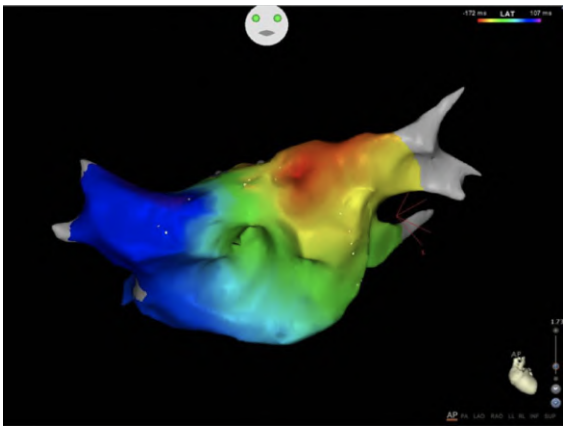

**Figure 1.2:** Activation map of an atrial tachycardia depicted on a left atrial geometry. The color-coded scale visualizes earlier activated regions (red/yellow color) in comparison to later activated (green/blue color) areas. In this case, an atrial focus is postulated at the roof of left atrium, adjacent to the left upper pulmonary vein. Reprinted with permission from [26].

Voltage mapping is a complementary approach that consists of evaluating the voltage amplitude of the recording in order to characterize areas involved in the generation and maintenance of arrhythmia (see Figure 1.3). Low atrial voltage amplitude is considered a marker for the presence of atrial fibrosis, which could play a key role in maintaining AF. As such, several clinical studies have described approaches for isolating areas of atrial low voltage, in an attempt to reduce arrhythmia recurrence after AF ablation. However, the methodology for defining low voltage areas has not been standardized and a clear voltage threshold for abnormality has never been histologically validated [27].

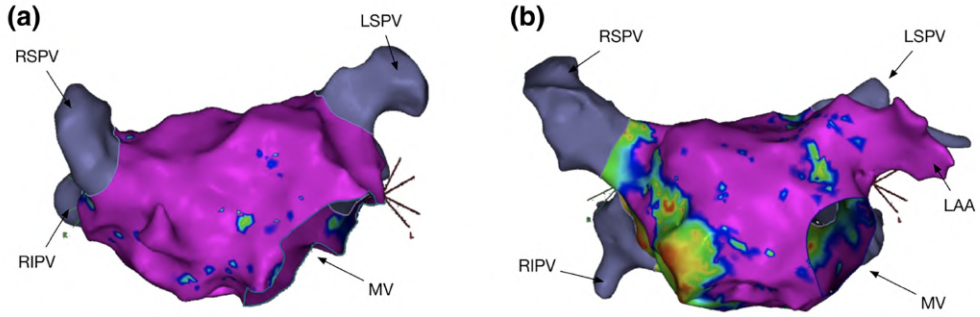


**Figure 1.3:** Two examples of high density left atrial voltage maps created during AF ablation. In both cases, purple colour represents EGM voltage $> 0.5$ mV. In panel **(a)**, minimal/no low voltage areas are present whereas in panel **(b)**, there are areas of low voltage affecting the left atrial septum and posterior wall. Reprinted with permission from [27].

### 1.2.3 Complex fractionated atrial electrograms

Almost two decades ago, Nademanee et al. proposed that areas with complex fractionated atrial electrograms (CFAE) may be critical for maintaining AF and their ablation might result in better clinical outcomes [28]. CFAEs were described as fractionated or continuous electric activity at short cycle lengths and may colocalize with potential drivers of AF (rotor cores) [29]. However, this method has been proven to be highly unspecific, as multiple functional and structural irregularities in the atria can lead to CFAEs that are irrelevant to AF mechanisms [30–32]. Such a lack of specificity has resulted in no incremental benefit when CFAEs are ablated after conventional PVI [33]. Moreover, CFAE ablation may increase the risk of atypical atrial flutter due to lesions that may generate the substrate for other atrial arrhythmias [34].

The improvement to CFAE analysis using nonlinear-based waveform similarity analysis termed similarity index has been proposed by Lin et al. [35]. The similarity index identifies the morphological repetitiveness of waveform patterns in fractionated signals, and the distribution of such index can be displayed on the 3D electroanatomical mapping system in real-time. The analysis enables the identification of different wave propagation patterns including rotational activity [36]. The authors observed that patients undergoing similarity index and phase mapping

(see next subsection) guided ablation showed higher termination rates and lower AF recurrences than patients receiving conventional CFAE ablation [36].

### 1.2.4 Spectral analysis and phase mapping

Spectral analysis is used to map the distribution of AF frequencies and localize the atrial areas with the highest activation frequencies [37], which usually coincide with the location of AF sources that maintain the arrhythmia [38]. The spectrum of a signal displays its power distribution in the frequency domain, and the frequency of the highest peak in the spectrum is called dominant frequency (DF), which is often used as a surrogate for the average activation rate at that location [39]. The real activation rate is usually difficult to measure in the time domain during AF, which makes spectral analysis particularly useful. However, frequency domain mapping produces time-averaged frequency information over space, thereby losing the ability to track temporal variations of the signal.

Phase mapping becomes a valuable tool in this regard, i.e. in detailing both spatial and temporal information (see Figure 1.4). Phase is a measure that describes where is a signal in its cycle of oscillation at a given point in time [40]. Analysis of phase changes over space provides information on the patterns of organization (repetitive activity) and helps to assess their stability in time and space. This approach can be particularly useful during fibrillation, as phase mapping can detect the phase singularities that organize the fibrillation, although optical mapping provides much higher resolution and accuracy in space and time [40]. Phase mapping forms the basis of numerous studies done in clinical electrophysiology that aimed to identify phase singularities and rotational activity. Those studies have adapted the Hilbert transformation as a practical way to derive the signal phase from the voltage-time series, and to demonstrate rotational drivers underlying AF maintenance [40–42]. Several non-invasive and invasive mapping approaches have used phase mapping to guide driver detection and ablation [36, 43, 44].

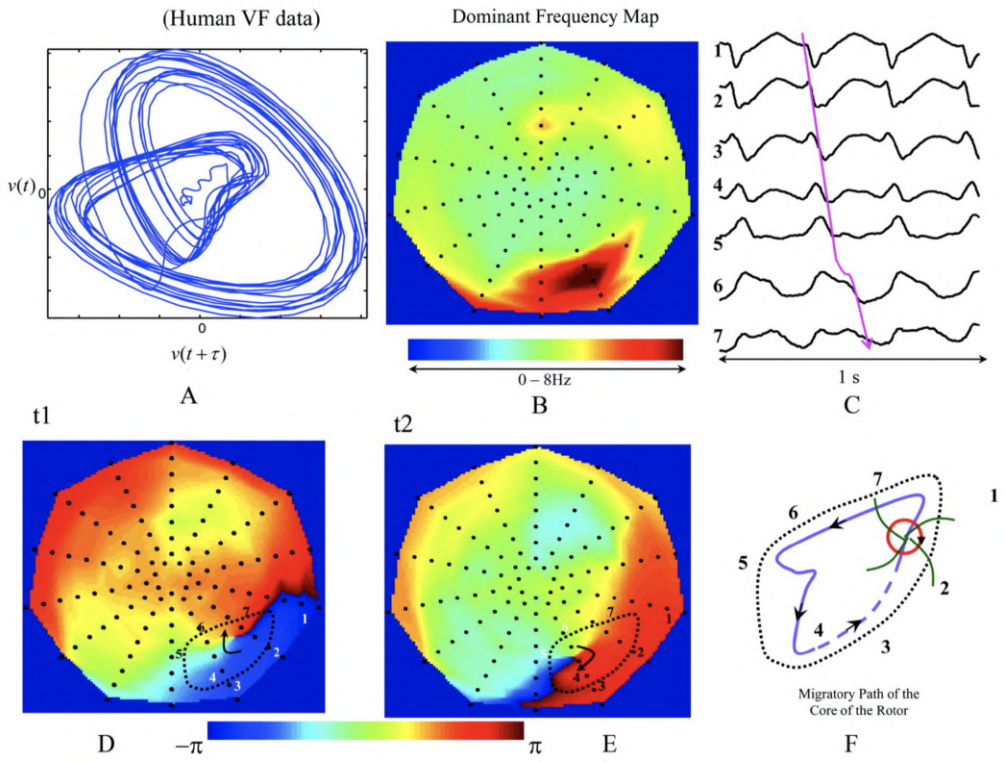


**Figure 1.4:** Top panel (**A** and **B**) shows the phase-space plot and the DF map of a human ventricular fibrillation segment. Bottom panel (**D** and **E**) shows 2 instances of the corresponding phase maps showing a phase singularity/rotor. Curved arrows show the direction of rotation. Top right panel (**C**) shows the EGM along the path of rotating phase pattern. Bottom right panel (**F**) shows the details on the migratory path of the rotor (1 through 7). Reprinted with permission from [40].

### 1.2.5 Simultaneous multielectrode mapping

Over the years, many studies have used high-density multielectrode patches to record epicardial (outer heart layer) electric activity from patients undergoing cardiac surgery [9, 45–47]. While this approach has the advantage of not requiring the use of toxic voltage-sensitive dyes, placing multielectrode patches on the epicardium requires open chest surgery, which is the main disadvantage. Furthermore, it is limited to small areas with limited spatial resolution when compared with optical mapping, but occasionally it is possible to identify rotational activities [47].

The other side approach is accomplished using multielectrode catheters in the form of "baskets" to obtain simultaneous endocardial (inner heart layer) recordings from many atrial locations [44]. These recordings are used to generate activation movies of the atrial electric activity after considerable processing and

interpolation [48]. The main advantage of this approach is that it enables real-time assessment of changes in driver activity during the ablation procedure. However, many limitations need to be considered, such as artifacts, a ventricular activity that contaminates atrial recordings, suboptimal electrode-tissue contact, poor spatial resolution, amount of extrapolation in the presence of poor quality data, and phase interpolation bias.

### 1.2.6 Focal impulse and rotor modulation

Focal Impulse and Rotor Modulation (FIRM) is a prototypical system to guide ablation, based on the premise that AF is sustained by rotors and/or focal sources, which were sufficiently stable in space [44, 49, 50]. FIRM maps using basket multielectrode mapping catheters, and its workflow is shown in Figure 1.5. The Conventional Ablation for Atrial Fibrillation With or Without Focal Impulse and Rotor Modulation (CONFIRM) trial reported AF suppression in 82% of patients, much higher than the control group treated by conventional ablation techniques [33]. Even though the initial results and long-term follow-up experience reported high success as compared to conventional strategies, subsequent studies using FIRM have demonstrated varying success rates [51].

### 1.2.7 Electrographic flow mapping

Electrographic flow mapping also uses recordings from panoramic basket catheter but is analyzed using the Horn–Schunck optical flow algorithm to calculate the average electrical flow of propagation of action potentials that is proposed to be resistant to noise and artifacts [42]. Figure 1.6 shows a schematic description of the individual steps to derive electrographic flow from atrial signals. Applied retrospectively to FIRM data, the approach has been used to identify FIRM regions that may be of higher or lower importance, including sites where targeted ablation terminated AF [52].

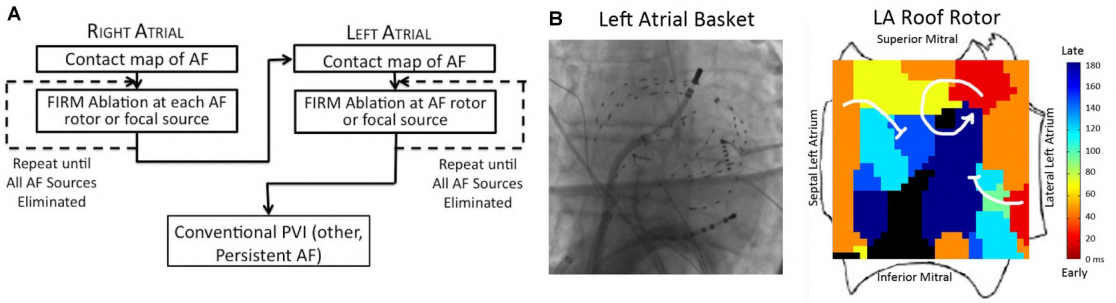


**Figure 1.5:** **(A)** Workflow for FIRM-guided ablation of AF. **(B)** Typical basket placement and results from FIRM-guided ablation. Basket placed in left atrium, with resulting FIRM map showing AF rotor at roof with surrounding spiral arms disorganizing and fusing with the fibrillatory milieu (blocked arrows) and rotor precession within a limited area on successive cycles (not shown). Reprinted with permission from [49].

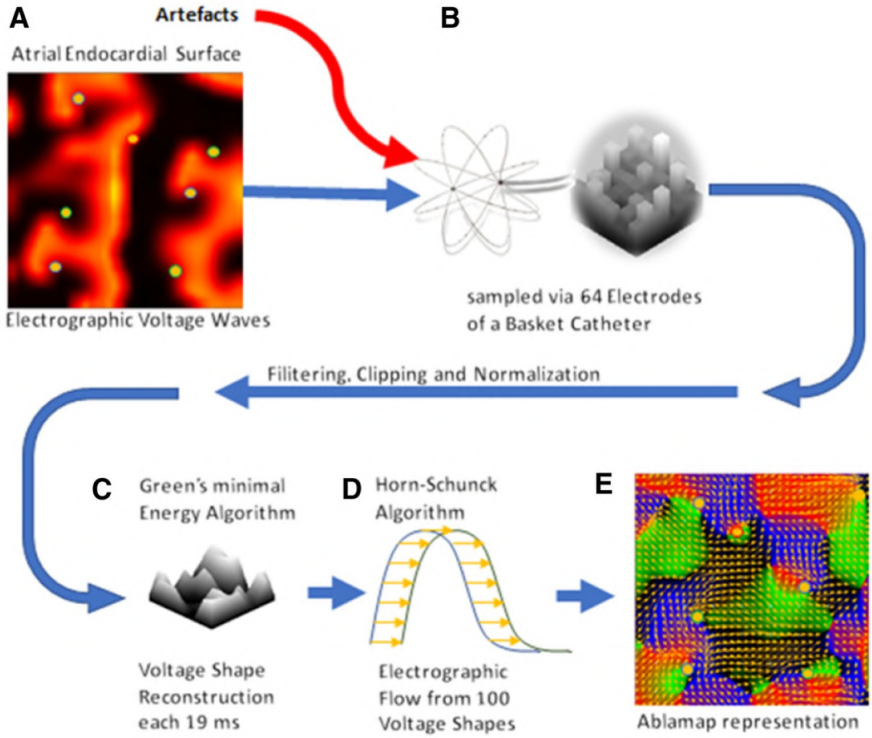


**Figure 1.6:** The Principle of Electrographic Flow Mapping. **A** Sources of excitation (yellow spots) induce electrographic voltage waves (orange). **B** EGMs recorded via 64-pole basket catheter sampled and filtered to reduce artifacts. **C** Each 19 ms reconstruction of the voltage shape with Green's Minimal Energy algorithm. Shapes resemble optical maps as obtained with voltage sensitive dyes. **D** 100 subsequent shapes are processed to an electrographic flow map (Horn-Schunck method). **E** Each electrographic flow map is automatically analyzed with respect to active sources of electrographic flow, source characteristics (rotor, focal impulse) and passive rotors. Reprinted with permission from [52].

### 1.2.8 Spatiotemporal dispersion mapping

Another approach to atrial recordings analysis has suggested that fractionation occurring non-simultaneously at neighboring electrode locations (time dispersion) and organized in properly defined clusters (spatial dispersion) may indicate the presence of an underlying source of AF [53]. After mapping with a multielectrode catheter, sequentially positioned in various atrial regions, the data are visually analyzed to identify atrial locations displaying spatiotemporal dispersion on signals. Areas with dispersion have been defined as clusters of signals, either fractionated or non-fractionated, that display inter-electrode time and space dispersion at a minimum of three adjacent bipoles such that activation spreads over all the AF cycle length (see Figure 1.7). Seitz et al. tested this approach in a study that included 105 patients undergoing AF ablation. The ablation was performed only in regions displaying dispersion criteria during AF, which terminated in 95% of patients, but mostly with initial conversion to AFL (85%). [53].

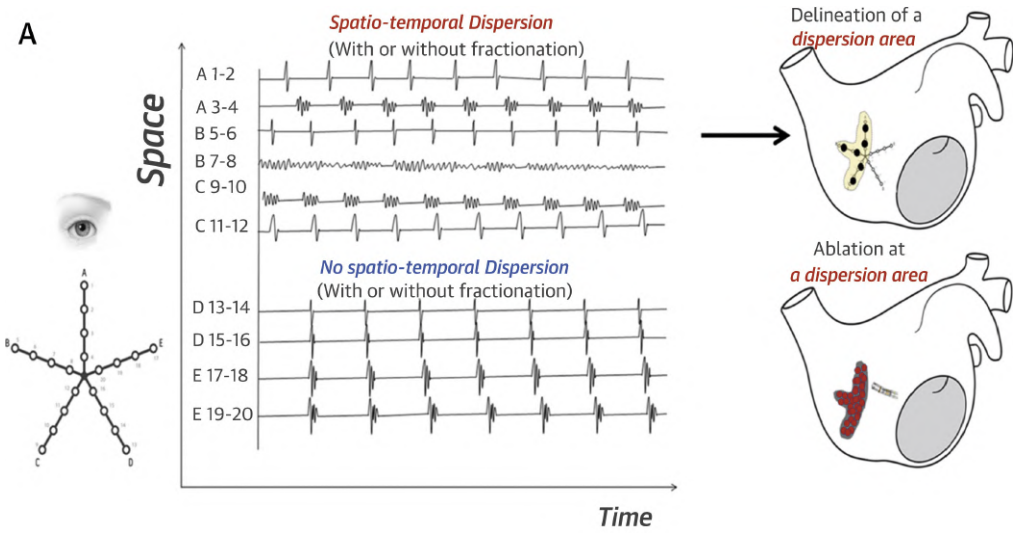


**Figure 1.7:** Dispersion areas are defined and delineated via a mapping approach. A 1-2, A 3-4, B 5-6, B 7-8,C 9-10 and C 11-12 display spatiotemporal disperiosn. Reprinted with permission from [53].

### 1.2.9 Stochastic trajectory analysis of ranked signals

Stochastic trajectory analysis of ranked signals (STAR) analyzes data from multiple individual wavefront trajectories to identify regions of the atrium that most often precede the activation of the neighboring areas. This is done by creating a statistical model from many hundreds of activations, ranking the regions of the atrium by the amount of time that their activations precede those of the adjacent regions (Figure 1.8) [54].

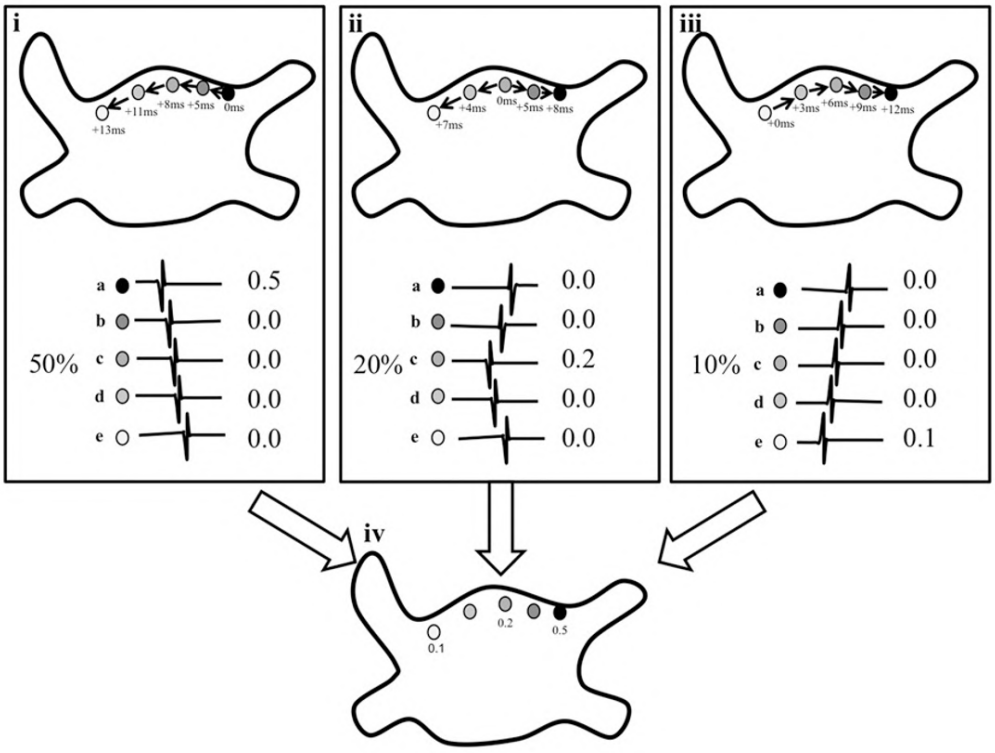


**Figure 1.8:** Simplified method of calculating a STAR map. Five signal pairs are shown, (a-e), and the signals derived from each electrode are shown below. Three representative patterns which together comprise 80% of the total recording time are shown (**i-iii**): (**i**) accounting for 50% of the time electrode a is leading all other electrodes, (**ii**) a different activation sequence is illustrated, with electrode (c) leading, accounting for 20% of the time, (**iii**) is another activation sequence where electrode (e) leads, 10% of the time. Each electrode has a value associated with it based on the proportion of time that electrode is seen as "leading" its closest associated electrode as shown in (iv). A final process combines these data and superimposes these on a combined map, highlighting the leading electrodes. Reprinted with permission from [54].

### 1.2.10 Real-time electrogram analysis for drivers of AF

Real-Time Electrogram Analysis for Drivers of Atrial Fibrillation (RADAR) system sorts and compiles signals from electroanatomic maps created with standard mapping equipment, using signals from the coronary sinus as a reference [55]. This approach bins localized recordings at several hundred locations with a similar coronary sinus signal pattern into one global map to calculate 3D conduction vectors and a driver density map. This is repeated for all observed coronary sinus patterns. Multiple maps are fused probabilistically based on the repetition of rotational or focal drivers at the border of low-voltage areas to highlight presumed AF drivers, which are targeted for ablation.

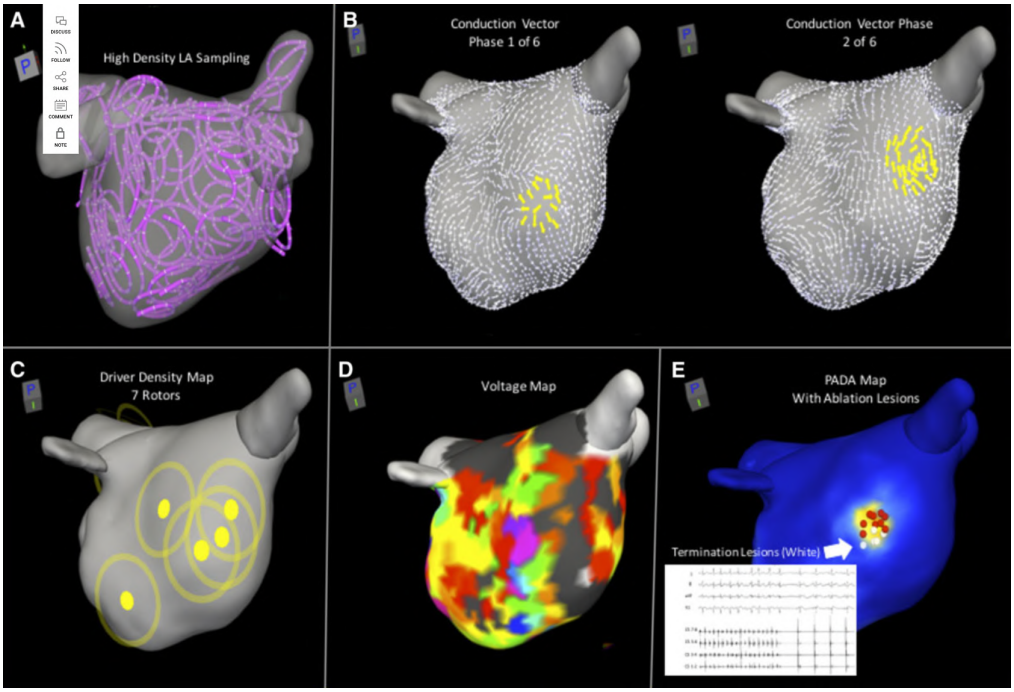


**Figure 1.9:** Creation of probabilistic atrial driver assessment (PADA) map. **A**, High-density EGM, voltage, and location information are collected throughout the left atrium using standard mapping equipment. Individual conduction vector maps for each phase (**B**) are combined to yield a driver density map (**C**). A voltage map collected during AF (**D**) is incorporated with this information to output the PADA map (**E**). AF was successfully terminated with ablation (red and white dots) at the highlighted driver domain on the posterior wall in this patient. Reprinted with permission from [55].

### 1.2.11 Body surface mapping and electrocardiographic imaging

The body surface mapping (BSM) is a noninvasive methodology that has recently gained visibility for the analysis of activation patterns during atrial arrhthmia [56, 57]. In the study by Guillem et al., a multi-electrode vest that covered the whole patient's torso (Figure 1.10) was used, along with simultaneously recorded endocavitary signals at several locations. They selected segments without ventricular activity after adenosine infusion or applied ventricular activity subtraction if such intervals were not found. Comparing endocavitary and surface DF maps, they demonstrated that high-frequency sources could be reflected on a small area of the body surface close to the atrium [56]. Another study used phase mapping and filtered the endocavitary signals with a narrow 2-Hz band-pass around the highest DF filtering to improve the detection of stable rotors (8.3% of the time before filtering and 73% after filtering) [57].

BSM outputs potentials on the body surface, not on the heart. In contrast, the electrocardiographic imaging (ECGI) mapping system provides estimated epicardial signals in relation to the heart's anatomy (see Figure 1.10). This technology enables to investigate non-invasively different patterns of cardiac activation that may be relevant for the understanding of AF dynamics [58, 59]. The approach uses hundreds of electrodes distributed throughout the patient's torso, in combination with computed tomography (CT) imaging. The body surface potentials recorded by the electrodes and the geometric information provided by computed tomography are combined using sophisticated computer back-extrapolation (electrocardiographic inverse solution) to deduce electrical activity on the heart surface [60, 61]. Both rotors and focal sources can be observed using ECGI [62].

## 1.3 Scope and aims of the thesis

The alternatives to analyzing intracardiac mapping data are practically unlimited. This thesis aimed to contribute to the understanding of atrial arrhythmia from the technical point of view by merging signal processing and network theory to tackle

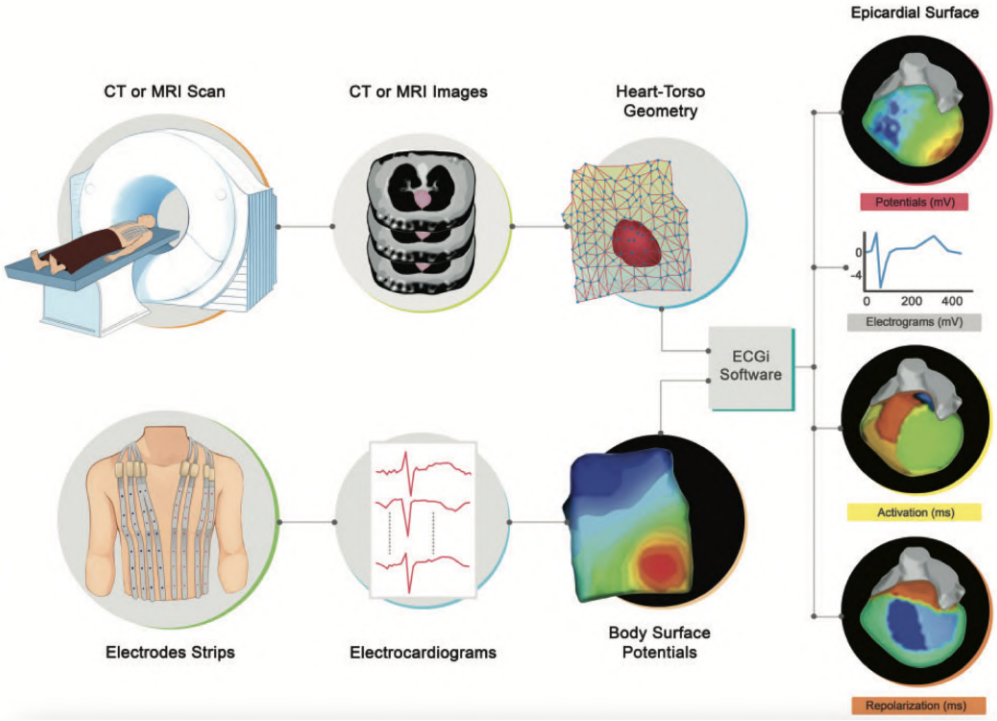


**Figure 1.10:** The ECGI procedure. Body surface potentials are recorded from several electrodes. The patient-specific heart-torso geometry is obtained from thoracic CT or MRI scan. The data are combined using mathematical algorithms to reconstruct epicardial potentials and EGMs on the heart surface. Maps of epicardial activation and recovery can be further derived from the EGMs. Reprinted with permission from [63].

the problem. Specifically, the main objective of this thesis is to provide useful tools, based on network theory, for helping electrophysiologists and technicians in the decision process during arrhythmia studies and ablation procedures.

In order to achieve this goal, the concept of network needs to be introduced in the context of atrial electrical propagation. A common strategy to build a network is to consider the atrial activity organization, i.e., the coupling between the recordings measured at different atrial sites. The coupling can be described in terms of various characteristics of the electrical activity of the atria, such as the repeatability or regularity of the atrial activations, the correlation, and synchronicity among atrial signals recorded in different locations, or the similarity of the wave morphology. However, the performance and interpretation of all these signal processing approaches used on atrial signals get highly degraded by far-field ventricular activity that might be overlapped with the signal of interest, i.e., the

atrial one. Therefore, the most important preliminary step for almost all further analyses of atrial signals is the cancellation of the ventricular activity. Although ventricular activity cancellation is a well researched topic in the body surface signals, the conventional approaches to the problem still have some hefty problems when applied to intracardiac data, especially in AF patients. Hence the first major goal of this thesis was to improve on the current ventricular activity cancellation techniques. This was done by exploring a novel algorithm, based on combining the two most common approaches in a unified framework, with the goal of taking advantage of their pros, while trying to avoid their cons.

After the improvements in signal preprocessing, the next major goal was to construct networks (mathematical structures also known as graphs) that characterize the cardiac propagation pattern during atrial arrhythmias. The networks were generated by processing atrial signals (EGMs) collected in a hospital during an electrophysiology (EP) study by catheters (with electrodes) positioned at the different regions of the atria. Network vertices represented the locations of the recordings and edges were determined by interrelationship measures between two nodes, computed from the recordings. Atrial conduction paths could be identified by examining the networks. During the analysis, the algorithms from network theory could be employed to automatically identify potential targets for treatment, such as rotational activity, spreading from electrode to electrode creating a closed loop, or focal activity, manifesting as a divergence of excitation from a given point (region). We analyzed the robustness of this approach's potential with respect to the existing state-of-the-art methodology used in clinics. We validated the applicability of the network-based methodology in both in-silico and clinical settings, in various simulated atrial models of different heart rhythms, and in various clinical cases.

The final goal of the thesis was to develop automated computer-aided technology in planning the optimal ablation strategy. We proposed a recommender system, built as a solution to an optimization problem, able to suggest the optimal ablation strategy for the treatment of complex atrial arrhythmia. The approach is tailored to the individual patient, based on the networks generated from the data collected

during the EP study. The optimization problem modeled the optimal ablation strategy as that one interrupting all drivers of the arrhythmia while minimizing the ablated atrial surface. Considering the exponential complexity of finding the optimal solution to the problem, we introduced a heuristic algorithm with polynomial complexity.

## 1.4 Thesis organization

The work presented in this thesis consists of six chapters.

- Chapter 1 is the introductory chapter.
- Chapter 2 gives a brief introduction to cardiac anatomy and electrophysiology. The atrial arrhythmias flutter and fibrillation are introduced and interventional therapeutical approaches are presented.
- Chapter 3 provides an overview of ventricular activity cancellation, which is an important step in preprocessing atrial signals. A novel method is introduced and compared to state-of-the-art methods. The preliminary contributions from this chapter were presented at the 41st Annual International Conference of the IEEE Engineering in Medicine and Biology Society[1]. The initial method was extended and compared in more detail with the most common cancellation strategies, which presents the further contribution from this chapter, also included in a peer-reviewed publication under preparation[2].
- Chapter 4 presents and evaluates a method to characterize the atrial wave propagation based on network theory. The main contributions from this chapter were published in a peer-reviewed journal[3]. The additional application

[1]M. W. Rivolta, R. Sassi, M. Vila. Refined Ventricular Activity Cancellation in Electrograms During Atrial Fibrillation by Combining Average Beat Subtraction and Interpolation. Annu Int Conf IEEE Eng Med Biol Soc. 2019 Jul;2019:24-27.

[2]M. Vila, M. W. Rivolta, L. Gigli, F. Lombardi and R. Sassi. Maximum a Posteriori Estimate of Ventricular Activity in Electrograms During Atrial Fibrillation. Manuscript in preparation.

[3]M. Vila, M. W. Rivolta, G. Luongo, L. A. Unger, A. Luik, L. Gigli, F. Lombardi, A. Loewe and R. Sassi. Atrial Flutter Mechanism Detection Using Directed Network Mapping. Front Physiol. 2021;12:749635. Published 2021 Oct 26.

in a simulated AF scenario was presented at the 43rd Annual International Conference of the IEEE Engineering in Medicine and Biology Society[4].

- Chapter 5 presents and evaluates a method to automatically recommend a patient-specific ablation treatment based on network theory (extending the method from Chapter 4). The original idea was presented as proof-of-concept at the Atrial-Signals 2021 conference[5]. The main contributions from this chapter are in preparation for a peer-reviewed publication which will be submitted shortly[6].

- Chapter 6 summarizes the findings presented in this thesis.

[4]M. Vila, S. Rocher, M. W.Rivolta, J. Saiz, R. Sassi. Directed Network Mapping Approach to Rotor Localization in Atrial Fibrillation Simulation. Annu Int Conf IEEE Eng Med Biol Soc. 2021 Nov;2021:730-733.

[5]M. Vila, M. W. Rivolta, G. Luongo, A. Loewe, R. Sassi. Directed Network Mapping Hints the Ablation Strategy for Atrial Flutter: a Proof of Concept. Abstract. In Atrial Signals 2021, 23-25 September 2021, Karlsruhe 2021 (pp. 16-16). Karlsruher Institut für Technologie (KIT).

[6]M. Vila, M. W. Rivolta, C. A. Barrios Espinosa, L. A. Unger, A. Luik, A. Loewe and R. Sassi. Recommender System for Ablation Lines to Treat Complex Atrial Tachycardia. Manuscript in preparation.

# 2
# Medical Fundamentals

## Contents



The basic medical fundamentals that are essential to understand and put into context the studies presented in the thesis are presented in this chapter. Firstly, brief descriptions of cardiac anatomy, physiology, and electrophysiology are summarized. Then, the atrial arrhythmias flutter, and fibrillation are introduced, and state-of-the-art interventional treatments are presented.

## 2.1 Cardiac anatomy and physiology

The heart is a muscular organ that continuously pumps oxygenated blood from the lungs to the tissues throughout the body, and transports the blood with carbon dioxide away from the tissues toward the lungs. Figure 2.1 shows the anatomy of the heart with the major blood vessels. The heart is made up of four chambers,

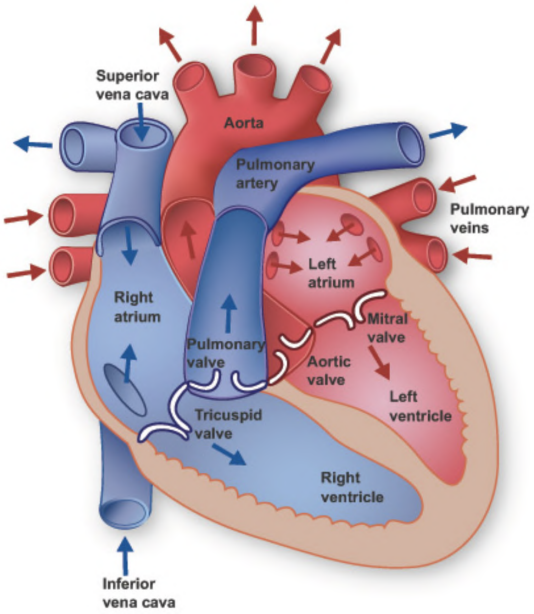


**Figure 2.1:** Anatomy of the human heart. Reprinted with permission from [64].

that are anatomically and functionally divided into the right and the left halves by the muscular wall called the septum. Each half consists of an atrium and a ventricle that are connected through valves controlling the blood flow. The ventricles fulfill the pumping function of the heart by expelling blood from the heart towards the peripheral beds within the body and lungs. Blood is carried from the heart to the rest of the body through a complex network of arteries and capillaries. Blood is returned to the heart through veins. The atria, which are the focus of this thesis, collect the blood flowing from the veins and entering the heart.

Deoxygenated blood enters the right atrium (RA) through the inferior vena cava (IVC), the superior vena cava (SVC), as well as the blood from the heart itself through the coronary sinus (CS). The RA ejects and passes blood through the tricuspid valve (TV) into the right ventricle. The right ventricle expels into the lungs where the blood is oxygenated. Coming from the lungs, the blood is collected through the (normally) four pulmonary veins (PVs) in the left atrium (LA). The LA ejects and passes blood through the mitral valve (MV) into the left ventricle. The left ventricle pumps blood out of the heart to the rest of the body through the aorta. The circulatory loop is closed as the blood comes back from the body to the RA.

## 2.2 Cardiac electrical system

Electrical impulses from the heart muscle (myocardium) cause the heart to contract. The activity of the heart, described as a sequence of muscle contractions and relaxations, corresponds to a series of electrical events. In electrical terms, the contraction and relaxation phases are referred to as depolarization and repolarization, respectively. When any part of the electrical conduction system of the heart is activated, its tissue gets depolarized and it needs to be repolarized before being activated again. Before the repolarization, the tissue is said to be refractory.

In a healthy heart, this process is coordinated by electrical impulses originating in the sinoatrial (SA) node, located high in the RA near the SVC (see Figure 2.2). The impulse leaves the SA node and spreads radially across both atria through the muscle fibers, causing them to contract. After propagating throughout the atria, the impulse reaches the atrioventricular (AV) groove, the structure to which the valve rings are attached and that separates the atria from the ventricles. This structure is electrically inert and acts as an insulator, thus the electrical impulse would be prevented from reaching the ventricles if not for the specialized AV conducting tissues: the AV node and the bundle of His (see Figure 2.2).

As the electrical impulse enters the AV node, the conduction velocity of the impulse is slowed significantly, causing a delay. After passing through the AV node, the conduction velocity increases again as the electrical impulse enters the His bundle, which delivers the impulse on the ventricular side of the AV groove. Once on the ventricular side, the electrical impulse follows the His bundle as it branches into the right and left bundle branches. Branching of the Purkinje fiber continues distally to the furthermost reaches of the ventricular myocardium. The electrical impulse is thus rapidly distributed throughout both the left and the right ventricle simultaneously. This completes the electrical cycle of one heartbeat.

Hence the heart's electrical system is designed to organize the sequence of myocardial contraction with each heartbeat. The heart rate is directly controlled by the rate of impulses from the SA node, and this is referred to as normal Sinus Rhythm

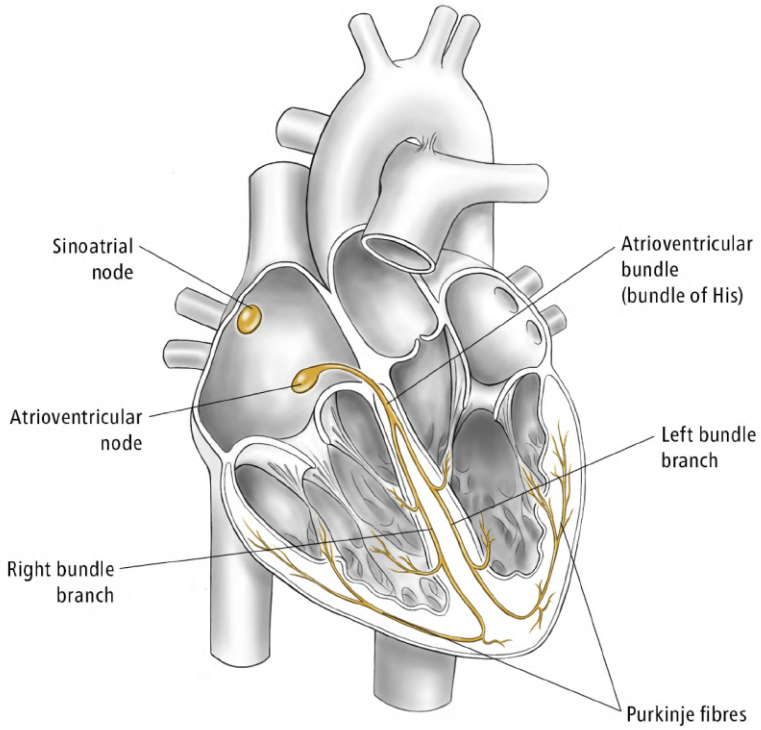


**Figure 2.2:** Cardiac conduction system. Reprinted with permission from [65].

(SR). The delay of the impulse in the AV node causes a sufficient time difference between the atrial and the ventricular contractions to allow complete atrial emptying.

The cardiac cycle, as represented by the electrocardiogram (ECG), measured on the body surface, consists of several characteristic waves which are shown in Figure 2.3. During SR, the beginning of the cardiac cycle is denoted P wave, which reflects the depolarization of the atria. The subsequent depolarization of the ventricles is denoted QRS complex, which at the same time masks the atrial repolarization. At the end of the cardiac cycle, the T wave occurs which reflects ventricular repolarization.

## 2.3 Atrial flutter

Atrial flutter (AFL) is the second most prevalent heart rhythm disorder after atrial fibrillation (AF) [67]. Instead of that every heartbeat starts with a single electrical impulse from the SA node, this type of arrhythmia is described with a consistent excitation pattern, perpetuated around a large central obstacle, which can be an

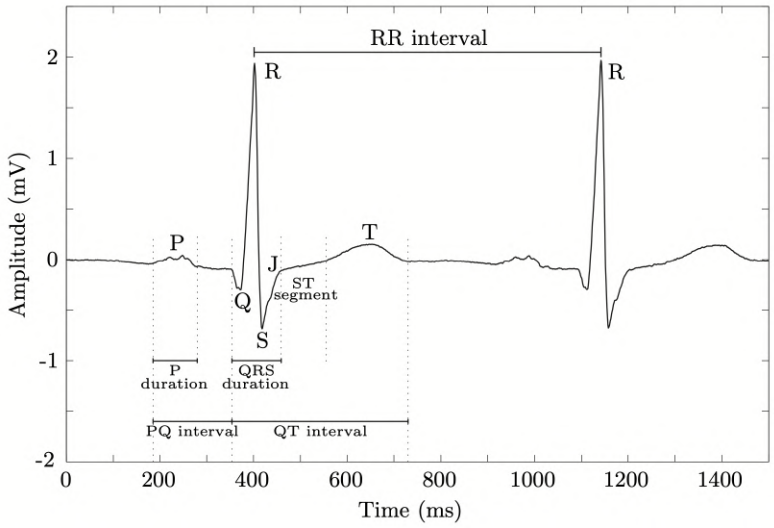


**Figure 2.3:** The cardiac cycle in sinus rhythm as observed in the ECG. Reprinted with permission from [66].

anatomical structure, unexcitable scar tissue, or a functional line of block [7]. With the cycle length between 250 ms and 135 ms [68], such a fast rhythm cannot be sustained by the ventricles, meaning a 2:1 or 3:1 conduction block at the AV node is frequently observed. The most common type of AFL is a typical circuit located in the RA, involving the cavotricuspid isthmus (CTI) bounded by the TV and the IVC (Figure 2.4) [7]. Therefore, ablation at this critical portion of the path is the first-line approach for termination [7].

However, the circuits involved in atypical AFL are highly variable and involve a range of anatomical boundaries, possible in both RA and LA (Figure 2.5). For the maintenance of the arrhythmia in these atypical cases, different anatomical obstacles (e.g., the MV), scars from previous cardiac surgery, regions electrically isolated by ablation (e.g., the PVs) and arrhythmogenic substrates can be responsible [7]. Despite the variety of mechanisms, high success rates of AFL ablation were reported in the range of 88 to 100% [69].

There is a close interrelationship between AFL and AF. The presence of AFL usually suggests an underlying predisposition to AF, which will eventually be identified in most of these patients [70]. Indeed, AFL is generally initiated through a transitional phase of AF [71]. Furthermore, studies reported an incidence rate

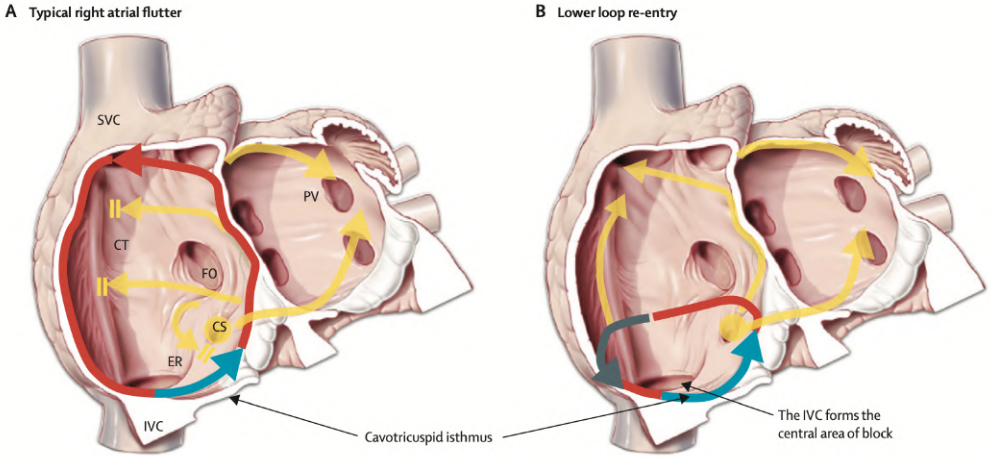


**Figure 2.4:** Anatomical circuits of AFL in the RA. The atrioventricular valves that sit anteriorly (in front) have been removed for clarity. **A**, Typical flutter involves a circuit around the TV. **B**, Lower loop reentry involves a smaller circuit around the IVC. Red arrows represent the activation path for each circuit. The blue arrows indicate the CTI representing the crucial narrowest part in the circuits. Yellow arrows indicate passive activation wavefronts not driving the flutter. The dark gray arrow in **B** indicates a zone of slow conduction allowing to sustain the flutter along the shorter circuit compared to **A** where the crista terminalis (CT) forms a line of functional block. Reprinted with permission from [7].

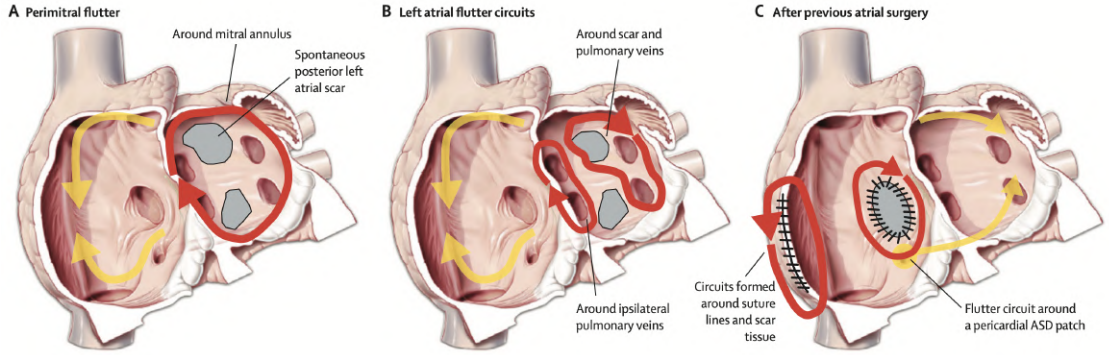


**Figure 2.5:** Atypical flutter circuits. Red arrows indicate the activation path for each driving circuit. Yellow arrows indicate passive activation wavefronts not driving the flutter. Gray areas represent unexcitable scar tissue. **A**, Perimitral flutter involves a circuit around the MV. **B**, Flutter circuits around obstacles formed by the PVs. **C**, Flutter circuits around suture lines and scar tissue from previous surgery. Reprinted with permission from [7].

of 5 to 40% of AFL following ablation for AF, with a strong dependency on the type of ablation [72]. Pharmacological therapy is often ineffective in treating AFL, and catheter ablation (see Section 2.8) is regarded as the most important

therapeutic option for patients [7].

## 2.4 Atrial fibrillation

AF is the most common sustained arrhythmia characterized by a complete loss of regular atrial activity, where several impulses of varying origin spread throughout the atria and cause uncoordinated atrial contractions. It is a progressive disease usually starting with short silent paroxysms transitioning to longer and symptomatic episodes [73]. According to the duration of its episodes, it is classified as paroxysmal, persistent, long-standing persistent and permanent AF [2].

The underlying mechanisms of AF are complex and not yet completely understood. Numerous factors including genetic predisposition, structural modification and fibrotic inclusions, progression of cardiac diseases, inflammation, dysfunction of the autonomic nervous system paired with electrophysiological abnormalities of the atria and PVs, are considered to favor the initiation and sustaining of fibrillation. Different studies have shown evidence for several (in parts contradicting) theories.

So far, three main theories on AF mechanisms have evolved. The multiple wavelet hypothesis was introduced by Moe et al., stating that AF is generated by parallel existing microreentry circuits propagating on varying routes throughout both atria, randomly activating the atrial tissue and thus leading to the complex electrical patterns observable during AF [74]. The maze operation for therapy of AF was generated based on this model [75]. The second theory was developed as Haissaguerre et al. observed that AF is often triggered by focal sources [76]. Focal triggers were observed most often in the LA close to the PVs, but other origins were also found, such as the SVC. Ablation of these focal sources terminated AF, and this theory became the rationale for the current ablation strategy, the PVI [7, 77]. The third theory is based on the concept of rotors, which are the sustained high frequency functional reentrant drivers, appearing in presence of an appropriate heterogeneous AF substrate [11]. This mechanism is more probable when AF is maintained for relatively long time periods, which results in a more complex arrhythmogenic substrate due to atrial remodeling, i.e., the shortening of

action potential duration and refractory period [5]. Figure 2.6 illustrates various hypotheses and proposals concerning the mechanisms of AF.

After identification of triggers inside the PVs, their isolation has become the standard first line approach for any catheter ablation. It can be achieved with both radiofrequency ablation or cryoballoon application [5, 7]. Due to limited success rates in the treatment of patients with persistent AF, numerous additional approaches were suggested, as previously described in Section 1.2 of Chapter 1. Despite a large variety of ideas, the optimal treatment strategy for patients suffering from AF still has to be found. Indeed, the detection of the mechanisms underlying AF is one of the most challenging research topics in current electrophysiology.

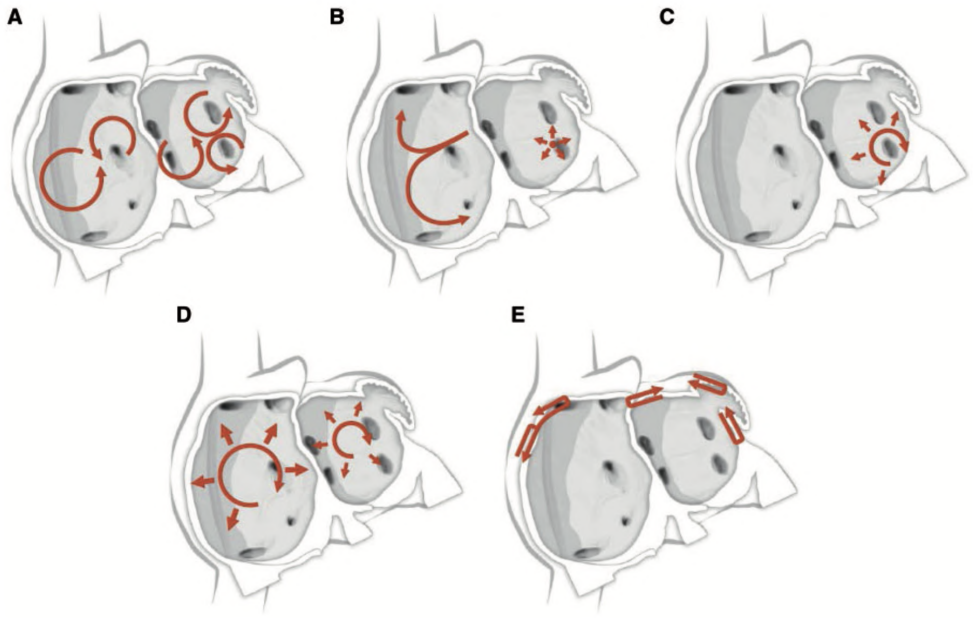


**Figure 2.6:** Schematic drawing showing various hypotheses and proposals concerning the mechanisms of AF. The atrioventricular valves that sit anteriorly (in front) have been removed for clarity. **A**, Multiple wavelets hypothesis. **B**, Rapidly discharging focal triggers. **C**, Single reentrant circuit with fibrillatory conduction. **D**, Functional reentry resulting from rotors or spiral waves. **E**, AF maintenance resulting from dissociation between epicardial and endocardial layers, with mutual interaction producing multiplying activity that maintains the arrhythmia. Reprinted with permission from [5].

## 2.5 Electroanatomic mapping systems

Electroanatomic mapping (EAM) systems have been introduced into clinical electrophysiology over two decades ago [78]. They are utilized to precisely manage the diagnostic and decision processes during ablation interventions in patients with suspected or documented history of cardiac arrhythmias. EAM systems use multielectrode catheters, inserted into the cardiac chambers guided through a blood vessel, to record cardiac electrical activity and perform programmed cardiac electrical stimulation. In principle, EAM system consists of three main parts: (i) non-fluoroscopic catheter localization, (ii) calculation and three-dimensional (3D) display of electrical activation sequences (activation maps) and voltage information (voltage maps) within the cardiac anatomy, and (iii) 3D display of the anatomy of a heart chamber from serially generated catheter localization information. EAM systems additionally also allow to display catheter positions and stored recordings together with anatomic information of the heart chamber generated through other imaging modalities (e.g., computed tomography or magnetic resonance imaging) [79]. These systems minimize the patient risk by applying minimally invasive methods instead of open-heart surgery, as well as the minimal radiation exposure required to localize equipment in the heart.

At present, there are three major commercially available systems that rely on magnetic-based or impedance-based localization: CARTO® 3 (Biosense Webster), EnSite Precision™(Abbot), and RHYTHMIA HDx™(Boston Scientific). On the basis of magnetic and/or impedance measurements, these systems display the position of any electrophysiology catheter in 3D space. An example of such a catheter localization display is shown in Figure 2.7. Although advances in technology have facilitated the practice of EAM to identify areas of interest, a solid understanding of the fundamentals of signal acquisition and annotation is still necessary to ensure points are properly mapped and interpreted. Since EAM systems are frequently applied in all modern electrophysiology labs, further developing algorithms and techniques for these kinds of systems is an important step. One of the limitations

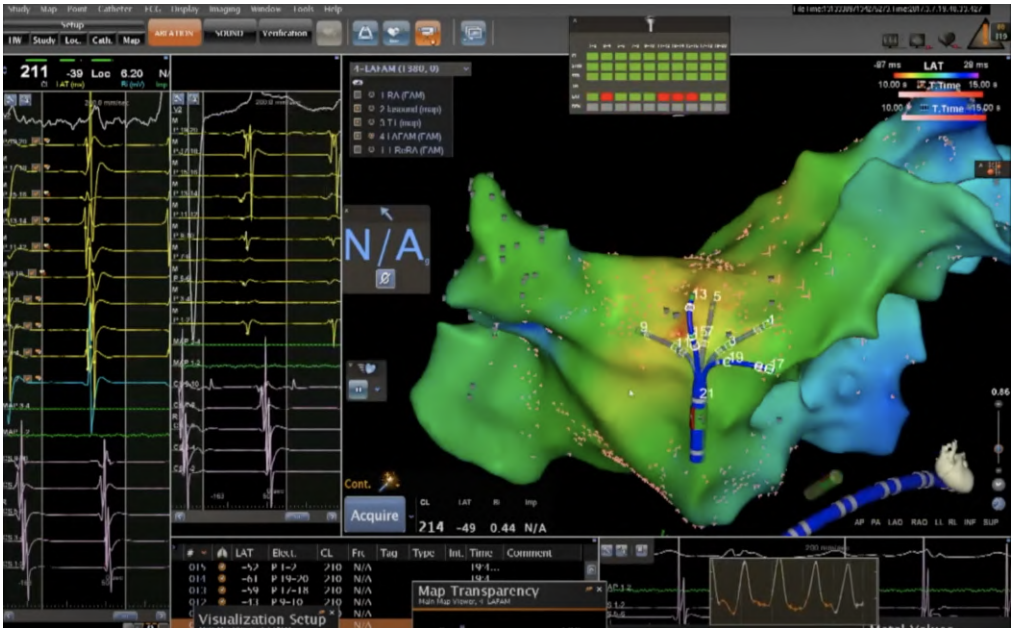


**Figure 2.7:** The screenshot of CARTO® 3 (Biosense Webster) EAM.

of EAM is the duration required to complete mapping, even with multielectrode catheters. Also, in the case of diseased atrium with extended scarring, comprehension of mapping may be sometimes difficult.

## 2.6 Catheters

Invasive catheters are used for electrophysiological testing in order to record the electrical information from within the heart and perform electrical stimulation (pacing). The catheters are composed of a handle (used to control curvature and torsion), an electrode arrangement (at the catheter tip), and a shaft (connecting both). They are made of different materials depending on the desirable properties (deflectability, curvature, stiffness, etc.) and allow different electrode configurations [80].

Catheters are usually guided into the heart through the cardiac structures using fluoroscopy. Right heart structures like RA, RV or CS are commonly accessed through the femoral vein which leads to IVC access [80]. Femoral artery approach and retrograde aortic access is used for mapping LV and MV, but a transeptal approach can also be used [80, 81]. The LA, due to its complex anatomy, is usually mapped via transeptal puncture from the RA [81].

Multielectrode catheters have different shapes and electrode configurations (electrode number and inter-electrode distances) which allow having special properties for mapping individual heart structures (see Figure 2.8). Ablation catheters are a special subclass that is equipped with a metal tip (with different tip lengths) connected to an ablation energy generator in order to perform permanent lesions in the cardiac tissue.

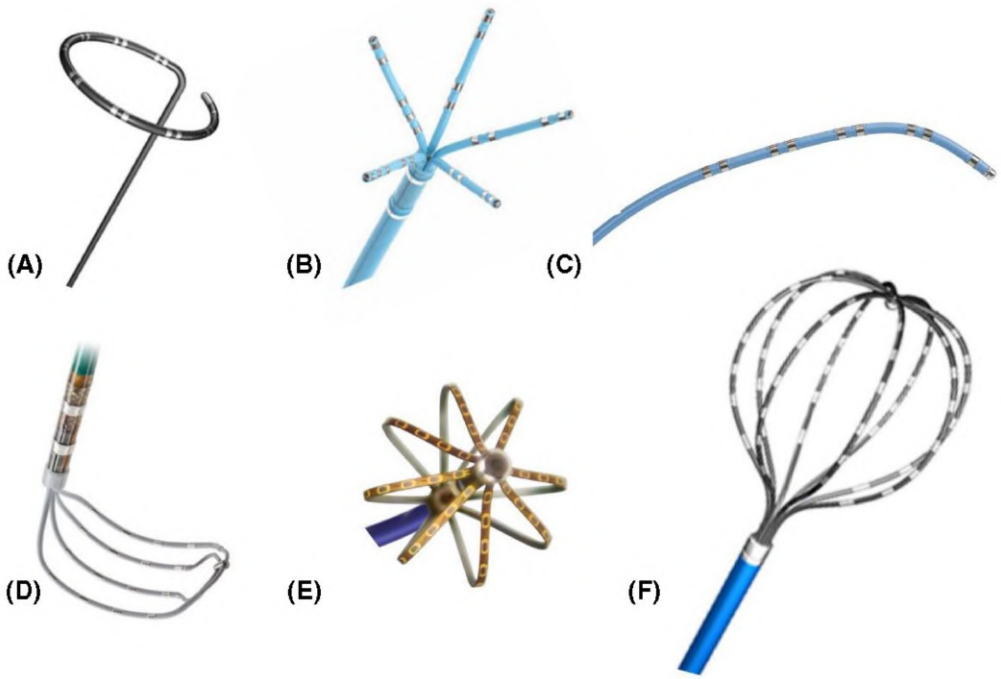


**Figure 2.8:** Commercially available dedicated multielectrode mapping catheters. **(A)**, Circular loop catheter; **(B)**, Five-splined catheter (PentaRay®, Biosense Webster); **(C)**, Linear catheter (Decapolar, Biosense Webster); **(D)**, Grid catheter (Advisor™HD Grid, Abbott); **(E)**, Mini-basket catheter (Orion™, Boston Scientific); **(F)**, Basket catheter (Constellation™, Boston Scientific). Reprinted with permission from [82].

## 2.7 Intracardiac electrograms

Cardiac mapping catheters are equipped with electrodes that record the local electrical potential of the myocardium at their respective position. These recordings are known as intracardiac electrograms (EGMs). Electrograms are usually recorded in unipolar or bipolar modes that have different characteristics but provide complementary information. Both recording modes have specific advantages but also suffer from disadvantages.

Unipolar EGM signal is the potential measured by a single electrode referred to a common potential, generally located on the patient's surface. The recording electrode in contact with the cardiac tissue is connected to the positive input of the recording amplifier, thus a depolarization wavefront propagating toward the electrode generates a positive deflection. As the wavefront reaches and surpasses the electrode, the deflection sweeps steeply negative with a final return to baseline [83], as illustrated in Figure 2.9. The interpretation of the morphology of unipolar EGMs is usually straightforward, and their morphology is independent of the wavefront direction. Although they very well represent the local activity near the measuring electrode, the major disadvantage is that signal quality is often strongly compromised by various artifacts like powerline interference and far-fields generated by depolarization of tissue remote from the recording electrode [84]. For clinical analysis, high signal quality is desired, therefore unipolar EGMs are less preferred in clinical routine compared with bipolar unless the proper ventricular activity is performed.

Bipolar EGM signal is obtained by subtraction of the signals measured by a pair of close neighboring electrodes [83], as illustrated in Figure 2.9. Multielectrode catheters generally have a short inter-electrode distance (around 2 mm) so bipolar recordings are less sensitive to far-field electrical sources which equally affect both unipolar channels, and have a high signal-to-noise ratio [80]. While the morphology of unipolar EGMs is very well studied, the morphology of bipolar EGMs depends on the direction of the activation wavefront with respect to the bipolar recording bipole axis. The bipolar signal amplitude is maximal if the depolarization wavefront propagates parallel to the recording axis, and it is close to zero if the propagation occurs perpendicular to the recording axis [83].

## 2.8 Catheter ablation

Catheter ablation is a procedure used to terminate a faulty electrical pathway from sections of the heart. It has emerged at the forefront of the management of atrial arrhythmias, such as AFL and AF [5, 7]. Successful identification of the mechanism

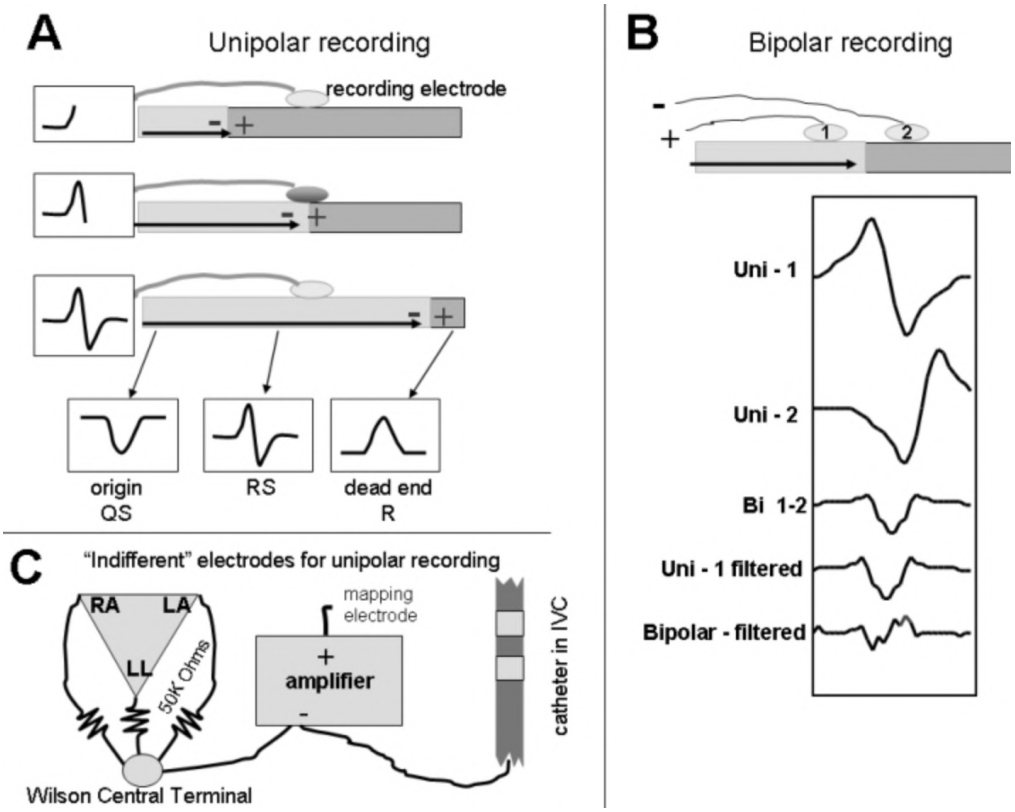


**Figure 2.9:** Genesis of unipolar and bipolar EGMs. **A**, Schematic diagram showing the unipolar recording electrode on a uniform sheet of tissue. Excitation of this tissue proceeds from left to right; the lighter gray areas indicate depolarized tissue. Theoretical recordings from three different sites along the tissue are shown in the bottom panel. Recordings from the initial site of depolarization generate a QS complex. Recordings from the last site to be depolarized generate a monophasic R wave (see text for discussion). **B**, Simulated unipolar and bipolar electrograms. The unipolar signal seen at the positive input to the recording amplifier (Uni-1) is an R-S. The unipolar signal from the second electrode (Uni-2) is in the negative input to the amplifier and therefore is inverted. The summation of these two signals generates the bipolar signal (Bi 1-2). Much of the far-field signal is the same at the two electrodes and therefore is subtracted out. **C**, Setup for unipolar recording, using either the Wilson central terminal or an indifferent electrode in the inferior vena cava (IVC). RA indicates the right arm; LA, the left arm; and LL the left leg ECG electrodes. Reprinted with permission from [85].

and ablation of the critical isthmus is required for the termination of AFL. The isolation of the PVs aims to trigger elimination during AF, with other techniques that focus on substrate modification, such as linear ablation, CFAE ablation, ganglionated plexi ablation, rotor ablation, etc. Up to date, all the strategies for substrate modification are lacking in defined, reproducible endpoints and the best ablation approach and ablation combinations are discussed controversially [5].

Special catheters are advanced into the heart to perform the ablation. In addition to the electrodes for EGM acquisition, these are also equipped with an ablation electrode, typically 4 to 8 mm in length. Radio frequency (RF) alternating current is delivered from the ablation electrode in a range of about 300 to 1000 kHz, in order to stimulate myocardial tissue. Temperature of the targeted tissue is subsequently increased by resistive heating, which induces focal necrosis with minimal injury to surrounding tissues (Figure 2.10A). Lesion formation itself is affected by multiple factors, like catheter tissue contact, transmitted power, time duration of application, or convective heat dissipation from circulating blood. The location of ablation lesions can be annotated in all EAM systems [86].

Cooling is an alternative approach to generating ablation lesions, with specialized cryoablation catheters used to freeze surrounding tissue. These catheters are designed especially for PVI and provide circumferential ablation and simultaneous monitoring of activation inside the PVs (Figure 2.10B) [87].

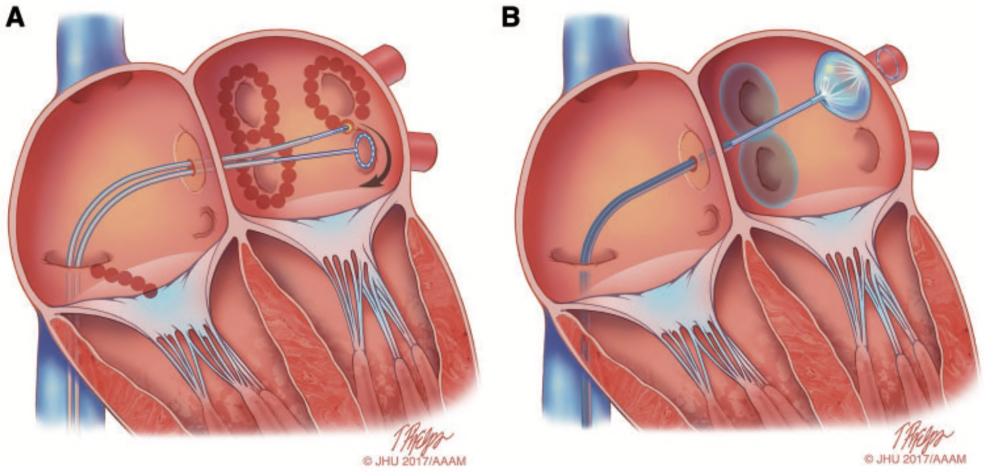


**Figure 2.10:** Schematic drawing showing catheter ablation of AF using either RF energy or cryoballoon AF ablation. **A**, A typical wide area lesion set created using RF energy. Ablation lesions are delivered in a figure of eight pattern around the left and right PV veins. Also shown is a linear CTI lesion created for ablation of typical AFL. A multielectrode circular mapping catheter is positioned in the left inferior PV. **B**, An ablation procedure using the cryoballoon system. Ablation lesions have been created surrounding the right PVs, and the cryoballoon ablation catheter is positioned in the left superior PV. A through the lumen multielectrode circular mapping catheter is positioned in the left superior PV. Illustration: Tim Phelps©2017 Johns Hopkins University, AAM. Reprinted with permission from [5].

# 3

# Cancellation of Ventricular Activity in Atrial Electrograms

## Contents



Successful mapping and ablation in an EP laboratory is critically dependent on acquiring multiple endocavitary signals in the presence of numerous sources of electric noise and interference and displaying these signals in an uncomplicated and clinically relevant fashion, with minimal artifact. Depending on the position of the catheter and type of measurement (i.e., unipolar or bipolar), the performance and interpretation of various signal processing approaches used on EGM get highly degraded by far-field ventricular activity that might be overlapped to the signal of interest, i.e., atrial one [88]. In order to properly study atrial signals, ventricular activity has to be removed from the EGM.

Atrial activity extraction is not only important in EGM during an EP study, but it is also used in the standard surface ECG or in atrial leads of pacemakers. Many

algorithms have been developed in the last decades to reduce the interference caused by the ventricles and such algorithms can be categorized into the following five groups: i) average beat subtraction (ABS) and its variants [89–93]; ii) interpolation [94–96]; iii) adaptive filtering [97–100]; iv) model-based filtering [101]; and v) multi-lead filtering [99]. An extensive review may be found in [102]. For some of these categories, important preprocessing steps, such as beat detection and time alignment of beats, need to be performed before ventricular activity cancellation. A review of methods for handling these well investigated preprocessing steps can be found in [66, 103].

Considering ABS and interpolation, the former estimates a template by averaging several ventricular segments (EGM segments that are taken in correspondence of QRS complexes on a concurrent surface ECG recording), and subtracts the template from the EGM. Several are its variants, including power correction algorithms [104], noise-dependent weights [105] or residual-constrained templates [92]. On the other hand, interpolation substitutes the entire ventricular segment with a prediction obtained from a model of the nearby atrial activity. Common methods in this context are sinusoidal and autoregressive (AR) interpolators with a prediction that minimizes the mean square error or prediction error, respectively.

All ventricular cancellation methodologies present pros and cons. ABS is straightforward to implement and sufficiently resilient to baseline fluctuations, but might leave high power residue and discontinuity at the borders of the ventricular segment. Also, when the morphology of successive ventricular complexes changes significantly in duration and/or amplitude, ABS fails to achieve good cancellation. With interpolation, the residues mimic the frequency content of the nearby atrial activity. However, its forecasting might fail due to poor model fitting [102], especially at high heart rate, when the duration of the nearby atrial activity, before and after the nearby ventricular artifacts, is limited in time. Also, with AR models, there is a forecasting horizon where previously predicted samples struggle in predicting new ones and the prediction reaches the average of the process. Other proposed alternatives consist of applying signal separation algorithms, which are able to use the multi-lead information, based on principal component analysis or independent

component analysis [99]. Even though joint processing of multiple leads may offer certain advantages, multichannel EGM recordings are often not available (for example, on implantable cardioverter-defibrillator devices), thus causing these techniques to be unsuited for these situations.

The rest of this chapter describes a novel ventricular cancellation strategy, which we termed r-ABS, based on combining ABS and interpolation in a unified framework [106]. The new algorithm merges the pros of ABS and interpolation, while trying to avoid their cons. It has been tested on both synthetic and real EGMs, while its performance was compared with various methods.

## 3.1 Refined atrial activity estimate

Let us have one EGM signal $z_k$, with $k$ the sample index, in which the ventricular activity is overlapped. In addition, we consider the time-positions of the ventricular complexes to be known (e.g., from a concurrent ECG $e_k$) and that, for each ventricular complex, a portion of $N$ EGM samples

$$\mathbf{z} = [z_i, z_{i+1}, \cdots, z_{i+N-1}]^\intercal$$

is located such that the R-peak, as identified on the ECG at position $k = i + N/2$, is approximately at the center (the procedure described in this section will be repeated for each ventricular activity). We assume the common signal-plus-noise model for the endocavitary recording

$$\mathbf{z} = \mathbf{a} + \mathbf{v}, \tag{3.1}$$

where $\mathbf{v} = [v_i, \cdots, v_{i+N-1}]^\intercal$ is the ventricular activity to remove (hence, the noise) and $\mathbf{a} = [a_i, \cdots, a_{i+N-1}]^\intercal$ is the atrial activity, including both far and near field effects. Along the entire EGM recording, $a_k$ is modeled as a zero-mean stationary stochastic Gaussian process with autocovariance function $\rho(\tau)$, with $\tau$ being the lag, as in [107]. The sequence $\boldsymbol{a}$ of $N$ stochastic variables is distributed as a multivariate Gaussian variable

$$\mathbf{a} \sim \mathcal{N}(0, \mathbf{\Sigma}_{aa}), \tag{3.2}$$

where $\mathbf{\Sigma}_{aa}$ is the Toeplitz covariance matrix, built from the values of $\rho(\tau)$.

Additionally, let us also set apart $L$ (left) and $R$ (right) samples respectively before and after the window bracketing the ventricular complex. Figure 3.1 shows these two segments with respect to a ventricular complex. In these small portions, by construction, no ventricular activity is present and $z_k = a_k$. The samples are stored in the vectors $\mathbf{l} = [z_{i-L}, \cdots, z_{i-1}]^\intercal$ and $\mathbf{r} = [z_{i+N}, \cdots, z_{i+N+R-1}]^\intercal$. Then, under the stationary and normality assumptions, the vector

$$\begin{bmatrix} \mathbf{l} \\ \mathbf{a} \\ \mathbf{r} \end{bmatrix} \sim \mathcal{N}\left( \mathbf{0}, \begin{bmatrix} \mathbf{\Sigma}_{ll} & \mathbf{\Sigma}_{la} & \mathbf{\Sigma}_{lr} \\ \mathbf{\Sigma}_{al} & \mathbf{\Sigma}_{aa} & \mathbf{\Sigma}_{ar} \\ \mathbf{\Sigma}_{rl} & \mathbf{\Sigma}_{ra} & \mathbf{\Sigma}_{rr} \end{bmatrix} \right), \tag{3.3}$$

is distributed as a multivariate Gaussian variable and its covariance is built from the values of $\rho(\tau)$ (as for Eq. (3.2)), given that the vectors $\boldsymbol{l}$, $\boldsymbol{a}$, and $\boldsymbol{r}$ contain only atrial activity. The definition of $\boldsymbol{l}$ and $\boldsymbol{r}$ needs the assumption that duration of $\boldsymbol{a}$ is known. While the length of a beat varies dramatically in AF, the signal model in Eq. (3.1) does not reflect this variation since a large enough, fixed value of $N$ is assumed.

For convenience, we can reorder the variables by defining the "boundary" vector

$$\mathbf{q} = \begin{bmatrix} \mathbf{l} \\ \mathbf{r} \end{bmatrix} \sim \mathcal{N}(\mathbf{0}, \mathbf{\Sigma}_{qq}), \tag{3.4}$$

where

$$\mathbf{\Sigma}_{qq} = \begin{bmatrix} \mathbf{\Sigma}_{ll} & \mathbf{\Sigma}_{lr} \\ \mathbf{\Sigma}_{rl} & \mathbf{\Sigma}_{rr} \end{bmatrix}, \tag{3.5}$$

and the following matrices

$$\mathbf{\Sigma}_{aq} = \begin{bmatrix} \mathbf{\Sigma}_{al} & \mathbf{\Sigma}_{ar} \end{bmatrix}, \qquad \mathbf{\Sigma}_{qa} = \begin{bmatrix} \mathbf{\Sigma}_{la} \\ \mathbf{\Sigma}_{ra} \end{bmatrix}. \tag{3.6}$$

ABS is based on the fact that the ventricular and atrial activities during AF are uncorrelated [102]. Thus, the synchronous average of a set of ventricular complexes reduce the atrial activity overlapped and it represents a robust estimate of the ventricular activity. However, ABS lacks of adaptability, thus possibly leaving high power residues and border discontinuities.

On the other hand, interpolation relies on the fact that, in short time windows, the atrial activity measured in a given site is stationary. This assumption implies

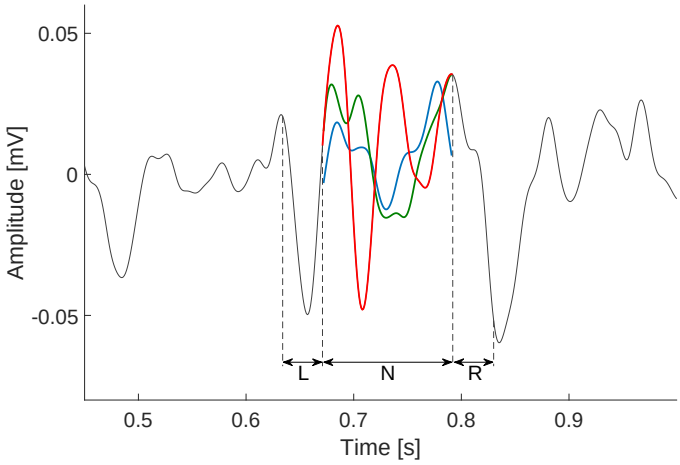


**Figure 3.1:** Example of EGM signal where ventricular activity (red line) is overlapped, along with two possible realizations of atrial activities reconstructed assuming its distribution to be described either by Eq. (3.7) (green line) or Eq. (3.2) (blue line). The segments of $L$, $N$ and $R$ samples are limited by vertical dashed lines.

that the atrial activity masked by the ventricular complex is distributed as that in the surrounding. Then, it extrapolates the result of the cancellation starting from the borders of the intervals and moving towards the center of the ventricular complex. Consequently, the estimate at the center of the window including the ventricular complex is less reliable.

In the method we proposed, we merged ABS and interpolation, leveraging the robust estimate provided by ABS (with a better estimate at the center of the cancellation window) as well as the fact that the residue should be distributed as the surrounding atrial activity (thus avoiding large power residues and discontinuities at the boundary of the cancellation window). The method is constituted by the following two steps.

First, once the samples $\hat{\boldsymbol{q}}$ from $\boldsymbol{q}$ are known, the atrial activity $\mathbf{a}$, underneath the ventricular complex, is distributed as

$$\mathbf{a}|\hat{\mathbf{q}} \sim \mathcal{N}\Big( \underbrace{\boldsymbol{\Sigma}_{aq}\boldsymbol{\Sigma}_{qq}^{-1}\hat{\mathbf{q}}}_{\boldsymbol{\mu}_*}, \underbrace{\boldsymbol{\Sigma}_{aa} - \boldsymbol{\Sigma}_{aq}\boldsymbol{\Sigma}_{qq}^{-1}\boldsymbol{\Sigma}_{qa}}_{\boldsymbol{\Sigma}_*} \Big). \tag{3.7}$$

In fact, $\mathbf{a}$ is conditioned on the samples $\hat{\boldsymbol{q}}$ of the boundary intervals (that are known and different for each ventricular complex) and the conditional probability

of a multivariate Gaussian variable is another multivariate Gaussian variable. For compactness, we set $\boldsymbol{\mu}_* = \boldsymbol{\Sigma}_{aq}\boldsymbol{\Sigma}_{qq}^{-1}\hat{\mathbf{q}}$ and $\boldsymbol{\Sigma}_* = \boldsymbol{\Sigma}_{aa} - \boldsymbol{\Sigma}_{aq}\boldsymbol{\Sigma}_{qq}^{-1}\boldsymbol{\Sigma}_{qa}$.

Second, we model the vector $\mathbf{v}$ in Eq. (3.1) by the sum of the ventricular estimate $\hat{\mathbf{t}}$ provided by ABS and a refinement term, as follows

$$\mathbf{v} = \hat{\mathbf{t}} + \boldsymbol{\Phi}^\intercal \mathbf{c}, \tag{3.8}$$

where $\boldsymbol{\Phi}$ is a $B \times N$ matrix containing $B$ basis functions. The random vector $\mathbf{c}$ contains unknown coefficients which we assume to be small (due to the robust estimate of ABS) and distributed as a multivariate Gaussian variable with zero mean and unknown variance $\sigma_c^2$. A point estimate of the vector $\mathbf{c}$ can be found by maximizing the logarithm of its posterior probability, i.e., log Maximum a Posteriori (MAP) estimate, conditioned on $\mathbf{a} = \mathbf{z} - \mathbf{v}$. The log MAP estimate of $\mathbf{c}$ is given by

$$\hat{\mathbf{c}} = \underset{\mathbf{c}}{\operatorname{argmax}} \log P(\mathbf{c}|\mathbf{a}) = \underset{\mathbf{c}}{\operatorname{argmax}} \log \left[P(\mathbf{z} - \mathbf{v}|\mathbf{c})P(\mathbf{c})\right] \tag{3.9}$$

where $P(\mathbf{c}|\mathbf{a})$ is the posterior probability of $\mathbf{c}$ given $\mathbf{a}$, and $P(\mathbf{c})$ is the prior probability of $\mathbf{c}$. Using Eq. (3.7) and Eq. (3.8), we obtain a point estimate of $\hat{\mathbf{c}}$, as follows

$$\begin{aligned} \hat{\mathbf{c}} &= \underset{\mathbf{c}}{\operatorname{argmin}}\, J(\mathbf{c}) \\ J(\mathbf{c}) &= (\mathbf{z} - \hat{\mathbf{t}} - \boldsymbol{\Phi}^\intercal \mathbf{c} - \boldsymbol{\mu}_*)^\intercal {\boldsymbol{\Sigma}_*}^{-1} (\mathbf{z} - \hat{\mathbf{t}} - \boldsymbol{\Phi}^\intercal \mathbf{c} - \boldsymbol{\mu}_*) + \lambda \mathbf{c}^\intercal \mathbf{c}. \end{aligned} \tag{3.10}$$

Taking the derivative of $J(\boldsymbol{c})$ with respect to $\mathbf{c}$ and introducing a regularization parameter $\lambda$, which absorbs the unknown variance of $\mathbf{c}$, the estimate of the coefficient vector is given by the solution of the linear system

$$(\boldsymbol{\Phi}\boldsymbol{\Sigma}_*^{-1}\boldsymbol{\Phi}^\intercal + \lambda \mathbf{I})\hat{\mathbf{c}} = \boldsymbol{\Phi}\boldsymbol{\Sigma}_*^{-1}(\mathbf{z} - \hat{\mathbf{t}} - \boldsymbol{\mu}_*), \tag{3.11}$$

where $\mathbf{I}$ is the identity matrix.

Finally, the final estimate of ventricular activity is

$$\hat{\mathbf{v}} = \hat{\mathbf{t}} + \boldsymbol{\Phi}^\intercal \hat{\mathbf{c}}. \tag{3.12}$$

In general, there is no standard rule on how to choose certain basis functions over others, and, in most of the cases, only empirical considerations guide the selection

for the problem at hand. In our case, considering that most of the ventricular energy will be located at the center of the window by construction (at sample $\approx N/2$), a reasonable choice is to set periodical boundary conditions (in the hypothesis that at the boundaries the signal might be close to zero). A common set of basis functions, displaying this characteristic, is the set of the sinusoidal functions, along with their harmonics, with fundamental frequency $\omega = 2\pi f_s/N$ with $f_s$ being the sampling rate. With this choice, which we performed, the coefficients $\mathbf{c}$ correspond to the Discrete Fourier Transform of the refinement factor $\mathbf{\Phi}^\intercal\mathbf{c}$ in Eq. (3.8). We employed the harmonics of order $0, \cdots, (B-1)/2$ with $B$ an odd number.

The covariance matrix in (3.3) was estimated using the coefficients of an AR model fitted on the atrial activity comprises between two consecutive ventricular complexes. In particular, for the $k$-th ventricular activity, we fitted the model on the atrial signal between the $k-1$ and $k$ beats. First, the covariance function was estimated using the Yule-Walker equations and then the covariance matrix, of dimension $(L+N+R) \times (L+N+R)$, was composed.

Figure 3.1 depicts a small portion of EGM, where the ventricular activity (in red) is removed and the atrial activity underneath reconstructed using Eq. (3.12) and Eq. (3.7) and the set of harmonic basis functions. As expected, the method avoids discontinuities at the border of the interval (green line). On the other hand, if the distribution of $\boldsymbol{a}$ were not conditioned on $\boldsymbol{q}$ and Eq. (3.2) used instead, the result would have been disconnected form the nearby activity (blue line).

Finally, for each ventricular complex to cancel, the algorithm can be summarized as follows:

1. Estimation of $\mathbf{\Sigma}_{\text{aug}}$ through AR model fitting;
2. Construction of the quantities in Eq. (3.4), Eq. (3.5) and Eq. (3.6);
3. Estimation of the template $\hat{\mathbf{t}}$;
4. Construction of the basis functions and building of $\mathbf{\Phi}$;
5. Construction of $\boldsymbol{\mu}_*$ and $\mathbf{\Sigma}_*$ according to Eq. (3.7);

6. Estimate of the refinement $\mathbf{\Phi}^{\intercal}\hat{\mathbf{c}}$ using Eq. (3.11);

7. Construction of the refined estimate $\hat{\mathbf{v}}$ as in Eq. (3.12).

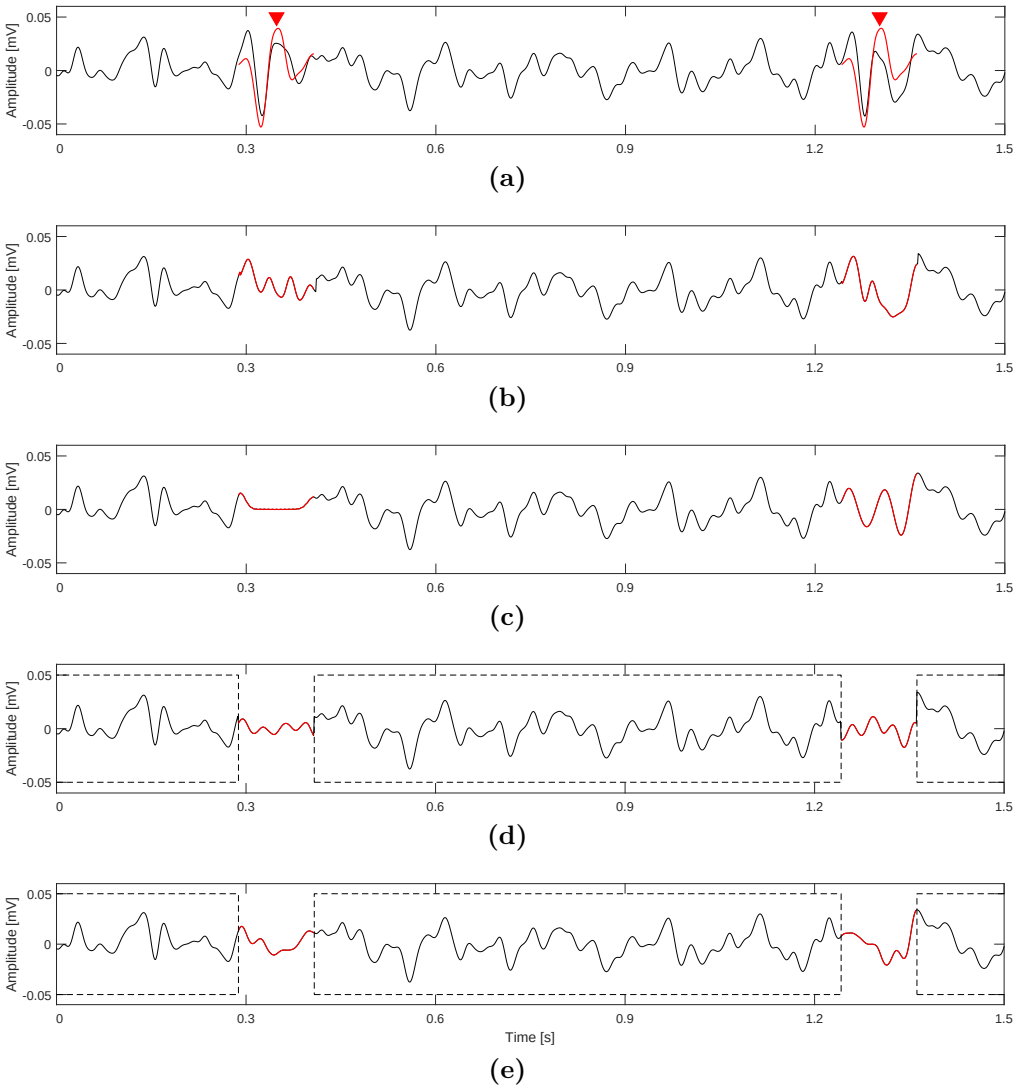


**Figure 3.2:** Example of real clinical EGM that underwent four different ventricular cancellation algorithms. The original EGM is shown in panel (a). Red arrow-tip markers point to ventricular activities (determined by means of the surface ECG). Red thick signals show the ABS template $\hat{\mathbf{t}}$ (a) and residual activities of ABS (b), AR interpolation (c), r-ABS without considering the samples at the boundaries (d), and r-ABS with considering boundary samples (e). The dashed box encloses the portion of EGM used for fitting the AR model.

## 3.2 Data

The algorithm was tested on two datasets and its performance were compared to those achieved by other ventricular cancellation methodologies. The first dataset was comprised of 10 synthetic EGMs, built along the line of what is described in [92]. Briefly, the far-field atrial activity was modeled using an AR model, whereas the near-far atrial activity and ventricular activity were generated using an electric dipole moving along a straight line, with respect to the electrodes. The average ratio between ventricular and near-field atrial peak amplitude was set to 4, while the average ratio between the near-field atrial peak amplitude and the standard deviation of the far-field activity was 2. Each synthetic EGM signal contained the interference of 120 ventricular contractions, generated independently between each other.

The second dataset was the Intracardiac Atrial Fibrillation Database, freely available of Physionet [108], and it was composed of the recordings obtained from eight patients collected during EP studies. Signals were all bipolar EGMs sampled at 1000 Hz and the temporal locations of the beats, as obtained from the ECG, were provided. We used the dataset for two analyses. Given the fact that the true atrial activity can not be known in real EGMs, in a first analysis, we quantified the performance of all algorithms by means of metrics suitable for real data (see Section 3.4 for their definition). The performance metrics on synthetic and real data were then considered together to create a ranking of the methodologies. In the second analysis, we determined the preference of experienced clinical personnel between the two-best performing cancellation algorithms on this dataset. For both datasets, ventricular activity length was set to $N = 120$ samples, corresponding to 120 ms at a sampling rate of 1000 Hz.

## 3.3 Selection of hyper-parameters

Three hyper-parameters needed to be set: i) the number of basis functions $B$; ii) the number of samples $L = R$ (length of the left and right boundary atrial activity), where for simplicity we considered the left and right window to have the same size;

and iii) the regularization parameter $\lambda$. The first five synthetic signals, hereafter named "training set", were used for hyper-parameter selection, considering the true atrial activity (which was known). We used a grid search approach in which, for each combination of $B$, $L$ and $\lambda$, the root mean square error (RMSE) between the residual activity after cancellation and the true activity was computed. We finally selected the combination which gave the smallest RMSE.

Using this strategy, the three hyper-parameters were set to $B = 11$ (corresponding to a maximum frequency of 41.7 Hz), $L = R = 3$ samples, and $\lambda = 800$ (which corresponds to $\sigma_c = 0.025$ and a standard deviation of the refinement $\mathbf{\Phi}^\intercal \mathbf{c}$ of $\sqrt{(B-1)\sigma_c^2/2} = 56\ \mu V$). As expected, the value of 56 $\mu V$ is lower than the average standard deviation of the vectors $\mathbf{z}$, i.e., 112 $\mu V$, given the fact that the average template $\hat{\mathbf{t}}$, built by ABS, is already a reasonable estimate of the ventricular activity.

## 3.4 Performance evaluation

The performance of the algorithms was quantified by comparing the true atrial activity known in the synthetic validation set with the corresponding estimated one. The performance was evaluated by two metrics: i) RMSE; and ii) Ventricular Depolarization Reduction (VDR) [99]. VDR was defined as $\text{VDR} = 10\log_{10}(R_{EGM}/R_{VR})$, where $R_{EGM}$ is the ventricular complex amplitude of the original EGM, and $R_{VR}$ is the residual amplitude of the EGM after ventricular activity reduction. Furthermore, we quantified the RMSE while changing the sampling rate of the signals. Sampling rate decimation (SRD) was performed in a range from 200 Hz to 1000 Hz, with a step of 200 Hz. A low pass filter was applied to avoid aliasing on the decimated signals.

Two different metrics were used for performance evaluation on the real data composing the validation set. The first one computed the percentage of high power residues (HPRs) remaining in the signal after cancellation (similarly to [92]). In practice, we counted the proportion of how many residual segments had a mean power higher than a certain threshold. Such threshold was estimated as the $95^{th}$ percentile of the mean power distribution of windows of atrial activities of length 120 ms (which is the same length of the $N$-window we employed). With the second

metric, we evaluated the log-likelihood of the residual activity with respect to the fitted AR model. The main rationale was to quantify how "close" the residual activity was to the nearby atrial activity. To do so, we computed the following formula for each ventricular cancellation performed

$$\log \mathcal{L} = -\frac{N}{2} \log \left(2\pi\sigma_\epsilon^2\right) - \frac{\mathbf{e}^\intercal \mathbf{e}}{2\sigma_\epsilon^2} \tag{3.13}$$

where $\sigma_\epsilon^2$ was the variance of the prediction error estimated during AR model identification, and the vector $\mathbf{e}$ was the difference between the estimated atrial activity and its 1-step prediction based on the same AR model[1]. In case of optimal prediction, the vector $\mathbf{e}$ will have a variance of $\sigma_\epsilon^2$ (lower bound), thus obtaining a maximal log-likelihood. The median $\log \mathcal{L}$ was retained for ranking the algorithms.

All performance metrics computed on the validation set were used to rank all the six methods. To do so, we used a radar chart. The radar chart consisted of a sequence of five equi-angular axes, with each axis representing one of the five performance evaluation metrics described in sections before. The values on the axes

[1]Eq. (3.12) can be derived from the log-likelihood function for the multivariate normal distribution (zero mean):

$$\log \mathcal{L}(\mathbf{x}) = -\frac{N}{2} \log \left(2\pi|\mathbf{\Sigma}_x|\right) - \frac{1}{2}\mathbf{x}^\intercal \mathbf{\Sigma}_x^{-1}\mathbf{x}.$$

Considering AR model

$$x_n = -\sum_{i=1}^{P} a_i x_{n-i} + w_n,$$

we have

$$\mathbf{w} = \mathbf{H}\mathbf{x}, \qquad \mathbf{\Sigma}_w = \mathbb{E}[\mathbf{H}\mathbf{X}\mathbf{X}^\intercal\mathbf{H}^\intercal] = \mathbf{H}\mathbf{\Sigma}_x\mathbf{H}^\intercal.$$

where $\mathbf{H}$ is a lower triangular matrix of model coefficients with ones on the main diagonal, therefore $|\mathbf{H}| = 1$ and $|\mathbf{\Sigma}_w| = |\mathbf{\Sigma}_x|$. Then, because the prediction error must be distributed as a white Gaussian noise

$$\mathbf{e} \approx \mathbf{w}, \qquad \mathbf{\Sigma}_e \approx \mathbf{\Sigma}_w,$$

we can derive

$$\begin{aligned}
\log \mathcal{L}(\mathbf{x}) &= -\frac{N}{2} \log \left(2\pi|\mathbf{\Sigma}_x|\right) - \frac{1}{2}\mathbf{x}^\intercal \mathbf{\Sigma}_x^{-1}\mathbf{x} \\
&= -\frac{N}{2} \log \left(2\pi|\mathbf{\Sigma}_x|\right) - \frac{1}{2}\mathbf{x}^\intercal \mathbf{H}^\intercal (\mathbf{H}^\intercal)^{-1} \mathbf{\Sigma}_x^{-1} \mathbf{H}^{-1}\mathbf{H}\mathbf{x} \\
&= -\frac{N}{2} \log \left(2\pi|\mathbf{\Sigma}_x|\right) - \frac{1}{2}\mathbf{x}^\intercal \mathbf{H}^\intercal (\mathbf{H}\mathbf{\Sigma}_x\mathbf{H}^\intercal)^{-1}\mathbf{H}\mathbf{x} \\
&= -\frac{N}{2} \log \left(2\pi|\mathbf{\Sigma}_w|\right) - \frac{1}{2}\mathbf{w}^\intercal \mathbf{\Sigma}_w^{-1}\mathbf{w} \\
&= -\frac{N}{2} \log \left(2\pi|\mathbf{\Sigma}_e|\right) - \frac{1}{2}\mathbf{e}^\intercal \mathbf{\Sigma}_e^{-1}\mathbf{e} = \log \mathcal{L}(\mathbf{e}).
\end{aligned}$$

coincided with the ranking of the method in that particular performance metric. A line was drawn connecting the ranking values for each axis, forming a polygon for each method. Methods were ranked by computing the area of their polygons, and such areas were normalized by the full area of the polygon. The two best-performing methodologies were retained for the evaluation with expert clinicians.

Given the fact that only heuristics can be computed to quantify the cancellation performance on real data, in addition to all the other metrics described in the paragraphs before, we tried to use the expertise of clinicians as one of the possible evaluation metric. In collaboration with the hospital Fondazione IRCCS Ca' Granda Ospedale Maggiore Policlinico di Milano, Milan, Italy, we conducted an experiment where we showed two panels with the same portion of atrial endocavitary signal in which the ventricular far field activity has been removed with the two best-performing algorithms according to the ranking: i) r-ABS; and ii) AR interpolation. Expert clinicians were asked to select based on their experience which portion of the atrial endocavitary signal contained the best reconstruction of the atrial signal with respect to the activity around it. The experiment was performed by ten different subjects, among whom seven were medical doctors and three clinical engineers, who were all experts in EP studies. Each of them were asked to repeat the experiment 30 times, amounting to a total of 300 repetitions of the experiment. Signals were taken from the Intracardiac Atrial Fibrillation Database [108] and the order of the signal portions and the selection of the intracardiac lead shown on the panels were randomized. Figure 3.3 shows the graphical user interface for the experiment. All code, including the interface, was developed entirely in MATLAB programming language.

Performance metrics of different algorithms were compared using the Wilcoxon signed rank test. A p-value less than 0.05 was considered statistically significant.

We compared r-ABS with five other methods, two types of ABS and three types of interpolation. The first one was ABS, where a template $\hat{\mathbf{t}}$ is obtained by averaging the EGM segments in correspondence to the time-positions of the ventricular complexes, and the template $\hat{\mathbf{t}}$ is subtracted from the original endocardial

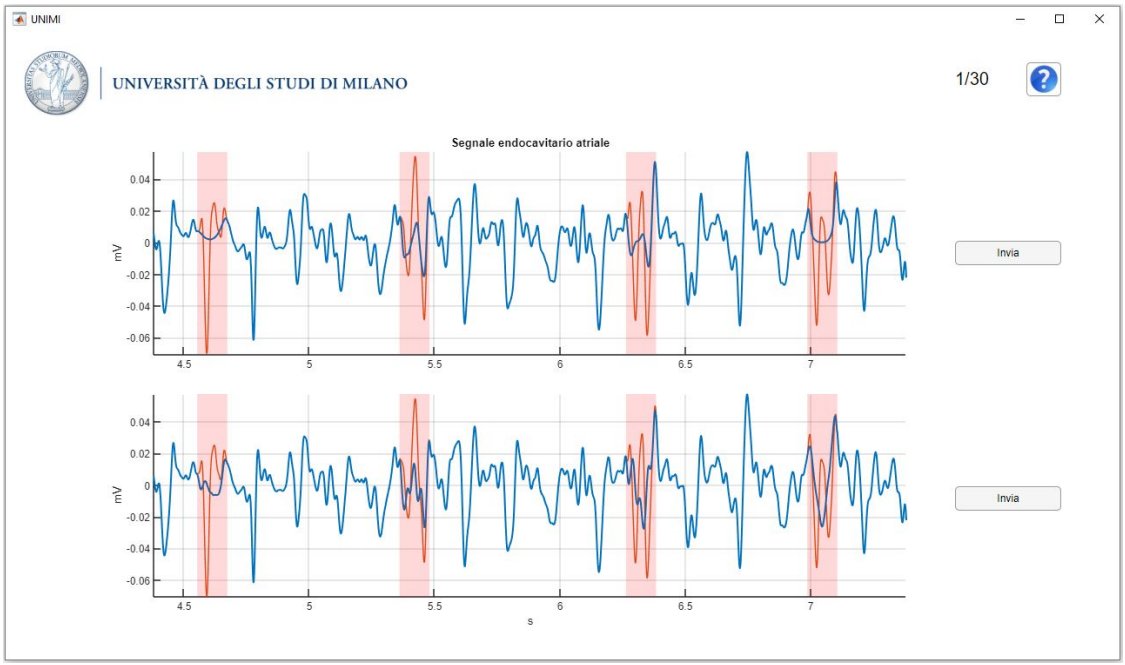


**Figure 3.3:** Visual evaluation experiment performed by the expert clinicians. The software shows two panels with the same portion of atrial endocavity signal in which the ventricular far field activity has been removed (in blue). The cancellation has been performed by two different algorithms, AR interpolation on one of the panels and r-ABS on the other. The pink area highlights the areas of the signal where atrial activity has been reconstructed by the algorithm, in correspondence with the R-peak (on concurrent surface ECG). The original EGM is shown on the panels in red color. The portion outside the pink area are the measured, unaltered activity. It was required from subjects to select 30 times which portion of the atrial endocavitary signal (above or below) contains the best reconstruction of the atrial signal with respect to the activity around it. For each of the 30 selections, the the signal portions and the order of the algorithms were applied in randomly.

recording $\mathbf{z}$ after time alignment by cross-correlation. The second one was ABS with adjustment of the power (p-ABS), where the template $\hat{\mathbf{t}}$ (before the subtraction) is multiplied by $(\mathbf{z}^\intercal\mathbf{z})/(\hat{\mathbf{t}}^\intercal\hat{\mathbf{t}})$ [104] to compensate for amplitude variations.

Regarding interpolation methods, they all treat ventricular segments as completely missing, to be replaced by interpolating the boundaries. The simplest one used was flat interpolation (Flat-int), where ventricular segment was simply set to 0, and the other two were interpolation based on AR models (AR-int) using surrounding samples [102], and interpolation based on singular spectrum analysis (SSA-int) [109].

## 3.5 Results

Focusing on the metrics used on synthetic data, the RMSE between the estimated atrial activity and the true one, for each of the six considered methodologies, is reported on Figure 3.4a. Both ABS and p-ABS performed the least (p-ABS had a median RMSE of 2.9% lower than ABS; $p < 0.05$). On the other hand, r-ABS outperformed all the others, having a RMSE statistically significantly lower from that of the AR interpolation method ($p < 0.05$), that ranked second. SSA interpolation ranked third and flat interpolation ranked fourth. Also, in regards to SRD, reported in Table 3.1, r-ABS proved to be the most robust method, followed by SSA interpolation, and again both ABS and p-ABS performed the least. AR and flat interpolation ranked third with the same score. In terms of VDR, excluding flat interpolation, AR interpolation was the top performer (Median VDR = 43.58), followed by the SSA interpolation and r-ABS which performed similarly (39.68 and 38.72), and yet again ABS and p-ABS performed the least (35.78 and 36.16)

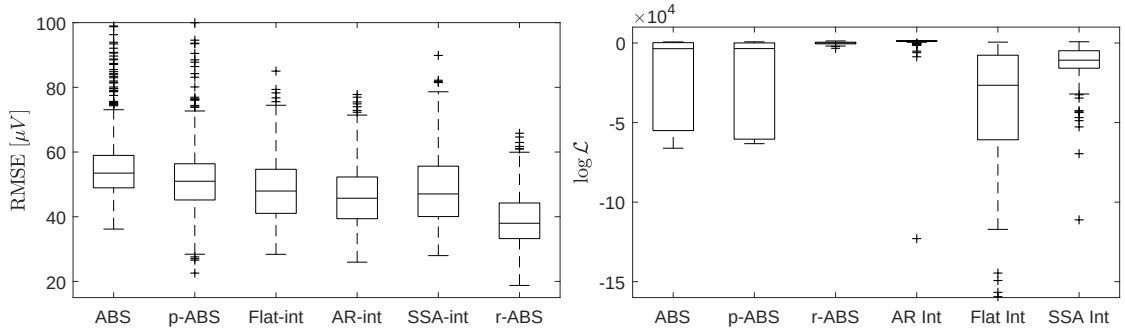


**Figure 3.4:** Boxplots of the performance for the six algorithms. Panel (a) reports the root MSE between the residual activity and the true one on the synthetic data. Panel (b) reports the log-likelihood computed on the clinical signal.

Furthermore, on clinical data r-ABS and AR interpolation resulted with the highest log-likelihood, even though r-ABS ranked second in this case ($p < 0.05$). In addition, ABS and p-ABS did not show any statistically significant difference ($p > 0.05$), while the flat interpolation performed the least ($p < 0.05$). SSA interpolation ranked fifth. This is reported on Figure 3.4b. Excluding flat interpolation (which by

**Table 3.1:** Median and interquartile range for each algorithm and performance metric.

| Metric | ABS | p-ABS | Flat-int |
|---|---|---|---|
| RMSE [$\mu V$] | 53.5 (48.9, 59.0) | 51.0 (45.2, 56.4) | 47.9 (41.0, 54.7) |
| SRD [$\mu V$] | 54.4 (50.0, 60.2) | 52.1 (46.5, 57.3) | 47.5 (40.6, 54.2) |
| VDR | 35.8 (35.3, 36.3) | 36.2 (35.5, 37.0) | – |
| $\log \mathcal{L} \times 10^{-3}$ | -3.5 (-55.0, -0.2) | -3.5 (-60.4, -0.1) | -60.8 (-26.5, -7.7) |
| HPR [%] | 8.3 | 4.8 | 0 |
| Metric | AR-int | SSA-int | r-ABS |
| RMSE [$\mu V$] | 45.7 (39.4, 52.3) | 47.0 (40.0, 55.6) | 38.0 (33.2, 44.2) |
| SRD [$\mu V$] | 45.9 (39.6, 52.5) | 45.0 (38.6, 53.1) | 40.1 (35.0, 45.7) |
| VDR | 43.6 (41.5, 45.6) | 39.7 (38.5, 40.8) | 38.7 (38.2, 39.3) |
| $\log \mathcal{L} \times 10^{-3}$ | 1.4 (1.0, 1.4) | -26.5 (-60.8, -7.6) | 0.0 (-0.5, 0.5) |
| HPR [%] | 4.1 | 0.7 | 2.8 |

the definition must have the perfect score of 0% in this metric), SSA interpolation and r-ABS resulted with the lowest percentage of high power residues (0.7% and 2.8%), while ABS and p-ABS performed the least (8.3% and 4.8%). AR interpolation ranked third (4.1%) in this case.

Radar chart on Figure 3.5 shows the general comparison between all of the six considered ventricular activity cancellation methods using five different performance metrics. The proposed method (r-ABS) performed the best in terms of RMSE even after SRD, coming in very close second with regard to log-likelihood. It ranked fourth in VDR and third in the percentage of HPRs. Generally, it has the largest area in the chart (with the value of 0.63, where the maximum area is being normalized to 1) and it is a very good performer across all the metrics. In the second place is AR interpolation (0.54), third is SSA interpolation (0.42), followed by flat interpolation (0.38), then p-ABS (0.17), and finally ABS (0.04). It is important to note that even though flat interpolation (which is essentially

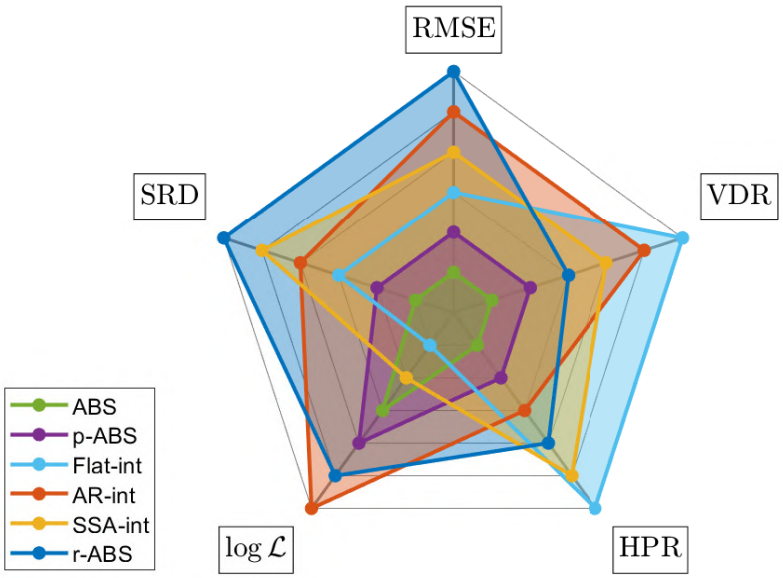


**Figure 3.5:** Radar chart of the performance for the six algorithms. Five axes represent different performance evaluation metrics. The positions on each of the axes correspond to the ranking in that particular metric. Methods being compared are visualized in different colors according to the legend.

substitution of ventricular segment with 0) provides the best performance for VDR and HPR, its behavior is not physiological.

Regarding the visual evaluation experiment performed by the expert clinicians, there was a total of 300 choices between AR interpolation and r-ABS. Out of these 300 choices, r-ABS was choosen 298 times, which leaves only 2 choices of AR interpolation. It shows the unambiguous preference of clinicians (99.33%) for ventricular cancellation made by r-ABS over the ones made by AR interpolation.

## 3.6 Discussion

The extremely important preprocessing step for all further analyses of EGM is cancellation of ventricular activity. The described methodology in this chapter combines two common techniques, ABS and interpolation, in an unified framework which was able to refine and improve the ventricular activity estimate, under the stationarity assumption of the atrial activity in very short time windows. The algorithm falls under the area of model-based filters such as Kalman filters and smoothers.

Different alternatives for ventricular activity cancellation in EGM have been compared in this chapter, each one of them with advantages and disadvantages. Considering that the most widely extended algorithms are ABS-based, in which common problems are lack of continuity at the boundaries of the $N$-window and high power residues (Figure 3.2b) [92, 102], to overcome this problem our algorithm modulated the template $\hat{\mathbf{t}}$ to match the stochastic process' properties (Figure 3.2d).

On the other hand, interpolation-based algorithms using AR models tend to predict poorly the expected value of the stochastic process for long temporal horizons (Figure 3.2c). This effect results in a flat signal around the peak of the ventricular activity (especially for low model orders), while preserving the frequency content of the process at the borders of the $N$-window. Although the residual power lies in the range of what expected from atrial activity and the frequency content is preserved at the borders, the reconstructed atrial activity lacks details exactly in the part of the $N$-window which much needed of refinement. This phenomenon did not happen with r-ABS, as the algorithm was able to preserve the frequency content by considering the AR model's $\Sigma_A$, while still exploiting the ABS estimate.

Moreover, we showed that the new proposed strategy provides compelling results and we quantified the improvement in respect to other methods. Such improvements were observed not only on simulated data but also on clinical data recorded during routine ablation procedures and were documented by several metrics used to evaluate cancellation performances. Performance evaluation has been approached in many different ways in the literature. Performance evaluation based on simulated data allows direct quantification of the error between the extracted and true atrial signals, but performance evaluation based on real data must rely on some indirect measures. Unfortunately, since the measures, as well as the data sets used for evaluation, differ between studies, it is hardly possible to make a fair comparison of performance. Since it is not possible to have an indisputable metric to evaluate cancellation performance in clinical data, we went a step further and used the expertise of clinicians, who unambiguously preferred cancellation residues made by our proposed method over the other one.

Being a variant of ABS methodology, r-ABS still shares some of its limitations. Firstly, it requires that QRS complexes are detected before any operation can be performed, opposed to methods based on adaptive filtering and multi-lead, blind source separation that do not require QRS detection. Some 30 to 40 beats are at least needed by ABS and variants to produce a template in which the atrial activity is reasonably well-suppressed, provided that the noise level is low [102]. A general limitation of r-ABS is that the covariance matrix $\Sigma_A$ needs to be estimated. Despite the fact that it can be conveniently obtained from the atrial samples nearby the ventricular activity, the stationary assumption might break, leading to a poor estimate. Also, to fit properly the AR model, near-field atrial activity must be limited. Another limitation is that, while it is often reasonable to assume $\mathbf{a}_Q = \mathbf{z}_Q$, $Q$-windows might still contain ventricular activity. In this case a larger $N$-windows should be considered. Lastly, inverting directly the matrix $\Sigma_N$ or computing its determinant might be numerically challenging, and specific available numerical strategies should be adopted.

# 4
# Directed Network Mapping

## Contents



Networks can be used to describe systems which can be seen in a wide variety of fields like sociology, mathematics, economics, physics, biology, ecology, etc., which makes network theory a great framework to study a countless phenomena occurring in nature. However, only recently network theory has been applied with a goal to identify the sources of cardiac arrhythmias, despite the fact that directed networks naturally occur in the cardiac propagation patterns recorded by electrodes.

Methodologically, the challenge of analyzing cardiac propagation patterns is to determine the interrelationships between a larger number of signals, which is suitable for network analysis. In general, a network is composed of nodes which are connected through edges. In this context, it is possible to define nodes as

specific sites on the atrial surface, described by the recordings measured at the site, and to define the edges based on the interrelationship between two nodes, computed from the recordings. These interrelationship can be defined by a diversity of bivariate measures in the time and frequency domain, which were created with the interest in quantifying atrial organization.

In the time domain, a linear method for measuring the spatial organization was first presented by Botteron and Smith [110]. The cross-correlation function between all paired combinations of the signals were evaluated and the degree of linear coupling was estimated as the absolute peak of the cross-correlation function. In the frequency domain, the magnitude-squared coherence (MSC) has been employed to quantify the coupling between two signals [111, 112]. In the absence of noise, two linearly related signals will have an MSC equal to one at all frequencies, while two random, uncorrelated signals will have an MSC equal to zero. One drawback of the coherence approach is that long sequences are required for robust spectral estimation, resulting in a method with low time resolution, thus limiting its applicability. Sih et al. proposed an algorithm that measured synchronization between sites with the aim of obtaining high temporal resolution [113]. The method was based on quantifying linear relationships between short epochs (about 300 ms) of two different atrial signals. It predicted the samples of one signal through linear adaptive filtering of the other.

Cross-correlation, coherence and adaptive filtering were linear approaches to the analysis of the coupling between two signals, but to fully account for the complexity of the dynamics during AF, measures able to capture both linear and nonlinear interaction were developed. The studies of Censi et al. and Mainardi et al. estimated the degree of nonlinear coupling by performing specific multivariate embedding procedures [114, 115]. The degree of coupling can also be obtained by the means of the mutual-conditional entropy [116]. Another coupling measure, based on the concept of Granger causality, which was originally employed in econometrics, has been proposed by Hoekstra et al. [117].

Coupling in pairs of EGMs has also been quantified using methods based on the detected activation times. Barbaro et al. proposed an index based on the assumption that two atrial regions can be considered as coupled when they are depolarized by the same propagation wavefront [13]. Two atrial sites were defined as coupled if the delays between the detected activation pairs were lower than the maximum time required for a propagation wavefront to cover the distance between them, and if the temporal structure of the delays over a certain period was statistically different from a random phenomenon. A similar approach was proposed by Masè et al. who characterized the coupling between two atrial signals through a measure of the properties of the time delay distribution by the Shannon entropy [118].

All the studies described so far were dealing with the various measures between two atrial sites. They describe many possible approaches to the first fundamental step in the creation of the network, i.e. defining an edge between two nodes. However, none of these studies actually make use of the network theory, and to the best of our knowledge, there was not a large amount of research in applying the algorithms from network theory to understand cardiac arrhythmias, until very recently. The main advantage of applying network theory is the fact that a plethora of efficient algorithms already exist to "query" and analyze the model. Zahid et al. proposed to use the "minimum cut" algorithm based on network flow analysis to predict optimal ablation targets for left AFL [119]. Vandersickel et al. demonstrated the wide applicability of directed networks for the detection of driving mechanisms of cardiac arrhythmias (focal or reentrant) in both the atria and ventricles [120]. This work, along with some other approaches, is discussed in more detail in Section 4.9 (Discussion) of this chapter.

In this chapter, a technique called "directed network mapping", based on our preliminary work [121, 122], is formally defined and evaluated. Directed network mapping creates a directed network by processing intracardiac EGMs to model the electrical propagation on the atrial surface. Atrial conduction paths can be indeed identified based on the time delay between activations collected at two locations at close distance. Then, network theory algorithms can automatically identify

arrhythmia mechanisms from the network created. The goal of this study was to verify the applicability of directed network mapping for the identification of atrial arrhythmia mechanisms in both *in-silico* and clinical settings.

## 4.1 Creation of a directed network for electrical mapping

In this section, we described an algorithm to build the directed network from the unipolar EGMs and electrode coordinates (spatial positions) acquired during sequential mapping in an EP study. That is, we characterized the electrical propagation pattern in the atria with a corresponding network made of $M$ nodes. The main steps of the algorithm are illustrated in Figure 4.1.

The algorithm started by automatically selecting a set of $M$ network nodes equally distributed (as much as the geometry permits) on the entire atrial endocardial surface. The $i$-th node was defined by its spatial 3D position $\mathbf{p}_i = [x_i, y_i, z_i]$. In addition, for each node $i$, we expected its corresponding unipolar EGM $\mathbf{\Phi}_i$, collected at that spatial position $\mathbf{p}_i$. $\mathbf{\Phi}_i$ was the vector of the EGM samples.

The first step of the algorithm was the preprocessing of each EGM. As stated in Chapter 2, the major disadvantage of atrial unipolar recordings is the contamination of substantial far-field ventricular activity, that typically overlaps the signal of interest. For this reason, ventricular activity cancellation using r-ABS was performed, as described in the previous chapter. Figure 4.1C exemplifies the cancellation process on a single unipolar recording.

In order to model wave propagation into the network, only nodes spatially close to each other on the atrial surface were allowed to be connected through an edge. Delaunay triangulation technique can be applied to define the set of neighbors for each node $i$, hereafter mathematically defined as $\mathcal{B}_i$. However, as the atrial mesh was available from the EP study, instead of creating a Delaunay triangulation, the original mesh was downsampled to $M$ vertices, using the Meshtool software [123]. The downsampling procedure prevented spurious connections between anatomical regions that were not actually connected (e.g., between the body of the left atrial appendage

and the left PVs). Also, the downsampling algorithm adapted automatically the position of the nodes and their number to preserve the original shape. All nodes connected to the node $i$ through a triangle in the downsampled mesh were considered as neighbors. An example of neighbors determination is illustrated in Figure 4.1B.

The next step was to establish whether an edge from node $i$ to any of its neighbors in $\mathcal{B}_i$ had to be created based on the EGM at the nodes. We created a connection only if the conduction velocity, estimated for the electrical wave propagating between node $i$ and $j \in \mathcal{B}_i$, was within a physiological range. In other words, only electrical waves propagating in certain directions with respect to the vector connecting the nodes $i$ and $j$ were eligible to determine a connection. The conduction velocity criterion was defined as follows

$$\mathrm{CV}_{\min} < \mathrm{CV}_{ij} = \frac{d_{ij}}{\tau_{ij}} < \mathrm{CV}_{\max} \tag{4.1}$$

where $\mathrm{CV}_{\min}$ and $\mathrm{CV}_{\max}$ were set to 10 cm/s and 250 cm/s, according to physiological limits [9, 124]; $d_{ij}$ was the Euclidean distance between $\mathbf{p}_i$ and $\mathbf{p}_j$ in cm, and $\tau_{ij}$ was the time delay between $\mathbf{\Phi}_i$ and $\mathbf{\Phi}_j$ in seconds. The delay $\tau_{ij}$ was estimated using the cross-correlation function between $\mathbf{\Phi}_i$ and $\mathbf{\Phi}_j$. In particular, $\tau_{ij}$ was set as the time delay associated to the first maximum of the cross-correlation between the two signals. To reduce the effect of noise and spurious local morphology, before computing the cross-correlation, $\mathbf{x}_i$ and $\mathbf{x}_j$ were preprocessed with bandpass filtering ($3^{\text{rd}}$ order Butterworth, 40–250 Hz, zero phase), rectification, and lowpass filtering ($3^{\text{rd}}$ order Butterworth, 20 Hz, zero phase) [110]. Figure 4.1C illustrates how the preprocessing emphasized the activations in the signals as opposed to signal morphology. In case the delay $\tau_{ij}$ was negative and the absolute value of $\mathrm{CV}_{ij}$ was within the physiological range, the directed edge was created from node $j$ to node $i$ (instead of $i$ to $j$). As common in network theory, the connections between the nodes in the network are described using a connectivity matrix $\mathbf{C}$ with entries $c_{ij}$. The existence of a directed edge between nodes $i$ and $j$ was set by having $c_{ij} = 1$, and 0 otherwise.

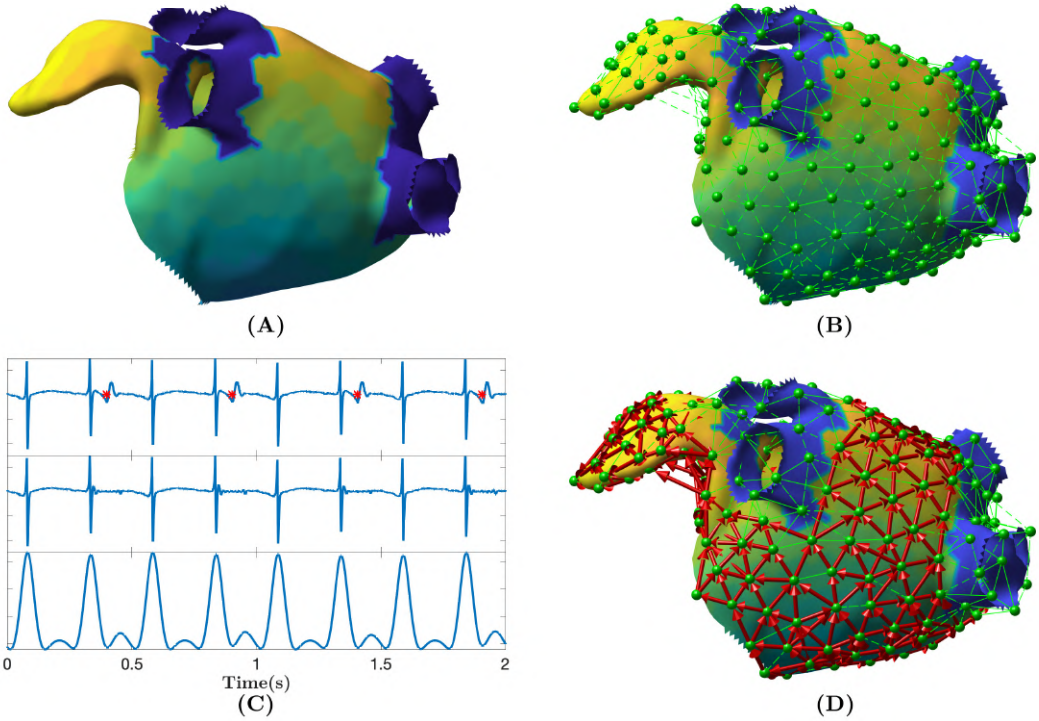


**Figure 4.1:** Depiction of the main steps of the directed network mapping technique. **(A)** Left atrial 3D model with LAT colormap. **(B)** Set of nodes (in green) equally distributed on the atrial surface with neighboring nodes connected using Delaunay triangulation. **(C)** Ventricular activity cancellation and preprocessing of one unipolar recording. The top panel of **(C)** shows original EGM and the time instants of the ventricular activity are marked in red. The middle panel shows the same EGM after performed cancellation. The bottom panel shows the result of the EGM filtering meant to emphasize the activations. The amplitude scale is in arbitrary units. **(D)** Final directed network (in red) after processing all the signals at each node to determine the existence and direction of the connections between nodes. The color map represents the LAT value across the atrial surface referenced to the activation of a specific node in the mesh. Adapted from [122].

In order to compute the time delay $\tau_{ij}$ using cross-correlation, the EMGs $\mathbf{\Phi}_i$ and $\mathbf{\Phi}_j$ had to contain at least one local atrial activation each. For each time window of length $l$, a network was created using the approach described so far. In addition, in order to detect sustained atrial arrhythmia, the creation of the network was repeated on consecutive windows (with possible overlap) and then were "averaged" to build a final directed network $\mathbf{A}$, whose entries were defined as follows:

$$a_{ij} = \begin{cases} 1 & \frac{1}{N}\sum_{n=1}^{N} c_{ij}^{n} \geq \frac{1}{N}\sum_{n=1}^{N} c_{ji}^{n} + \gamma \\ 0 & \text{otherwise} \end{cases} \tag{4.2}$$

where $N$ was the total number of networks "averaged", $c_{ij}^{n}$ the entry in the

connectivity matrix $\mathbf{C}_n$ for the $n$-th network, and $\gamma \geq 0$ a threshold parameter. A connection in $\mathbf{A}$ was established from node $i$ to node $j$, setting $a_{ij} = 1$, if the average connection strength $\sum_{n=1}^{N} c_{ij}^n/N$, in direction $i$ to $j$, was larger than the average connection $\sum_{n=1}^{N} c_{ji}^n/N$, in the opposite direction, $j$ to $i$, plus a small positive safety threshold $\gamma$, used to avoid random connection, due to noise, to appear.

Finally, the output of the algorithm described in this section comprised two networks, i.e., the directed network resembling the electrical propagation $G_{\text{prop}} = (V_{\text{prop}}, E_{\text{prop}})$ and the undirected network describing the triangular mesh $G_{\text{mesh}} = (V_{\text{mesh}}, E_{\text{mesh}})$. It is worth noting that the two networks shared the same nodes, i.e., $V_{\text{prop}} = V_{\text{mesh}}$. Figure 4.1 depicts an example of both networks.

## 4.2 Detection of cycles in the directed network

Having at disposal the directed network corresponding to an electrical mapping, macroreentries can be found by detecting cycles (i.e., closed-loops) in the network. A cycle $\mathcal{L}$ is defined as a non-empty sequence of nodes linked by directed edges in which the first and last node coincide. A standard depth-first search (DFS) algorithm was used for the purpose of detecting the cycles.

We empirically noticed that a few macroreentries were not identified because a single edge was missing in the directed network. In order to mitigate this problem (possibly occurring in longer sequences), a new algorithm for cycle detection tolerant to gaps of a single edge was developed. In particular, we leveraged the fact that the DFS algorithm was very efficient in finding cycles.

The algorithm works as follows. Given a node $i$ in $V_{\text{prop}}$, the directed edges connecting each node in $\mathcal{B}_i$ with $i$ were temporary set, and the DFS algorithm was run in this modified network to find the cycles. This step was repeated for all the nodes in $V_{\text{prop}}$ and all cycles found were merged. The algorithm was able to detect the macroreentries previously missed. The drawback of this procedure was the identification of many cycles similar to each other.

Given the large number of nodes in the network, as well as gap tolerance, in real applications, the cycle finding algorithm may provide cycles that are very similar to

each other, and differ only by a few nodes (in many cases, just one). These cycles belong to the same anatomical region and, in practical terms, should be considered as a single one. A network-based grouping algorithm of these cycles, based on the amount of nodes shared, was designed by means of the following three steps.

First, the amount of shared nodes between cycle $h$ and $k$ was computed as follows

$$w_{hk} = \frac{\#\mathcal{L}_h \bigcap \mathcal{L}_k}{\sup\{\#\mathcal{L}_h, \#\mathcal{L}_k\}} \tag{4.3}$$

where # was the cardinality of a set, $\#\mathcal{L}_h \bigcap \mathcal{L}_k$ represented the number of nodes shared between $\mathcal{L}_h$ and $\mathcal{L}_k$, that were then normalized by the length of the longest cycle. Hence, the quantity $w_{hk}$ was bounded, by construction, between 0 and 1.

Second, each $w_{hk}$ was used to build a further undirected graph whose nodes were cycles. A connectivity matrix $\mathbf{W}$ was built using the values of $w_{hk}$. In the graph, the edge between cycle $h$ and $k$ existed only if $w_{hk}$ was greater than a certain threshold $t$. Intuitively, a low value of $t$ facilitates the merging of the cycles. In our study, $t$ was empirically set to 0.7 by visual inspection of the grouping algorithm results (the sample size limited the extensive evaluation).

Third, a standard algorithm based on DFS was applied to locate connected components in the undirected graph just created. A connected component of an undirected graph is a set of nodes such that each pair is connected by a path. All the cycles belonging to the same connected component were grouped together and considered to represent the same reentry.

## 4.3 Directed network mapping for sequential data

In the clinical setting, ablation procedures are guided by the results of electro-anatomical mapping. Data are derived from recordings of multielectrode catheters, which are moved inside the atria to map the relevant regions and guide the intervention. Several catheter configurations are available on the market, and usually present a few electrodes (in the range of a few tens). With this typical setting, only snapshots of a few seconds of EGMs in the current position of the

electrodes become available. In order to map the electrical activity of both atria, sequential mapping is used to construct both voltage and activation maps. The latter is built by using a temporal reference, usually the QRS complex of the surface electrocardiogram (ECG) or the activation detected in a catheter inserted in the CS, to temporally align the activations identified within successive snapshots for each electrode. In addition, the positions of the electrodes are also tracked over time, with a magnetic- and impedance-based navigation system, thus allowing the construction of a 3D map of the geometry and of the electrical activation. In our study, we (retrospectively) utilized the data collected via sequential mapping to create a directed network that models the electrical propagation during AFL.

Sequential mapping brings two issues for directed network mapping. First, the number of atrial locations at which EGMs are collected is typically too large for building a directed network meant to model the electrical propagation. Many of these EGMs are acquired on locations very close between each other. However, current navigation systems report localization errors of about 1 mm [125]. Hence, the electrical propagation between very close electrodes cannot be estimated reliably. In addition, a large number of nodes prevents the network to be efficiently processed by the network theory algorithms, thus hampering the use of the technique during EP studies. Second, the recordings are not acquired concurrently at the same time (EGMs are collected sequentially with the same probe, which is moved).

In order to tackle these two issues, a coarsening procedure was designed to build a network composed of a smaller number of nodes $M$, each associated with an EGM temporally aligned with the others. We proceeded as follows. First, having at disposal a virtual anatomy (output of the EAM during ablation), we downsampled the original atrial mesh to $M$ points using the approach described in Section 4.1. The output of this step were the 3D coordinates $\mathbf{p}_i$ of each node, each contained in a triangular tessellation involving the neighboring ones. The next step was to assign the electrical activities measured by the moving catheter to each $\mathbf{\Phi}_i$. The position and electrical activity of each electrode on the catheter were tracked over time. Let $\tilde{\mathbf{p}}_{en}$ and $\tilde{\mathbf{\Phi}}_{en}$ be the 3D position and electrical activity of electrode $e$ at time index

$n$, respectively. The assignment was performed by i) checking whether the average position of the electrode was near to one of the nodes $\mathbf{p}_i$; and ii) the 3D coordinates of the electrode did not vary in the window of observation (i.e., the maximum range of movement of the catheter across axes did not exceed a given threshold). The window was defined as $l$-samples-wide and centered on the reference CS catheter activation times. More formally, let $\mathcal{W}_q$ be the set of $l$ time indices centered on the $q$-th CS activation (where $\#\mathcal{W}_q = l$, $\forall q$). The voltage samples $\tilde{\mathbf{\Phi}}_{en}$, collected with the electrode $e$ in the window of observation (i.e., $n \in \mathcal{W}_q$), were assigned to the node $i$ if the two following conditions were matched

$$\begin{aligned} \left\| \mathbf{p}_i - \frac{1}{l} \sum_{n \in \mathcal{W}_q} \tilde{\mathbf{p}}_{en} \right\| &< r_1 \\ \max_{x,y,z} \left( \max_{n \in \mathcal{W}_q} \tilde{\mathbf{p}}_{en} - \min_{n \in \mathcal{W}_q} \tilde{\mathbf{p}}_{en} \right) &< r_2 \end{aligned} \tag{4.4}$$

where $r_1$ and $r_2$ were two thresholds set to assess the closeness to the node of the electrode and its position stability in time. Considering the distances between the network nodes, they were empirically fixed at 6 mm and 2 mm, respectively. The max and min operators assessed the maximum and minimum values, along a given axis, of a vector or matrix, respectively.

This procedure may assign multiple signals to each node due to the presence of many CS activations and the many EGMs collected. In order to determine whether the directed edge should be created from node $i$ to $j$, the delays between all pairs of signals associated with node $i$ and $j$ were computed using the procedure described in Section 4.1, and a t-test was performed to verify if the average delay was significantly different from 0 ms (significance level $\alpha$: 0.05). Then, if the difference was statistically significant, the edge was created only if the conduction velocity associated with the average delay was within the physiological range, as assessed by equation (4.1).

For activation detection, we applied a threshold to the preprocessed (Botteron approach as described in Section 4.1) CS reference signal $z(n)$. The threshold $\theta_i$ was set at the time instant of the last detected activation $n_i$, and was held fixed until it was exceeded and a new activation was detected. It was calculated based

on the exponential average for the peak amplitudes of the previously detected activations [66],

$$\theta_i = \alpha\mu_i, \quad \mu_i = \mu_{i-1} + \beta(z(n_i) - \mu_{i-1}), \quad i >= 1,$$

where $\mu_i$ is the exponential average, $z(n_i)$ represents the peak amplitude of the most recently detected activation, the parameter $\beta$ defines the rate with which the threshold can change, and the parameter $\alpha$ determines the fraction of $\mu_i$ to be used in the threshold computation. When the preprocessed signal exceeds $\theta_i$, a new activation is detected. The time instant of the first local maximum following the activation served as an estimate of the activation time.

## 4.4 Validation in sinus rhythm

Directed network mapping was first validated using data from two subjects in SR (ages 67 and 54, both male). The data were collected from Fondazione I.R.C.C.S. Ospedale Maggiore Policlinico in Milan, Italy. EAM was performed using multielectrode catheters and the CARTO® 3 (Biosense Webster) navigation and mapping system. To allow correct local EGM assessment, the default protocol mandated that the mapping catheter was maintained in each location for 2.5 s after points were acquired. Although patients were paroxysmal AF cases undergoing PVI, they were in SR during the mapping and had no prior known substrate modifications. The CARTO® 3 system provided activation maps in the form of local activation times. Every patient that underwent EAM and ablation procedure had signed an informed consensus statement about periprocedural risk and about the use of clinical data for clinical research in the respect of privacy policy. A directed network map was built as described in the previous section and the results checked by visual inspection, comparing the connections of the network (connectivity matrix) with the activation map.

## 4.5 Validation in simulated AFL cases

Next, we validated the directed network mapping algorithm in simulated AFL scenarios. To do so, based on simulated AFL mechanisms implemented in a previous work by [126], we retrospectively analyzed 6 different computational AFL scenarios. These simulations included right AFL as well as left AFL forms, like macroreentries around the valves and across the roof. A complete list of scenarios is provided in Table 4.1.

**Table 4.1:** List of simulated AFL mechanisms. CW=clockwise, CCW=counterclockwise

| No. | Atrium | Mechanism | Position | Direction |
|---|---|---|---|---|
| 1 | Right | Macroreentry | Tricuspid valve | CCW |
| 2 | Right | Macroreentry | Tricuspid valve | CW |
| 3 | Left | Macroreentry | Mitral valve | CW |
| 4 | Left | Figure-of-eight | Left and Right PVs | Anterior |
| 5 | Left | Figure-of-eight | Left and Right PVs | Posterior |
| 6 | Left | Figure-of-eight | Right PVs | Anterior |

Cardiac excitation was modelled using the fast marching approach to solve the Eikonal equation [127, 128]. The atrial electrophysiological activity was simulated on the triangulated volumetric mesh of a bi-atrial anatomy (Figure 4.1A), generated from segmented magnetic resonance imaging data of a healthy subject [129]. Inter-atrial connections and fiber orientation were generated by a rule-based algorithm [130, 131]. Scars were added circumferentially around ipsilateral PVs representing ablation scars from the previous pulmonary vein isolation intervention. The simulations were initiated by manually placed triggers and refractory areas. They were continued at least 5 s to confirm a stable excitation pattern. The simulated excitation resulted in a LAT for each anatomical node that was not isolated. Spatio-temporal transmembrane voltage distributions were derived from the activation times using the Courtemanche human action potential model adapted to AF conditions [131].

For each scenario, we distributed 400 equidistant nodes on the endocardial surface: half of them in the left and the other half in the right atrium (with 7.8 mm average distance between two neighboring nodes). The spatial distribution of nodes is visible in Figure 4.1B. The 3D coordinates of the nodes, along with corresponding synthetic unipolar EGMs, were used as input to the network mapping algorithm. The unipolar pseudo-EGM $\Phi_i$ for the $i$-th node was calculated using the infinite volume conductor approximation:

$$\Phi_i(x,y,z) = -\frac{1}{4\pi}\frac{\sigma_{\text{intra}}}{\sigma_{\text{extra}}}\int\int\int \nabla V_m(x',y',z')\cdot\nabla\left(\frac{1}{r}\right)\,dx'dy'dz' \tag{4.5}$$

where $\sigma_{\text{intra}}$ is the intracellular conductivity (within the cardiac tissue), $\sigma_{\text{extra}}$ the extracellular conductivity (within the whole domain), $\nabla V_m(x',y',z')$ is the spatial gradient of the transmembrane voltage in the point with coordinates $x'$, $y'$, $z'$ [132]. The values of $\Phi_i(x,y,z)$ computed over time were then stored in the vector $\mathbf{\Phi}_i$.

The results were validated by locating the cycles in the network (section 4.2) and visually comparing their locations with the LAT map produced by the simulated mechanism.

## 4.6 Validation in clinical AFL cases

The directed network mapping algorithm was retrospectively validated on 10 patients (age: 66 ± 5 years; male/female: 7/3) with AFL who underwent an EP study and RF catheter ablation. The subjects selected by the clinicians were all complex AFL cases who had a history of AF and at least a previous PVI or additional substrate modifications. The study was done using a 64 mini-electrode small basket array (IntellaMap Orion™, Boston Scientific) that enabled rapid high-density mapping. The cases were provided by Städtisches Klinikum Karlsruhe, Germany and included 2 AFL scenarios in the RA and 8 in the LA. The complete list of clinical cases is provided in Table 4.2. Data collection was performed according to the Helsinki Declaration guidelines on human research. The research protocol used in this study was reviewed and approved by the local review board. All patients provided written informed consent.

**Table 4.2:** Complete list of analyzed clinical AFL cases. CW = clockwise, CCW = counterclockwise.

| No. | Atrium | Suspected mechanism | Description |
|---|---|---|---|
| 1 | Right | Tricuspid valve reentry CCW | The patient had previous PVI. |
| 2 | Right | Tricuspid valve reentry CCW | The patient did not have previous PVI. |
| 3 | Left | Mitral valve reentry CW | The patient had previous PVI with anterior block line from MV to left superior PV. A gap was detected in the block line. |
| 4 | Left | Mitral valve reentry CW | The patient had previous PVI with posterior roof block from left superior PV to right superior PV and an anterior line from MV to left superior PV. A gap was detected in the anterior block line. |
| 5 | Left | Mitral valve reentry CW | The patient had previous PVI. Gaps were found in the PVs from the previous ablation. |
| 6 | Left | Microreentry around PVI gaps | The patient had previous PVI. Gaps were found in both left and right PVI of the previous ablation. |
| 7 | Left | Figure-of-eight macroreentry around left and right PVs | The patient had previous PVI. Gaps were found in both left and right PVI of the previous ablation. |
| 8 | Left | Figure-of-eight macroreentry around left and right PVs | The patient had previous PVI with the the FIRM system based on rotor detection. Small areas of block in septal area. |
| 9 | Left | Figure-of-eight macroreentry around left and right PVs | The patient had previous PVI. Gaps were found in both left and right PVI of the previous ablation. |
| 10 | Left | Macroreentry around right PVs | The patient had previous PVI with anterior block line from MV to left superior PV. Gaps were detected in the right PVI and in the anterior block line. |

Each AFL case was analyzed offline retrospectively, after the intervention, by directed network mapping, after exporting all EGMs and the corresponding 3D coordinates from the EAM system. Only data collected before the actual ablation were analyzed. A degree of rhythm stability during the mapping phase is assumed to properly build an average direct network, which is typically true for AFL cases.

For each case, the average directed network was created by following the steps reported in Section 4.1. Briefly, atrial meshes provided by the EAM system, were downsampled to 114(107, 136) [median (interquatile range)] nodes. Then, for each CS activation, $N = 5$ different networks were created using a sliding window of length $l$, defined as half of the average distance between CS activations, with overlap of 100 ms. Given the time index $n_q$ of the $q$-th CS activation, the sliding window started at $n_q - l/2 - 200$ ms and was moved ahead 4 times with a stride of 100 ms. All networks were then "averaged" to obtain the average directed network. The safety threshold $\gamma$ was tuned to the value of 1, to avoid eventual random connections that could appear due to noise. Once created, cycles were detected and then grouped together according to the algorithm described in Section 4.2.

We finally compared the cycles found in the directed network with the clinical report of the patient. The clinicians provided information about the suspected AFL mechanism (as hypothesized after the successful ablation) and the corresponding part of the atrium involved (see Table 4.2). Depending on the suspected mechanism, we analyzed only the groups of cycles with a certain minimum number of nodes. In particular, in case of macroreentries, only cycles with at least 10 nodes were considered. On the other hand, for microreentry (case number 6), only cycles with less than 10 nodes were considered, but also without the gap tolerance. The evaluation of the correspondence between what was found by our algorithm and the clinical report was performed a posteriori together with the clinician (the algorithm was run only once and before having any knowledge of the clinical reports; it was not adapted to the specific mechanism at hand).

## 4.7 Validation in simulated AF case

A realistic 3D model of the human atria that included heterogeneity at cell, tissue and organ scale was used [133]. The model includes different anatomical regions with their respective fiber orientation. This computational finite element model is composed of linear hexahedral elements with a regular spatial resolution of 300 $\mu$m. For additional details about the model see [133]. The cellular electrical activity is modelled by the Courtemanche-Ramírez-Nattel ionic model [134]. In order to reproduce transmembrane potential ($V_m$) of experimentally observed heterogeneity in action potential (AP) morphologies and duration in the different atrial regions, the conductances of three specific ionic currents were adjusted for 8 different regions in both atria [133, 135]. This procedure generated nine different cellular models and the AP duration variation among regions was similar to experimental observations [136]. The electrical propagation was solved by the mono-domain formalism using the operator splitting numerical scheme (constant time step of 0.01 ms) with the ELVIRA solver [137]. The simulations were run on a computing node with sixty-four 16-core Intel® Xeon® Gold 6130 clocked at 2.10 GHz.

A sustained high frequency train of stimuli (100 ms cycle length) was applied in the RA, close to the CS. This led to a complex fibrillatory pattern with the presence of reentrant drivers. We were able to observe two rotors, one in the RA, very close to the SVC, and the other in the LA, in between the left PVs and the left atrial appendage. Figure 4.2 shows the simulation snapshots that display direction of wave propagation and the rotor in the left atrium. The simulation was run for a total of 6 s. Unipolar EGMs were computed on the endocardial surface as extracellular potentials, with a temporal resolution of 1 ms, in a whole atrial-torso model [133]. We computed 400 EGMs, equidistant from each other: half of them in the left and the other half in the right atrium (with 6.5 mm average distance between two EGMs).

AF usually manifests as reentrant circuits propagating through the whole atria creating non-stationary chaotic activation patterns. In order to handle these non-stationary characteristics of AF, we proceeded as follows. After all the signals were

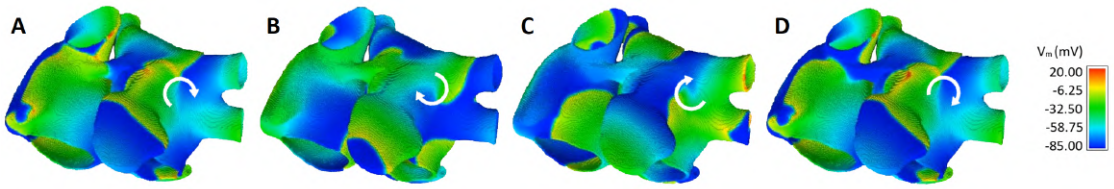


**Figure 4.2:** Simulated AF case. Four snapshots of the simulated transmembrane voltage ($V_m$ [mV]) in the 3D atrial model at times: **A** $t$, **B** $t + 33$ ms, **C** $t + 66$ ms, and **B** $t + 99$ ms. It is possible to observe a rotational activity in the left atrium, between the left PVs and the left atrial appendage (white arrow). Adapted from [121].

preprocessed and the neighbors were set, each of the EGMs were divided into 300 ms time segments, using a sliding window of 100 ms. This resulted in total of 58 different time segments for our 6 s simulation. Then, for each of these time segments, directed network mapping was performed and a specific network was generated. This concept is the same as averaging described in Section 4.1 but here the signals are divided across the entire signal duration, instead of just dividing on the shorter time segment centered around the CS activation. In fact, here we exploited the availability of many EGMs recorded concurrently in the computerized simulation. During the sequential mapping this task is more challenging and requires some further investigation.

Once the networks were created, any type of rotational activity could be found by detecting cycles in the networks. In order to find the center of the rotor, we looked for the smallest possible cycles in the networks, i.e. cycles that contain only three nodes. After finding all the smallest cycles in all the networks, we counted how many times the same cycle repeated throughout different networks (that represent different time frames). The cycles repeating in consecutive networks pointed us to the location of a stable rotor. It is also worth noting that it is possible to search for larger cycles (that contain more than three nodes) in the networks, as larger cycles may reveal somewhat larger area of the rotor's influence.

## 4.8 Results

The directed network mapping algorithm was first tested on the left atrium of the two patients in SR and provided a result in line with the expectation. The electrical propagation started in the septum, propagated along both the anterior and posterior

wall and ended around the left PVs. The LAT map provided by the CARTO® 3 system confirmed that the propagation found was properly detected. Figure 4.3 shows a few examples of the electrical propagation (red arrows) superimposed over the LAT map.

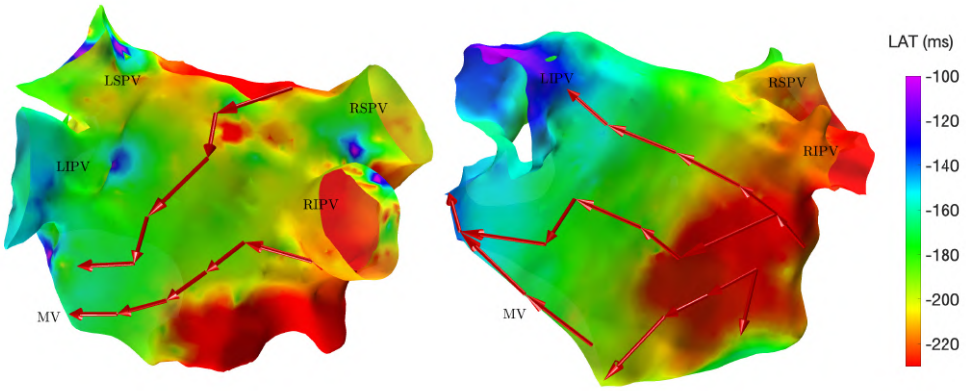


**Figure 4.3:** Electrical propagation pattern detected by directed network mapping (red arrows) superimposed over the LAT map (exported from CARTO® 3) for two subjects in sinus rhythm in posterior view. LSPV=left superior PV, LISP=left inferior PV, RSPV=right superior PV, RIPV=right inferior PV, MV=mitral valve.

The efficacy of the directed network mapping was also tested in 6 different simulation settings involving several types of AFL, induced on a 3D anatomical model of both atria. In each of the 6 setups, the algorithm was able to precisely detect the expected reentrant paths around the anatomical obstacles (see Figure 4.4).

A directed network was retrospectively created for each of the 10 EP studies recorded during ongoing AFL.

The first two clinical cases presented TV reentry with typical AFL (case 1 and 2). Directed network mapping detected 46 different cycles in case 1, and 183 in case 2, with two groups identified for both cases, a cycle group around the TV and another one around the IVC. This was in line with what was found in simulation 1 and 2. These two cycles commonly appear together, and they are clinically treated by performing an ablation line at the floor of the RA between the inferior tricuspid annulus and the IVC (cavotricuspid isthmus - CTI). These

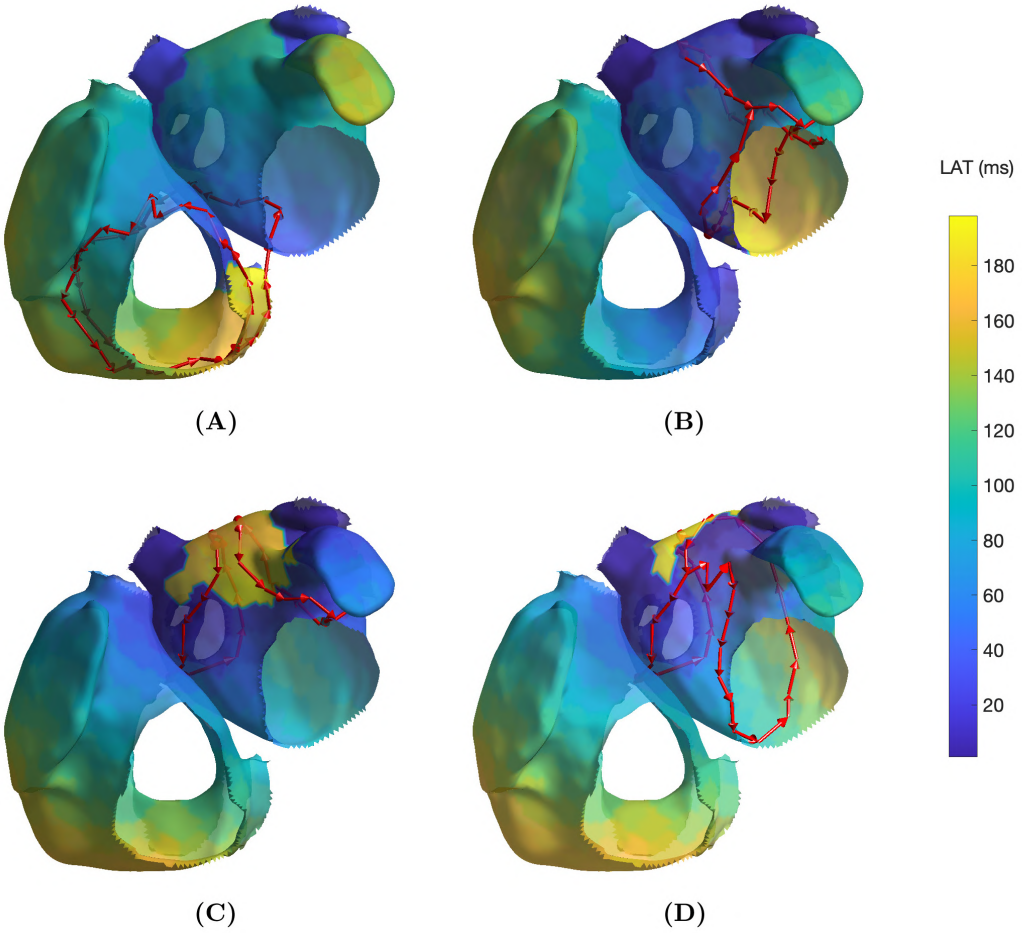


**Figure 4.4:** Cycles found on 4 AFL simulations: **A**, Macroreentry on tricuspid valve CCW (simulation 1), **B**, Macroreentry on mitral valve CW (simulation 3), **C**, Figure-of-eight around both PVs in anterior direction (simulation 4) and **D**, Figure-of-eight around right PVs in anterior direction (simulation 6; the threshold $t$ was set to 0.45 for visualization purpose). Only one cycle randomly selected from each group has been plotted. The color map represents the time interval between the initial time of the stable phase of the simulation and the first atrial activation in each node.

two cases fully matched the expectations of the clinicians. Figures 4.5a and b report the results of cases 1 and 2.

Cases 3, 4 and 5 were left atrial reentries around the MV in clockwise direction. In case 3, directed network mapping detected 20 different cycles but none of them was found around the MV. Two groups of cycles were detected around the left PVs in counterclockwise direction. We detected that some edges around the MV were not built by the algorithm, while most of the nodes were properly connected to form

a cycle around the valve. This happened even considering the gap algorithm in place (one edge gap was not sufficient). Regarding the detected cycle, it commonly appears when MV reentry is present. Similar results were found in simulation 3 (see Figure 4.4B). In both cases 4 and 5, a single cycle group (with 17 cycles in case 4 and 9 in case 5) around the MV was found and none was identified around the left PVs. This result was as expected. Indeed, for case 4 the clinical report stated that a posterior roof block line from the left superior PV to the right superior PV was made in a previous ablation, which would prevent any rotation around the left PVs. Figures 4.5c, d and e show the cycles identified for cases 3, 4 and 5.

In case 6, as reported in the clinical report, during the EP study, a total of three gaps were found in the previous PVI ablation lines. Two gaps were found in the left PVI line where a localized microreentry mechanism involving both gaps could be detected. The right PVI line presented with a single posterior gap. The excitation wave-front was meandering with a reduced conduction velocity through the gap. The algorithm found a total of 4 cycles, with either 3 or 4 nodes, belonging to two different groups: one group near the left superior PV and other one near the right inferior PV. These cycles pointed to the gaps reported in the previous PVI ablation, and the case matched the expectations of the clinicians. Figure 4.5f shows the cycles identified for the case 6.

Cases 7, 8, 9 were suspected figure-of-eight macroreentries around left and right PVs. In all these cases, the algorithm correctly detected the propagation pattern around the PVs. In particular, in case 7, two groups of cycles rotating around left and right PVs were found, but also with 3 additional cycles with $\geq 10$ nodes found traveling around both right PVs individually, as reported in Figure 4.6a. On the other hand, in case 8, along with two groups of cycles around the PVs, an additional cycle group on the anterior side of the right superior PV was found. Figure 4.6b reports the results for this case. Then, in case 9, there were two cycle groups for each pair of PVs, as shown on Figure 4.6c.

Finally, in case 10, the algorithm found two groups of cycles with at least 10 nodes. The cycles belonging to both groups were revolving around right inferior PV, in sort

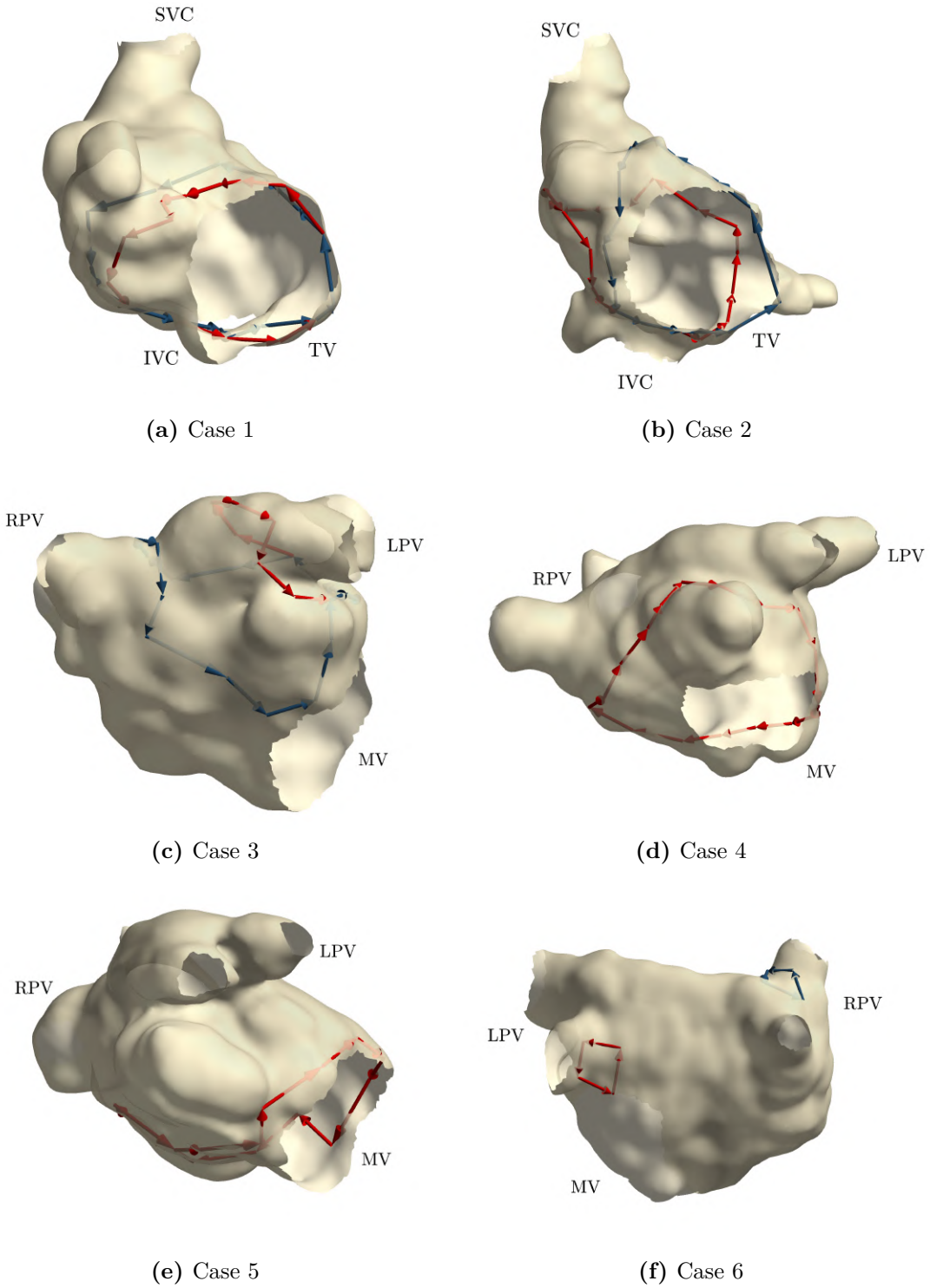


**(a)** Case 1 **(b)** Case 2

**(c)** Case 3 **(d)** Case 4

**(e)** Case 5 **(f)** Case 6

**Figure 4.5:** Cycles found on six clinical AFL cases. Arrows depict the reentry identified by directed network mapping with arrow colors representing cycles of different groups. Among all cycles in a group, only the one with a minimum average Menger curvature is reported. Panels **a-f** correspond to cases 1-6 of Table 4.2, respectively.

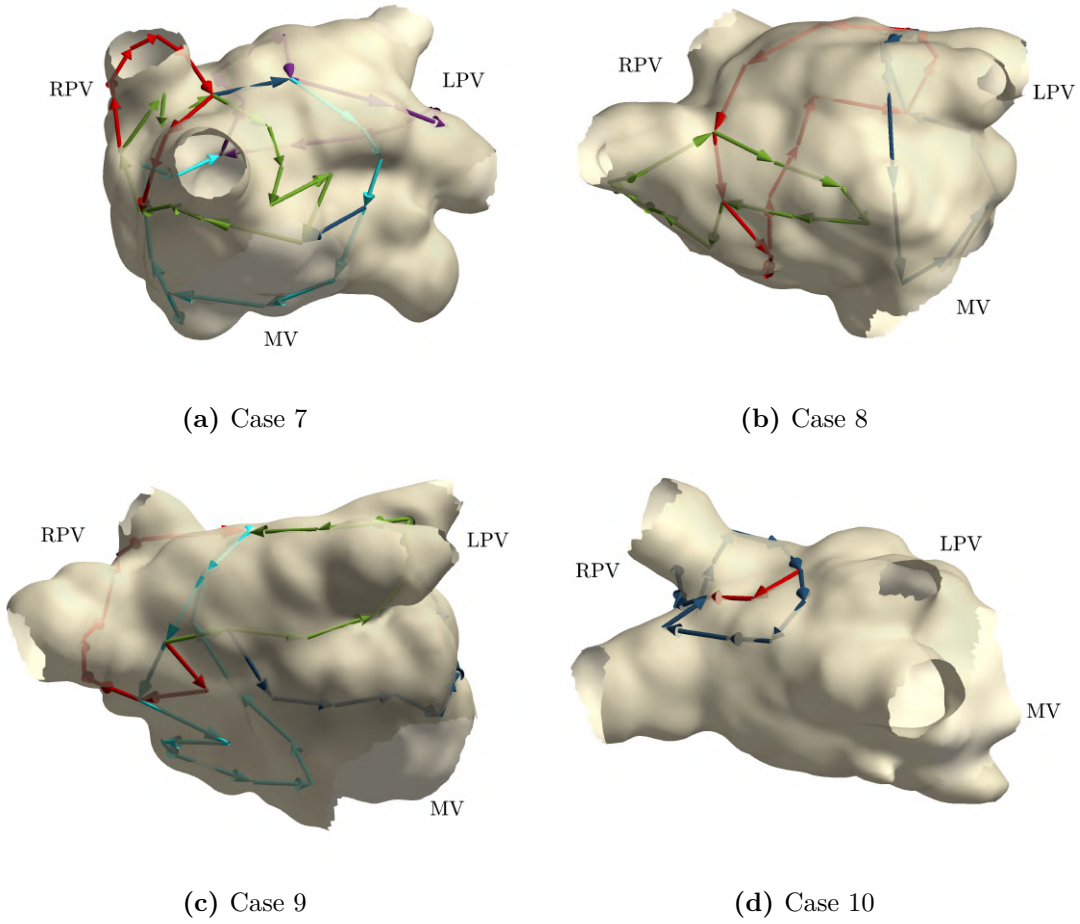


**(a)** Case 7 **(b)** Case 8

**(c)** Case 9 **(d)** Case 10

**Figure 4.6:** Cycles found on four clinical AFL cases. Arrows depict the reentry identified by directed network mapping with arrow colors representing cycles of different groups. Among all cycles in a group, only the one with a minimum average Menger curvature is reported. Panels **a-d** correspond to cases 7-10 of Table 4.2, respectively.

of concentric fashion. The mechanism was coherent with the identified gaps in the right PVs reported in the clinical report. Figure 4.6D reports the results of this case.

To summarize, the algorithm identified the exact same mechanism and its location, as reported in the clinical study, in 9 cases, and failed to identify the correct mechanism in 1 case (No. 3).

Regarding the simulated AF scenario, in the left atrium, across all 58 networks (representing different time frames), we detected a total of 97 cycles of three nodes. Most of these cycles occurred only in one or two networks, so they were not considered as candidates for the rotor location. We only considered those cycles that occurred seven or more times (900 ms or more), and they are reported in

Figure 4.7a. The most frequent cycle occurred in 19 networks, there were two cycles that occurred 10 times, two cycles that occurred 9 times, three cycles that occurred 8 times and finally three cycles that occurred in 7 networks. Additionally, we took into account which of these occurrences were in consecutive networks (see Figure 4.7a). The longest sequence of consecutive occurrences was relatively low (less than 5 networks) in all but two cycles that occurred in 9 and 10 consecutive networks. These two cycles were considered as top candidates for the rotor location. They were positioned in the same region right next to each other, even though they

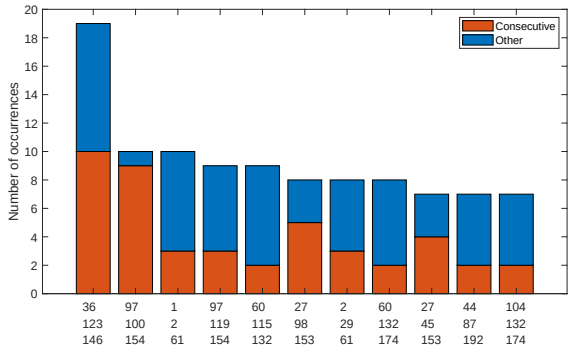


**(a)**

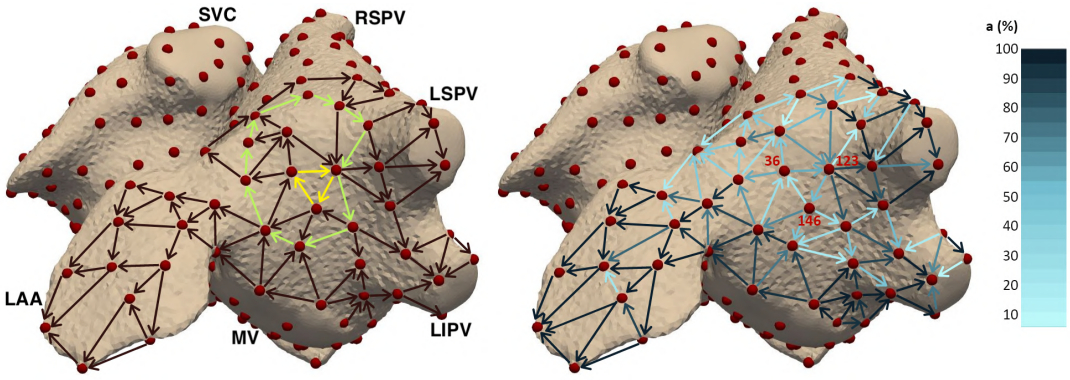


**(b)** **(c)**

**Figure 4.7:** Panel **(a)** shows the bar chart of graphs that contain cycles with exactly three nodes that occurred in 7 or more time frames. IDs of the nodes are contained on horizontal axis, and number of occurrences is on vertical axis. Red color indicates the longest sequence of consecutive occurrences. Panel **(b)** shows a portion of the network mapped in the rotor's region, generated for the single time interval (4100 ms to 4400 ms of simulation). Red dots represent EGMs and arrows represent their connections. The smallest cycle, made of 3 nodes and indicated in yellow, detects the center of the rotor. The bigger cycle, indicated in light green, shows the larger area of influence of the rotor. Panel **(c)** shows a portion of the result obtained by network averaging formula, focusing on the region where the rotor is located. The cycle with the largest number of occurrences (36,123,146) is visible. Adapted from [121].

did not share any common node. Interestingly, this region was the same one in which we already visually observed the existence of a rotor, looking at the electrical propagation map, produced by numerical simulations (see Figure 4.2a). Figure 4.7b and 4.7c show a portion of the result obtained in a single time frame and by network averaging formula, both focusing on the region of the rotor. The averaged network contained only two cycles with three nodes, and those two were the same ones we considered before as top candidates for the rotor location. In this region, we were also able to find cycles with more than three nodes in the averaged network.

## 4.9 Discussion

In the present work, we verified that directed network mapping can be used to properly detect different types of atrial arrhythmia mechanisms. The method was applied to a broad range of simulations and clinical cases. First, we showed that directed network mapping can be used to accurately represent the electrical propagation pattern in SR. Second, directed network mapping was able to correctly locate reentries in in-silico AFL and AF models, where we tested 7 different scenarios. Finally, we tested the technique on 10 clinical cases of AFL and compared the results with clinical reports by expert electrophysiologists. Overall, the algorithm proved to be satisfactory according to the clinicians' opinion with respect to the complex cases analyzed and has potential for clinical use. In fact, in addition to the fully identified cases (9/10), it is worth noting that the mechanism of the remaining case (No. 3) was actually detected by the algorithm but not in their entirety, as we correctly identified the gap in the anterior block line, that was responsible for the mechanism in place. This makes it difficult to classify the performance of the algorithm with simply "identified" or "not identified". For this case, physicians may still get useful insights on the underlying mechanism and thus considering the goal as achieved.

Regarding the missed mechanism around the MV for case 3, we detected, by visual inspection, that a few edges around the MV were not built by the algorithm, while all other nodes were properly connected to form a cycle around the valve. We found that the histogram of the temporal delays between nodes in the disconnected

region displayed a bimodal distribution with positive and negatives delays. The respective modal delays had a conduction velocity within the range to construct the edge, however, the t-test failed due to an average delay close to 0 ms. A hypothesis to explain this phenomenon could be related to the presence of slow conducting areas in the surrounding of the gap in the anterior line. These areas might have created a periodic oscillation of the delays of two neighboring nodes with respect to the CS activation. We leave the investigation of this hypothesis for future works.

In this study, the majority of clinical cases we investigated were AFL macroreentries. However, the technique showed some potential for microreentries as well. In fact, a few cycles of the smallest allowed dimension (i.e., 3 to 4 nodes) were detected for the clinical case 6. The atrial area involving microreentries has been found to vary from few millimeters up to 2-3 centimeters in diameter. For example, Jais et al. reported evidence of slow conducting areas as small as 2 centimeter around which a reentry was observed [138]. Furthermore, in 2020, Mantovan et al. were the first to report a microreentry circuit confined to a region size of a couple of millimeters [139]. These areas range from 3 $mm^2$ to 300 $mm^2$. In our clinical cases, the average distance between nodes was 16.8 mm, that corresponded to a reentry with an area of approximately 120 $mm^2$, hence the actual dimension of the smallest detected cycles was in line with what previously reported.

Over the years, network theory has had many different applications, but to the best of our knowledge, there was not a large amount of research in this domain to understand cardiac arrhythmias, until very recently. In the study by Vandersickel et al., directed networks were used to describe electrical excitation to extract the arrhythmia mechanism [120]. In their work, the authors established a proof-of-concept using *in-silico* simulations of several activation patterns and clinical data of atrial tachycardia (AT) to demonstrate the wide applicability of directed networks in this domain. In their very recent follow-up study, authors evaluated the diagnostic accuracy of their method in more complex AT cases [140]. They retrospectively analyzed 51 AT cases and compared the diagnoses made by their method with those of the experts based on high-density activation maps.

They showed that cardiac mapping based on network theory could outperform high density activation mapping for specific types of AT (e.g., localized reentry), whereas for macroreentries, the directed network performed similarly to experts. These results hint that directed network may be a valuable tool during EP studies.

Our algorithm and the one proposed by Vandersickel et al. share the same goal, i.e., modeling the electrical propagation through directed networks and exploiting network theory to infer information about the arrhythmia mechanisms. Inspired by their study, we investigated the use of directed network mapping for AF characterization and rotor detection in computerized simulations [121]. However, during AF, the creation of network based on LAT maps as proposed by Vandersickel et al. become a difficult task. We then designed an algorithm directly estimating the time delay between activations recorded in nearby sites using a cross-correlation based algorithm. This approach was found to be more reliable with respect to computing the difference between LAT values in different sites [24, 141]. Motivated by these preliminary results, we started investigating on the applicability of directed networks for the identification of macroreentries in AFL. This problem required the implementations of a DFS algorithm for cycle detection, a grouping algorithm for cycles in similar locations, and a study specifically designed to test the algorithms on clinical cases: the work described in this chapter. Another contribution by the same research group shares some more similarities with our analyses [140]. First, both our work and theirs tested the capability of a directed network to correctly detect and group cycles. In this regard, our approach was based on a secondary graph taking into account the position of all nodes in the cycles, whereas they proposed a clustering technique based solely on the centroid of the cycles, that might group cycles with different orientations and with similar centers. Second, even though we both analyzed complex atrial arrhythmias, the objectives of the studies were different. Our study was focused on the validation of the algorithm, whereas they compared the output of the algorithm with the identification of the mechanisms performed by experts. Apart from different technical implementations and study designs, it was very satisfactory to find out

that both studies corroborated the robustness of directed network and network theory to characterize atrial arrhythmia and its various mechanisms.

Other approaches to understand cardiac arrhythmias, based on network theory, are vastly distinct and mostly applied for AF characterization. For example, using high density contact mapping, directed networks were applied to describe AF by identifying recurring wavefront propagation patterns [142]. AF was also described with a directed network applying sparse modeling for the estimation of propagation patterns [143]. Directed arrows can also be created based on the concept of Granger causality between different signals [144, 145]. This approach could be an alternative way to generate the network, but it requires implementing a linear multivariate autoregressive model instead of deriving the activation times. Studies on undirected networks exist too. For example, in one study the network was created by quantifying the similarity between EGMs collected at different locations [146]. Features from the network were then extracted and used to distinguish between SR and AF. In another study, authors used mutual information between pairs of nodes to build the network [147]. Authors found that successful AF ablations led to networks with a higher connectivity with respect to unsuccessful ones. Overall, the use of directed network mapping, or in general network theory, to characterize the electrical propagation has several advantages with respect to a LAT map. In particular, it opens up to a whole new field of automated analyses. For example, the identification of reentries and focal points can be automatically and quickly performed, thus promoting a faster inspection of the ongoing arrhythmia.

We used unipolar EGMs as input to the directed network mapping. The major disadvantage of unipolar EGMs is that they also record substantial far-field ventricular signal, which interferes with the atrial activity. Because of the susceptibility to noise and far-field potentials, unipolar EGMs are not often used in clinical practice, leading to the routine use of bipolar EGMs [85]. However, bipolar EGMs can be sensitive to wavefront direction, bipole orientation, electrode size, interelectrode spacing, and the exact spatial location of the measurement is less precise [84, 148]. Therefore, assessment of the exact LAT based on bipolar EGMs

can introduce ambiguity, especially in low-voltage EGMs with multiple peaks [149]. To overcome the problem of far-field ventricular signal in unipolar EGMs, many different cancellation techniques have been developed, as discussed in Chapter 3. Even though we used r-ABS method that showed good performance, this methods still require signal acquisitions from several seconds to minutes, during which the catheter must be held still, and it was applied offline. Signal acquisitions should be repeated after each change of catheter position, which prolongs the procedure to obtain state of the art map densities (more than 15000 points on average [150]), even if simultaneous wall contact of at least 20 electrodes per mapping position is assumed. For that reason, there is a need to process the signals faster in real-time. During the last years some significant steps forward were taken in this direction [151, 152]. For example, Frisch et al. proposed to model the ventricular activity acquired at different locations during mapping and interpolate the voltage in locations not visited by the catheter [151]. The main assumptions were that the ventricular activity varies smoothly across the atrial surface and that the atrial activity is not overlapped to the ventricular one (or, at least, uncorrelated). In this way, the model could be used afterwards to remove the ventricular activity.

The most common method to detect the existence of a cycle in directed networks is using DFS, by finding an edge that points to an ancestor of the current vertex (it contains a back edge). Since we are employing DFS and looking at all the vertices along with their edges, for each node in the network the 1-edge gap algorithm has a runtime of $O(V + E)$ with a space complexity of $O(V + E)$ as well, where $V$ is the number of nodes and $E$ is the number of edges. The computational time required to build the directed network and to find the cycles was approximately 5 minutes computed on a MacBook Pro 2.3 GHz 8-Core Intel Core i9 16 GB 2667 MHz DDR4 for a mapping phase lasting on average 20 minutes, without an optimized code.

# 5 Ablation Recommender System

## Contents



Planning the optimal ablation strategy for the treatment of complex atrial arrhythmias can be a time consuming task and is error-prone. In this chapter, the potential of network theory in supporting the planning of the ablation treatment is presented. An ablation recommender system is proposed, built as a solution of an optimization problem. Specifically, here we define "support" as suggesting a set of possible ablation lines suitable to terminate reentrant activities, recommended automatically by a computer program.

The problem was designed on top of directed network mapping, described in the previous chapter. The optimization problem modeled the optimal ablation strategy as that one interrupting all reentrant mechanisms while minimizing the ablated atrial

surface. Considering the exponential complexity of finding the optimal solution of the problem, a heuristic algorithm with polynomial complexity is introduced. The algorithm has been tested on computerized electro-anatomical simulations of LA and RA under different arrhythmia patterns. Then, data from EP studies collected during catheter ablations were employed to evaluate the performance of the proposed algorithm. The algorithm made use of only data collected during mapping and was able to process them nearly real-time.

## 5.1 Modeling the ablation strategy with graph theory

The output of the directed network mapping, as described in Chapter 4, comprised two networks, i.e., the directed network resembling the electrical propagation $G_{\text{prop}} = (V_{\text{prop}}, E_{\text{prop}})$ and the undirected network describing the triangular mesh $G_{\text{mesh}} = (V_{\text{mesh}}, E_{\text{mesh}})$. Two networks shared the same nodes, i.e., $V_{\text{prop}} = V_{\text{mesh}}$. Figure 5.1a depicts an example of both networks.

### 5.1.1 Ablation lines as paths on a graph

The networks $G_{\text{prop}}$ and $G_{\text{mesh}}$ could be leveraged to study the effect of ablation lines on the atrial tissue. To do so, a third undirected network $G_{\text{lines}} = (V_{\text{lines}}, E_{\text{lines}})$ derived from $G_{\text{mesh}}$ was first built as follows. Each triangle in the mesh was used to create the set of nodes $V_{\text{lines}}$. In other words, each triangle in the mesh defined a specific node in $V_{\text{lines}}$. The position of these nodes on the atrial model was defined as the centroid of each triangle. For a triplet of nodes in $V_{\text{mesh}}$, $i$, $j$ and $z$ with $j, z \in \mathcal{B}_i, i \neq j \neq z$, the position was $(\mathbf{p}_i + \mathbf{p}_j + \mathbf{p}_z)/3$.

The edges $E_{\text{lines}}$ were created by connecting nodes of $V_{\text{lines}}$ of adjacent triangles (i.e., triangles sharing two nodes). The resulting graph was a Voronoi tessellation built on top of the triangular mesh $G_{\text{mesh}}$. This graph represents a reticulum of all possible ablation lines. In other words, an ablation line was then defined as a path on $G_{\text{lines}}$. Figure 5.1b shows the reticulum of all possible ablation lines.

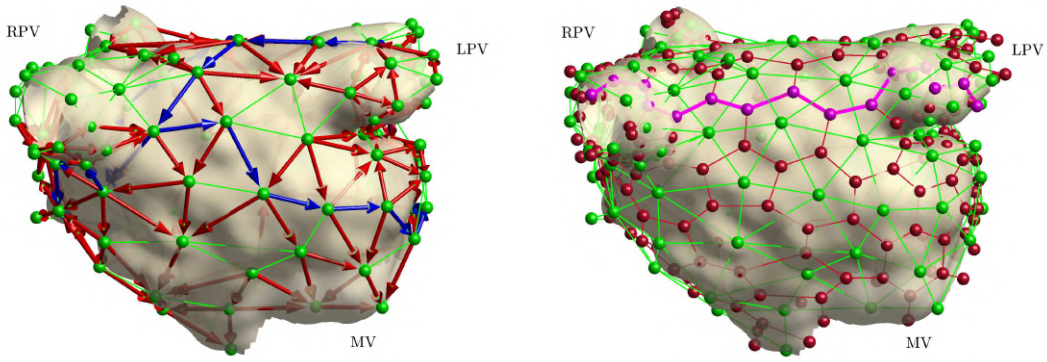


**(a)** **(b)**

**Figure 5.1:** **(a)** Example of implementation of directed network mapping. Green spheres represent the nodes distributed on the atrial mesh while the green lines are the edges connecting neighboring nodes. Spheres and lines construct the graph $G_{\text{mesh}}$. Red arrows indicate the directed connection between two neighboring nodes as a model of electrical propagation. Spheres and arrows represent the graph $G_{\text{prop}}$. Blue arrows represent the macroreentries identified as they show a cycle. **(b)** The Voronoi tessellation $G_{\text{lines}}$ (red), built on top of $G_{\text{mesh}}$ (shown in green), is reported as red spheres and red lines. The purple line represents an example of an ablation line traversing along the edges of the Voronoi tessellation. The atrial model is the clinical case 9 of Table 4.2

The Voronoi tessellation contained all possible ablation lines lying within the atrial surface but not touching the boundaries of the model. In other words, no line was actually interrupting the electrical propagation traveling along anatomical regions such as mitral valve, PVs, etc., due to the fact that the regions were on the boundaries of the anatomical model. In order to equip the reticulum with ablation lines possibly interrupting such electrical propagations, all nodes on the free boundaries were identified. Then, for each triangle having two nodes located on a free boundary, a new node was added in $V_{\text{lines}}$ and its position was mirrored with respect to the centroid of the triangle. The total number of nodes of $G_{\text{lines}}$ was $M_A$. An example of these nodes is reported in the lower part of Figure 5.1b.

Another important aspect for the addition of new nodes in $V_{\text{lines}}$ was the possibility to determine which nodes in $V_{\text{mesh}}$ were located on the valves and PVs. This was achieved by identifying the connected components in the graph built only using the nodes of the free boundaries. The association between the

nodes in the free boundary and the added nodes in $V_{\text{lines}}$ was then straightforward. Associating the correct anatomical structure (e.g., mitral valve) to a connected component was done by visual inspection.

The main advantage of this procedure is that each edge in $G_{\text{lines}}$ crosses exactly one edge on $G_{\text{mesh}}$ and this property was leveraged to determine whether an ablation line would interrupt a cycle in $G_{\text{prop}}$. In particular, we were able to define the function

$$cut1edge : (e_a, e_m) \in E_{\text{lines}} \times E_{\text{mesh}} \rightarrow \{0, 1\} \tag{5.1}$$

where the value of the function $cut1edge$ is 1 when the edge $e_a$ in $E_{\text{lines}}$ cuts the edge $e_m \in E_{\text{mesh}}$, otherwise 0.

Among all possible paths on the Voronoi tessellation, we considered the ablation lines with the shortest path between each pair of nodes belonging to the i) MV and left PVs; ii) MV and right PVs; iii) left PVs and right PVs for the LA; and for the RA iv) IVC and SVC; v) IVC and TV; and vi) SVC and TV.

### 5.1.2 Recommender system as optimization problem

In this section, we describe the algorithm to recommend ablation lines suitable to interrupt all reentry activities identified as cycles.

All identified cycles were stored as a set

$$\mathcal{L} = \{L_1, L_2, \ldots, L_{\#\mathcal{L}}\} \tag{5.2}$$

where $\#\mathcal{L}$ is the total number of cycles and each $L_i$ is a directed graph containing only one cycle. The number of nodes of each $L_i$ is $M_i$ (built upon $G_{\text{mesh}}$).

All possible ablation lines were stored as a set

$$\mathcal{A} = \{A_1, A_2, \ldots, A_{\#\mathcal{A}}\} \tag{5.3}$$

where $\#\mathcal{A}$ is the total number of ablation lines and each $A_i$ is an undirected graph containing only one ablation line. The number of nodes of each $A_i$ is $M_A$ (built upon $G_{\text{lines}}$).

We denote the graphs of a specific cycle $L_j$ and ablation line $A_i$ as $(V_{\text{prop}}(L_j), E_{\text{prop}}(L_j))$ and $(V_{\text{lines}}(A_i), E_{\text{lines}}(A_i))$, respectively.

The main objective was to find the optimal set of ablation lines to stop the arrhythmia. We considered the set able to interrupt all cycles in $\mathcal{L}$ with minimum ablation length as optimal.

The optimization problem was designed as follows. First, let us define $\mathcal{C} \subseteq \mathcal{A}$ (e.g., $\mathcal{C} = \{A_2, A_5, A_8\}$) as the set representing all possible candidate ablation lines. From this candidate set, the overall ablation length was defined as follows. Considering that the elements of $\mathcal{A}$ are all graphs, each $A_i$ has its associated set of edges $E_{A_i}$. Let then construct the set of edges $E_{\mathcal{C}}$, as follows:

$$E_{\mathcal{C}} = \bigcup_{A_i \in \mathcal{A}} E_{A_i} \tag{5.4}$$

The edge set $E_{\mathcal{C}}$ contained the edges of all $A_i$.

The overall ablation line length was then defined as

$$l_{\mathcal{C}} = \sum_{e \in E_{\mathcal{C}}} d(e) \tag{5.5}$$

where $d(e)$ is the length of edge $e$ in mm.

The second step of the algorithm was to define how many cycles were interrupted by the candidate set $\mathcal{C}$. To do so, by leveraging the Voronoi reticulum previously created, it was possible to define a function *cut* that indicated whether a given ablation line $A$ would interrupt a certain loop $L$, as follows.

$$cut : (A, L) \rightarrow \{0, 1\} \tag{5.6}$$

where the output of 1 means interruption, 0 otherwise. Formally, if $\exists (e_A, e_L) \in E_{\text{lines}}(A) \times E_{\text{prop}}(L)$ such that $cut1edge(e_A, e_L) = 1$, then the output was set to 1. Using this function, it was possible to define an additional set $\mathcal{T}_A$ containing all cycles interrupted by a given ablation line $A$, as follows

$$\mathcal{T}_A = \{L : L \in \mathcal{L}, cut(A, L) = 1\} \tag{5.7}$$

By leveraging this set, the number of cycles interrupted by the ablation lines stored in the candidate set $\mathcal{C}$ can be defined as

$$r_{\mathcal{C}} = \# \left( \bigcup_{A \in \mathcal{C}} \mathcal{T}_A \right) \tag{5.8}$$

Finally, the overall optimization problem was defined as

$$\begin{array}{ll} \text{find all sets} & \mathcal{C} \\ \text{that minimize} & l_{\mathcal{C}} \\ \text{subject to} & r_{\mathcal{C}} = \#\mathcal{L} \end{array} \tag{5.9}$$

### 5.1.3 Efficient solution via heuristic algorithm

The number of possible candidate set $\mathcal{C}$ for the problem in (5.9) is large and grows exponentially with the number of ablation lines in $\mathcal{A}$. Precisely,

$$\sum_{k=1}^{\#\mathcal{A}} \binom{\#\mathcal{A}}{k} = 2^{\#\mathcal{A}} - 1. \tag{5.10}$$

The computational complexity $\mathcal{O}(2^{\#\mathcal{A}})$ suggested that enumerating all possible solutions and evaluating them according to (5.9) was feasible only for a low number of ablation lines.

We developed a heuristic that can guide the identification of an optimal candidate set when the number of ablation lines is large. The main idea of the algorithm is to add one optimal ablation line at a time to a set of already established ones using an iterative approach, with an initially empty set. Then, the optimization problem was solved by splitting it into two sequential problems. The first ones determines the subset of all candidates (including the previously selected lines) that maximizes the number of cycles interrupted. Then, among the candidates of the subset, the candidate adding the shortest ablation line to the overall ablated surface is selected (in case of multiple candidates, tough very unlikely, a random ablation line was selected among those with equal performance).

The algorithm was stopped when at least one candidate set $\mathcal{C}^*$ interrupted all cycles or when a maximum number of ablation lines, here called "depth", was reached. Using this approach, the number of candidates $\mathcal{C}$ to evaluate reduces heavily to

$$\sum_{i=0}^{\text{depth}-1} (\#\mathcal{A} - i) = \frac{\text{depth}\,(2\#\mathcal{A} - \text{depth} + 1)}{2} \tag{5.11}$$

that reached $\#\mathcal{A}(\#\mathcal{A}+1)/2$ when depth $= \#\mathcal{A}$. The complexity of the heuristic-based algorithm is polynomial, i.e., $\mathcal{O}(\#\mathcal{A}^2)$ (or $\mathcal{O}(\#\text{depth}^2)$).

Algorithm 1 reports the pseudocode of the algorithm.

**Algorithm 1** Pseudocode of the proposed heuristic aiming to recommend the ablation strategy.

**Require:** $\mathcal{A}$, $\mathcal{L}$, depth $\in \mathbb{N}_+$
  $\mathcal{C}^* \leftarrow \{\}$
  $i \leftarrow 1$
  **while** $r_{\mathcal{C}^*} < \#\mathcal{L}$ **and** $i \leq$ depth **do**
    $\mathcal{P} \leftarrow \{\mathcal{C} : \mathcal{C} \subseteq \mathcal{A}, \#\mathcal{C} = i, \mathcal{C}^* \subseteq \mathcal{C}\}$
    $\mathcal{P}^{\max} \leftarrow \underset{\mathcal{C}\in\mathcal{P}}{\operatorname{argmax}}\, r_{\mathcal{C}}$
    **if** $\exists \mathcal{C} \in \mathcal{P}^{\max}$ **having** $r_{\mathcal{C}} == r_{\mathcal{C}^*}$ **then**
      **Exit**
    **end if**
    $\mathcal{P}^{\max/\min} \leftarrow \underset{\mathcal{C}\in\mathcal{P}^{\max}}{\operatorname{argmin}}\, l_{\mathcal{C}}$
    $\mathcal{C}^* \leftarrow$ **random pick from** $\mathcal{P}^{\max/\min}$
    $i \leftarrow i + 1$
  **end while**

## 5.2 Validation of recommender system

### 5.2.1 Simulations

We validated the recommender system in simulated arrhythmia scenarios of atrial flutter (AFL). To do so, we retrospectively analyzed 6 different simulated AFL mechanisms [126]. These simulations included both right and left forms of AFL, such as macroreentries around the valves and across the roof. A complete list of scenarios is provided in Table 4.1, in Chapter 4.

The objective of the simulations was the verification that the recommended ablation lines would stop the AFL mechanism in place. To do so, the recommender system was run and then the optimal ablation lines were identified on $G_{\text{lines}}$. Each line $A \in \mathcal{C}^*$ was then projected on the original atrial mesh by identifying the nearest node from each one in $V_{\text{lines}}(A)$. The boundary nodes of $A$ were then connected to the closest node belonging to one of the anatomical structures (identified again with the free boundary algorithm). All nodes were connected using the shortest path algorithm. The respective ablation lines identified were then virtually applied to each of the 6 AFL scenarios to verify the interruption of the AFL mechanism. Interruption of the mechanism was considered successful if 3 s after the application of

the ablation line the electrical propagation had ceased. Simulations were generated as described in Section 4.5 of Chapter 4.

### 5.2.2 Clinical cases

The recommender system was tested on 10 clinical cases which were described in Section 4.6 of Chapter 4. Each case was analyzed offline, after the intervention, by directed network mapping to create the propagation network. Macroreentries were identified using the algorithm tolerant to one missed edge, and only cycles having $\geq 10$ nodes (average length $\geq 136\,\text{mm}$) were considered as macroreentries. The recommender system was then employed to recommend the set of ablation lines needed to interrupt all cycles.

The performance of the recommender system was assessed by visual inspection of the ablation lines suggested. In case the lines were located in the expected anatomical position according to the guidelines for the treatment of the atrial arrhythmia mechanism in place, the recommendation was considered correct.

It is worth noting that the case 6 presented only microreentries around the PVs. Instead of excluding this case, we wanted to assess the potential of our algorithm for the recommendation of ablation lines suitable for microreentries as well. To do so, we first identified microreentries using the DFS algorithm without tolerance on missing edges (see Section. 4.1 of Chapter 4), with cycles containing less than 10 nodes. Regarding the set $\mathcal{A}$ of ablation lines, we identified all ablation paths between nodes of the Voronoi tessellation that were no more than 3 nodes away from the free boundaries of the PVs. Recommendations were obtained for case 6 on this set of ablation lines.

Table 4.2 reports the list of all cases analyzed with the algorithm.

### 5.2.3 Results

Directed network mapping was performed on the simulated AFL episodes using the updated algorithm. In all scenarios, the mechanism was properly identified. The recommended ablation lines for the scenarios from 3 to 6, i.e., mitral valve and

figure-of-eight macroreentries, successfully interrupted the mechanism. The first and second, i.e., tricuspid valve macroreentries, converted into a biatrial AFL.

Directed network mapping was computed for all clinical cases, as described in Chapter 4. Figure 5.2 and Figure 5.3 show the macroreentries identified and ablation lines recommended for clinical cases, while Table 5.1 reports a summary of the results. Among all cycles in a given group, only the cycle having the minimum average Menger curvature is plotted.

The first two clinical cases (1 and 2) were typical counterclockwise AFL with a critical inferior turning point between the TV and the IVC known as the CTI. Directed network mapping detected two cycle groups for both cases, a cycle group around the TV and another one around the IVC. The numbers of all possible ablation lines were 271 and 255, respectively. The optimal ablation line for both cases was along the CTI. The lengths of the optimal ablation lines were 28 mm (case 1) and 31 mm (case 2). Figures 5.2a and b report the results of cases 1 and 2.

Cases 4 and 5 displayed left atrial reentries around the mitral valve in clockwise direction. In both cases, a single group of cycles around the MV was found by directed network mapping. The numbers of all possible ablation lines were 584 and 454, respectively. The optimal ablation line for both cases was the line connecting the mitral valve with the left PVs, which is called endocardial mitral isthmus line (MIL). The lengths of the optimal ablation lines were 38 mm for case 4 and 62 mm for case 5. Figures 5.2d and e show the cycles identified and ablation lines recommended for these two cases, respectively.

Case 6 had microreentries due to gaps in the previous PVI, in both left and right PVs. Directed network mapping detected 4 cycles, with either 3 or 4 nodes, belonging to two different groups: one group near the left superior PV and the other one near the right inferior PV. The number of ablation lines was 3315. The ablation lines identified were two: one for each left and right PVs. These ablation lines pointed to the possible gaps in the previous PVI ablation. Figure 5.2f reports the results for case 6.

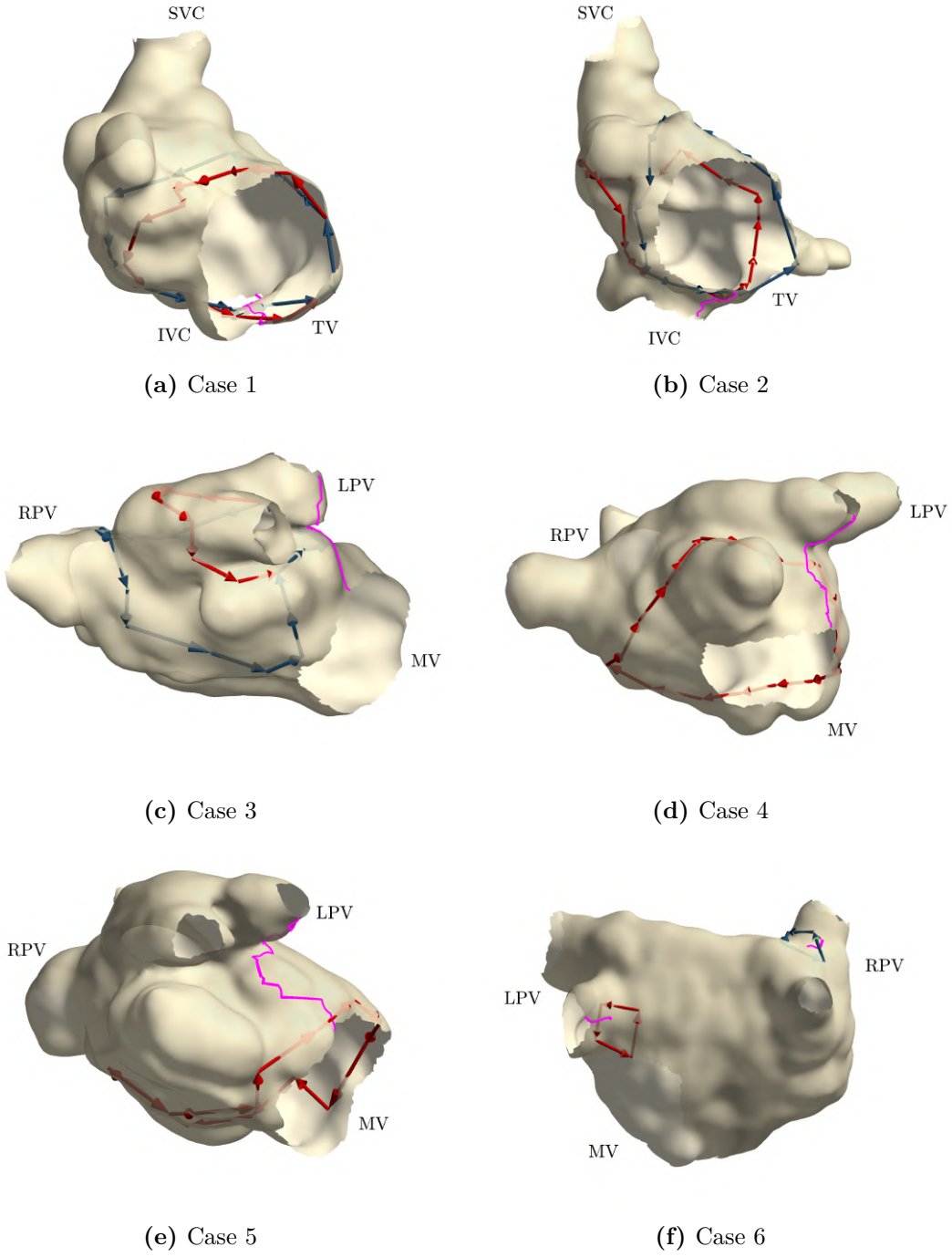


**(a)** Case 1 **(b)** Case 2

**(c)** Case 3 **(d)** Case 4

**(e)** Case 5 **(f)** Case 6

**Figure 5.2:** Results of the recommender system for 6 clinical cases. Arrows depict the reentry identified by directed network mapping with arrow colors representing cycles of different groups. Among all cycles in a group, only the one with a minimum average Menger curvature is reported. The purple line represents the recommended ablation line. Panels a), b), c), d), e) and f) correspond to case 1, 2, 3, 4, 5 and 6 of Table 4.2.

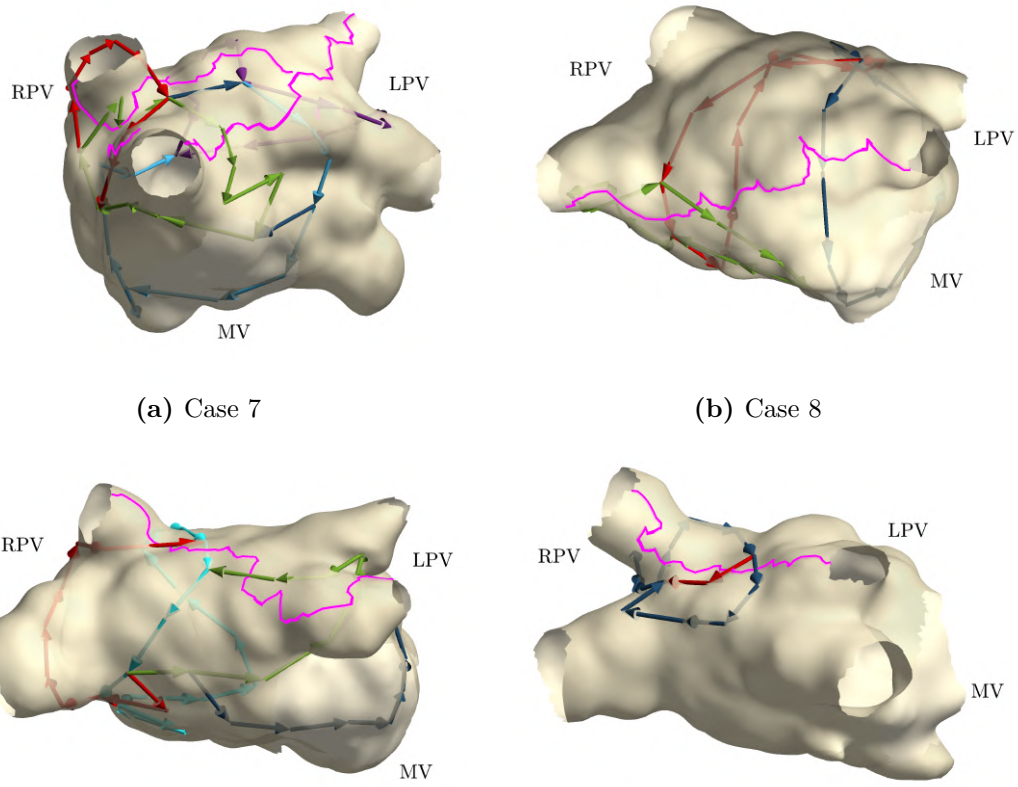


**(a)** Case 7 **(b)** Case 8

**(c)** Case 9 **(d)** Case 10

**Figure 5.3:** Results of the recommender system for 4 clinical cases. Arrows depict the reentry identified by directed network mapping with arrow colors representing cycles of different groups. Among all cycles in a group, only the one with a minimum average Menger curvature is reported. The purple line represents the recommended ablation line. Panels a), b), c) and d) correspond to case 7, 8, 9 and 10 of Table 4.2.

Case 7 displayed a figure-of-eight macroreentry around both left and right PVs. Figure-of-eight was properly identified, with additional cycles with $\geq 10$ nodes found traveling around both right PVs individually, as stated in Chapter 4. The number of ablation lines was 503. The optimal ablation line for this case connected the left PVs to both right PVs using two paths (see Figure 5.3a). The length of overall ablation line was 172 cm.

Cases 8 and 9 had confirmed figure-of-eight macroreentries. In both cases, directed network mapping correctly detected the propagation pattern around the PVs. The number of ablation lines were 668 and 479 for cases 8 and 9, respectively. The optimal ablation line for both cases was the one connecting the left pair of

**Table 5.1:** Summary of the results for the clinical cases. Values in parentheses for the group column indicate the number of cycle groups identified with the algorithm without tolerance regarding a single missing edge. For case 6, † refers to results related to microreentries.

| No. | $\#\mathcal{L}$ | $\#\mathcal{L}_{1-gap}$ | #groups | $\#\mathcal{A}$ | $\#\mathcal{C}^*$ | $l_{\mathcal{C}^*}$ (mm) | Time (s) |
|---|---|---|---|---|---|---|---|
| 1 | 4 | 46 | 2(1) | 271 | 1 | 28 | 5.9 |
| 2 | 13 | 183 | 2 | 255 | 1 | 31.2 | 34.5 |
| 3 | 0 | 20 | 2 | 614 | 1 | 36.3 | 8.8 |
| 4 | 0 | 17 | 1 | 584 | 1 | 37.7 | 8.2 |
| 5 | 0 | 9 | 1 | 454 | 1 | 61.7 | 2.2 |
| 6 | $4^\dagger$ | - | $2^\dagger$ | $3315^\dagger$ | $2^\dagger$ | $14.3^\dagger$ | $12.7^\dagger$ |
| 7 | 21 | 310 | 5(3) | 503 | 2 | 172 | 295.2 |
| 8 | 0 | 76 | 3 | 668 | 1 | 112.7 | 28.6 |
| 9 | 4 | 63 | 4(1) | 479 | 1 | 91.1 | 16.2 |
| 10 | 0 | 9 | 2 | 532 | 1 | 62.4 | 3.4 |

PVs to the right pair of PVs. The lengths of the optimal ablation lines were 113 mm for case 8 and 91 mm for case 9. Figures 5.3b and c report the results for the case 8 and 9, respectively.

Case 10 reported a macroreentry around right PVs. Here, directed network mapping found two groups of cycles, both revolving only around the right superior PV in a sort of concentric fashion. The mechanism was coherent with the identified gaps in the right PVs reported in the clinical report. The number of ablation lines was 532. The optimal ablation line connected the left pair of PVs to the right pair of PVs. The length of the line was 62 mm. Figure 5.3d reports the results for case 10.

The mechanism of case 3 was partially identified. Two groups of cycles were detected around the left PVs in counterclockwise direction but none of them was found around the MV. Despite the partial identification, we ran the recommender system in this case too. The number of all possible ablation lines was 614. A single optimal ablation line was recommended to connect the MV to the left PVs. The length of the ablation line was 36 mm. Figure 5.2c reports the results for case 3.

The execution time for running the heuristic was traced for all cases. On a MacBook Pro 2.3 GHz 8-Core Intel Core i9 16 GB 2667 MHz DDR4 using Matlab (R2021a, The MathWorks, Inc., Natick, USA), the execution time was $10.8(5.9, 28.6)$ s [median (interquartile range)].

## 5.3 Discussion

The recommender system was found able to recommend ablation lines, for the complex atrial tachycardia considered, that were partially matching those performed clinically. In particular, for the cases displaying typical AFL (case 1 and 2), the optimal ablation line was along the CTI, which is the standard treatment for typical flutter [153], and they matched what performed clinically for these two cases.

For mitral valve reentries (cases 3, 4 and 5), the recommended ablation line connected the MV with the left PVs, which is called the endocardial MIL. Also this line is what is typically performed for the treatment of this reentry [154]. Despite the mechanism of case 3 was partially detected, it is worth noting that directed network mapping correctly identified the gap in the anterior block line, that was responsible for the mechanism in place, as described in Section 4.8 of Chapter 4. The ablation line recommended was resembling the MIL at the posterior mitral isthmus, that is considered a conventional MIL [154]. Similar results were obtained for case 4 and 5 in which MILs to left superior PV and left inferior PV were recommended. Despite these lines were coherent with the mechanism, the treatment that stopped the reentry in cases 3 and 4 involved the closing of the gap in the MIL previously performed from the MV to the left superior PV. For case 5, the recommendation was correct. Furthermore, anterior MIL is typically preferred over the posterior one since it is easier to achieve a bidirectional block with a lower length of the MIL [154]. However, the length of the line depends on the specific patient's anatomy and other factors, such as the thickness of the myocardium and closeness to other anatomical structures, may play a role for the selection of what line to perform [155]. Therefore, the modeling of previous ablated tissue, thickness of the myocardium and preferences of ablation strategies in the optimization problem may

represent additional steps to further improve the performance of the recommender system. We leave this investigation for future works.

For the figure-of-eight cases (7, 8, 9), the optimal line was the one connecting left and right PVs, resembling a roof line, a floor line or a combination of the two. Case 7 was found to require the most complicated ablation strategy according to our algorithm. In fact, the figure-of-eight mechanism also involved gaps in the previous PVI on the right PVs. Directed network mapping identified a reentry on each right PV. However, only a reentry on the right inferior PV was clinically observed. The mechanism was stopped by performing a roof line. In addition, PVI was also repeated. Despite the recommended strategy may look overly complicated, a closer inspection hints that a roof line and PVI on the right PVs were the necessary lines and matched with the actual ablation. The mechanism of the case 8 was stopped with a roof line, which matched to the recommended strategy. Regarding case 9, the patient had gaps in the previous PVIs which their closing caused the termination of the mechanism. In addition, a roof line was performed to ensure a successful intervention, that matched the recommendation.

Case 10 presented a macroreentry around the right PVs due to a gap in the previous line connecting the MV and right superior PV. When the gap was ablated, the mechanism stopped. In this case, the recommended line resembled a roof line and it was the shortest single path terminating the arrhythmia according to our algorithm. This case opens up to an interesting discussion. Indeed, the antero-medial line connecting the right PV and MV typically shows large lengths [155], and thus it likely becomes excluded from the set of eligible lines by the heuristic implemented. In addition, this line is close to the aortic sinus, which requires attention when ablating along this isthmus: the critical position of other structures was a property not modeled in our optimization problem. For this specific case, with a proper modeling of previous ablations, the recommended line would have been the closing of the gap as optimal strategy.

Finally, the recommended lines for the case displaying microreentries (case 6) were two short paths interrupting the cycles appearing on both left and right

PVs. Despite the recommender system being designed only for the treatment of macroreentries, we wanted to evaluate the potential for microreentries too. For this case, however, the ablation lines found need to be considered as only indications for the necessary treatment, and not for their exact location. In fact, interrupting any edge composing the cycle would stop the microreentry. Gaps were found during the intervention on both left and right PVIs very near to the mechanisms identified by directed network mapping. However, only the gaps on the left PVI resulted in an observed microreentry. The microreentry identified on the right PVI was mostly located within the RSPV and was likely caused by a combination of factors such as the gap on the right PVI and the substrate of the previously ablated tissue. The clinical treatment was the closing of the gaps in both left and right PVIs, as indicated by the interruption of the microreentries provided by the recommender system. Further investigations are needed in this context.

One key assumption of our methodology was that ablation lines could only stop the mechanism in place but not changing it. However, this assumption might not hold in practice and for this reason we implemented computerized simulations to assess such possible switch of the mechanism. Out of the six simulations considered, only the scenarios involving typical atrial flutter switched into a biatrial flutter. Biatrial tachycardia is considered a rare form of reentrant arrhythmia and is found associated with scars on the septum [156]. Such scars create a block of the electrical propagation between the left and right atria, thus promoting a reentry traveling from the right to the left atrium through the CS, and from the left to the right atrium through the Bachmann's bundle on the way back (or viceversa). We noted that the ablation recommended was very close to the septum due to the particular position of the IVC in this reconstructed anatomy (please, refer to Figure 4.4 in Section 4.8 to inspect the 3D model). Likely, the position of the line in combination with this specific anatomy caused the switch into a biatrial flutter.

The performance of the recommender system can be summarized under different perspectives. First, the position of the recommended lines matched what typically expected by the mechanism in place in 89% of the cases (cases from 1-5 and 7-9; case

6 excluded). Second, the suggested lines exactly matched the clinical treatment in 44% (cases 1, 2, 7, 8), and partially matched in 22% (cases 5 and 9). Hence, accuracy ranged between 44% to 67% with the actual treatment. The drop in performance was associated to the lack of modeling of the previous ablated tissue (cases 3, 4, 9, 10) into the optimization problem and the selection of the left inferior PV instead of left superior PV when performing a MIL (case 5). Third, the recommended lines terminated the mechanism in 67% of the simulated scenarios (however, we believe that this percentage is underestimated considering that the wrong recommendation was for a rare form of arrhythmia in a single anatomy considered).

Another point worth discussing was that the recommended ablation lines displayed a "zig-zag" behavior with both low and high spatial frequency oscillations (e.g., see Figure 5.3b). The low oscillations were mostly due to the strategy used for the creation of the Voronoi tessellation. Indeed, the use of the centroid in each of the triangles composing the downsampled mesh forced the ablation path to circumnavigate the nodes where the electrical potentials were quantified (see Figure 5.1b). This behavior can be solved by i) forcing the downsampling algorithm to produce a denser distribution of nodes; or ii) adding points within each triangle where the ablation path could go through. In our opinion, both strategies have advantages and disadvantages. In fact, adding nodes to $G_{\text{prop}}$ might compromise the detection of cycles due to higher chances of missing edges (similar to what is described above), while adding points for ablation lines would make $\#\mathcal{A}$ grow drastically, thus increasing the computational time required to find the optimal ablation set. Regarding the high spatial frequency oscillations, they are mostly due to the way the ablation lines were projected from the Voronoi tessellation to the original mesh. We believe that this is a minor problem that can be easily solved by smoothing the line using a low pass filter or a geometric snake for a triangular mesh [157, 158]. We leave these investigations and improvements for future works.

Despite our study reports the first attempt for the use of graph theory to recommend the ablation strategy from data collected during interventions, at the best of our knowledge, only one study investigated a similar approach [119].

Zahid et al. proposed to use the "minimum cut" algorithm based on a flow network to predict optimal ablation targets for left AFL. They used data collected from EP studies and magnetic resonance imaging to create a mathematical model, comprising a geometry annotated with both healthy and fibrotic tissues, and a cellular model, to simulate the electrical propagation. A flow network was constructed on simulated data considering each volumetric element of the geometry as a node, and connecting adjacent nodes only when the conduction velocity was higher than a certain threshold (they used 100 cm/s). Once the network was created, the "minimum cut" algorithm was employed to interrupt the mechanisms.

The "minimum cut" algorithm is the dual problem of the so-called "maximum flow" problem, common in network theory. Briefly, this problem requires the assignment of a maximum capacity to each edge of a graph. The maximum flow from one node, called source, to another one, called sink, is computed as the maximum sum of the flows between all paths connecting the source and sink, according to the maximum capacity of each edge (a clear example is the road network from one city to another one where each road has a maximum capacity of cars). Finding the maximum flow between two nodes is equivalent of identifying the minimum sum of the flows through the edges that, when removed, would separate the network into two disjoint networks (in the road example is equivalent to finding the bottleneck during traffic jam).

There are three major differences between our approach and that of Zahid et al. The first one is that all algorithms we proposed are based only on data collected during mapping and do not require computerized simulations. This is clearly advantageous under different perspectives. On the one hand, directed network mapping and recommender system require only two important assumptions: i) stationary electrical propagation; and ii) conduction velocity within a physiological range. Both assumptions are also required by the flow network implemented by Zahid et al., but with additional requirements such as availability of imaging data, and electrophysiological model of atrial cells and model of fiber orientation, specifically fitted on patient's data. Also, results can be obtained fully automatic and

nearly real-time with our approach, while computerized simulations are (typically) computationally expensive. On the other hand, the main drawback of the recommender system is that the mechanism may turn into a more complicated pattern after performing the suggested ablation lines (as it occurred in our simulations of typical AFL). In this case, being able to simulate beforehand the effect of the recommended ablations using advanced computational models seems a reasonable and feasible approach to further improve the performance.

The second difference is that the "minimum cut" algorithm needs the selection of the source and sink, i.e., two nodes of the network. This selection represents a major difficulty and can completely change the output of the algorithm, i.e., the ablation strategy recommended. In fact, the source and sink are typically inputs of the optimization problem. However, we found no criteria for the a priori selection of these two nodes considering the physiological phenomenon in place.

Finally, the third major difference is that there is no guarantee that the set of minimum cuts would resemble the ablation lines established for the treatment of complex atrial tachycardia. Indeed, the noise present on the recordings may make the nodes of the network with a low degree, i.e., just a few edges inward and outward to and from a node. Hence, the noise will likely lead the minimum cut algorithm to find a set of ablation lines, as short as one edge, that are disconnected between each other, for the treatment of macroreentries.

# 6 Conclusions

## Contents



Successful catheter ablation is dependant on appropriate mapping to determine arrhythmia mechanism. Development of techniques to map regular cycle length arrhythmia have resulted in improved procedural outcome, but such advances have not been observed with atrial fibrillation (AF), where ablation beyond PVI has not consistently been shown to improve long term outcomes. The population of patients suffering from AF is expected to significantly increase over the coming years, and the number of patients requiring catheter ablation will substantially grow. Consequently, an efficient and reliable mapping procedure is of fundamental importance.

A literature review, in Chapter 1, has identified some of the significant challenges that exist when attempting to map AF and some of the existing techniques that have caused great controversy. Despite decades of attempts to understand the underlying mechanisms of AF, evidence to confirm or disprove several suggested mechanisms is still lacking. The intention of this thesis was to develop a new

automated techniques which enable atrial arrhythmias, specifically AF and AFL, to be mapped in order to understand the mechanisms that maintain them. The eventual goal is to utilize this understanding to improve catheter ablation outcome with a patient tailored approach. It is hoped that these contributions will help to advance the quality of treatment that patients receive in the future.

## 6.1 Original Contributions

The main novelties of this work were: (i) a new algorithm for ventricular activity cancellation in atrial signals, (ii) a directed network mapping technique to describe and characterize cardiac arrhythmias, (iii) an ablation strategy recommender system for the treatment of atrial arrhythmia.

### 6.1.1 Ventricular Activity Cancellation

We have introduced a new signal processing approach to remove the far-field activity present in atrial EGMs recorded during AF, by refining the ventricular activity estimate provided by the ABS using maximum a posteriori estimation. The novel cancellation method has been tested on both synthetic and real AF EGMs. We have compared its performance using various metrics to other existing methods that have been extensively used in studies, and generally it achieved better results. In conclusion, we feel that this work opens a new perspective in the cancellation of ventricular activity in atrial signals during AF, and we believe that the proposed algorithm should be considered when the atrial activity can be properly modeled with a stationary stochastic Gaussian process. As unipolar atrial signals get highly degraded by ventricular activity, in this thesis this was the important preliminary step for further processing of these signals and the creation of directed networks.

### 6.1.2 Directed Network Mapping

Using network theory to characterize cardiac excitation represents an innovative and promising tool that has the potential to be used in an EP study for the treatment of atrial arrhythmias. In cases when the physician cannot unequivocally identify

the driving mechanism using the LAT map and where several hypotheses can be formulated, directed network mapping could aid the operators by showing existing cycles in the network, possibly associated with conduction pathways sustaining AFL. In addition, this technology, along with dedicated visualization techniques, may represent an novel way to report the physicians an overall description of the arrhythmias in place, and speed up the planning of the ablation therapy.

### 6.1.3 Ablation Recommender System

We proposed a recommender system, built as solution of an optimization problem, able to suggest the optimal ablation strategy for the treatment of atrial arrhythmia. The problem was designed on top of directed network mapping used to model the electrical propagation, based on network theory. The optimization problem modeled the optimal ablation strategy as that one interrupting all reentrant mechanisms while minimizing the ablated atrial surface. Considering the exponential complexity of finding the optimal solution of the problem, we introduced a heuristic algorithm with polynomial complexity. The proposed algorithm was applied to both simulated and clinical data, achieving promising performance, nearly real-time. The study may open up interesting scenarios for the application of network theory for the treatment of atrial arrhythmia.

## 6.2 Future Directions

The current directed network mapping approach is a proof-of-concept. Many different clinical settings are not yet tested. It remains to be seen how the networks will characterize cardiac excitation in very complex clinical cases, for example with multiple rotors, or in a very fibrotic tissue. A possible limitation is that sequential mapping may fail to capture important dynamic changes in atrial electrophysiology when the arrhythmia is not stationary. In this proof-of-concept, we analyzed the entire mapping procedure, thus assuming arrhythmia as stationary. This simplification might have led to spurious connections, possibly mitigated by the averaging network procedure put in place. Although the method does not

require sequential mapping by itself, it is the predominantly available technology at present, and so we relied on that.

Another important extension of our method could be the conversion of the directed network into a weighted directed network by assigning a weight to each edge. The weight could be the level of "fractionation", the conduction velocity, or other important features for the mechanism undergoing. This new approach requires a completely new set of algorithms where it is necessary to assign a physiological meaning on cycles built on edges with weights. However, this is not straightforward in our opinion, hence we leave this for future investigations. Yet, we believe that together with an appropriate colormap, the visualization may become more informative and support better the planning of the optimal ablation.

The next step for directed network mapping, should be analyzing clinical AF cases. So far we only tested it in a computational 3D model of human atria in which sustained rotor activation was present. The main goal was to assess the potential of directed network mapping to characterize AF, and to use it for rotor detection. Additionally, in another recent study, the authors showed that graph based mapping can overcome some of the limitations of phase mapping, by being able to exclude the false rotors that phase mapping generates [159]. The next important step in this direction is to analyze clinical AF cases.

Regarding the ablation recommender system, the association between anatomical structures, such as valves, appendage and PVs, and nodes on the free boundaries was the only step not performed automatically by our software. This problem was tackled recently by means of different tools such as machine learning [160] or statistical shape models [161]. Since this step was not the main objective of the study, we leave the insertion of this automatic association in the overall pipeline as future works.

The set of ablation lines was restricted to those from one anatomical structure to another one in both atria. However, this approach might be suboptimal in case of previous PVI (as in our case) because the ablated tissue is not considered in the optimization problem. Here, we had no information about the exact position of the previous PVI on the mesh, hence we employed the free boundaries. This

lack of information might have led the recommender system to suggest longer ablation lines that what actually needed, e.g., not connecting PVIs from left to right PVs for the treatment figure-of-eight macroreentries (see case 9 in Figure 5.3c)). The influence of ablated tissue on the recommended ablation strategy will be investigated in the future.

Another important limitation is that we did not consider focal activations in the optimization problem. Despite directed network mapping seems able to identify such activations by looking at the in-degree of the nodes [121], modeling how they should be handled by the recommender system is challenging. In the current framework, the most straightforward way would be considering closed-loop ablations placed around each node in the propagation graph and let the recommender finding the optimal solution. However, this approach may contrast with the optimization problem designed specifically for macroreentries. In fact, the algorithm could find many of these closed-loop ablations simply because they tend to reduce the overall ablation length while removing macroreentries as well. A similar problem occurs when dealing with microreentries. We leave the investigation on how to handle focal activations and microreentries in the optimization problem for future.

Finally, the recommender system could be extended to consider additional criteria rather than just the length of the ablation line. For example, ablating in diseased areas (identified as areas with low bipolar voltage, reduced conduction velocity or late gadolinium enhancement [162]) might be preferred to ablating nearby healthy tissue. This may lead, for example, to preferring an anterior MIL to a lateral MIL [163].

# Bibliography


[1] World Health Organization. *Cardiovascular diseases*. URL: `https://www.who.int/news-room/fact-sheets/detail/cardiovascular-diseases-(cvds)` (visited on 01/06/2022).

[2] G. Hindricks et al. "2020 ESC Guidelines for the diagnosis and management of atrial fibrillation developed in collaboration with the European Association for Cardio-Thoracic Surgery (EACTS)". In: *European Heart Journal* 42.5 (Feb. 2021), pp. 373–498.

[3] B. P. Krijthe et al. "Projections on the number of individuals with atrial fibrillation in the European Union, from 2000 to 2060". In: *European Heart Journal* 34.35 (Sept. 2013), pp. 2746–2751.

[4] M. Velleca et al. "A Review of the Burden of Atrial Fibrillation: Understanding the Impact of the New Millennium Epidemic across Europe". In: *European Medical Journal* (Oct. 2019).

[5] H. Calkins et al. "2017 HRS/EHRA/ECAS/APHRS/SOLAECE expert consensus statement on catheter and surgical ablation of atrial fibrillation: Executive summary". In: *EP Europace* 20.1 (Jan. 2018), pp. 157–208.

[6] A. Chugh et al. "Prevalence, mechanisms, and clinical significance of macroreentrant atrial tachycardia during and following left atrial ablation for atrial fibrillation". In: *Heart Rhythm* 2.5 (May 2005), pp. 464–471.

[7] G. Lee, P. Sanders, and J. M. Kalman. "Catheter ablation of atrial arrhythmias: state of the art". In: *The Lancet* 380.9852 (Oct. 2012), pp. 1509–1519.

[8] L. Rottner et al. "Catheter Ablation of Atrial Fibrillation: State of the Art and Future Perspectives". In: *Cardiology and Therapy* 9.1 (June 2020), pp. 45–58.

[9] K. T. Konings et al. "High-density mapping of electrically induced atrial fibrillation in humans." In: *Circulation* 89.4 (Apr. 1994). Publisher: American Heart Association, pp. 1665–1680.

[10] K.T.S. Konings et al. "Configuration of Unipolar Atrial Electrograms During Electrically Induced Atrial Fibrillation in Humans". In: *Circulation* 95.5 (Mar. 1997). Publisher: American Heart Association, pp. 1231–1241.

[11] J. Jalife. "Rotors and Spiral Waves in Atrial Fibrillation". In: *Journal of Cardiovascular Electrophysiology* 14.7 (2003), pp. 776–780.

[12] H. J. Sih. "Measures of organization during atrial fibrillation". eng. In: *Annali dell'Istituto Superiore Di Sanita* 37.3 (2001), pp. 361–369.

[13] V. Barbaro et al. "Extraction of physiological and clinical information from intra-atrial electrograms during atrial fibrillation: review of methods". In: *Annali dell'Istituto Superiore Di Sanita* 37.3 (2001), pp. 319–324.

[14] J. G. Quintanilla et al. “Mechanistic Approaches to Detect, Target, and Ablate the Drivers of Atrial Fibrillation”. In: *Circulation: Arrhythmia and Electrophysiology* 9.1 (Jan. 2016).

[15] G. La Rosa et al. “Mapping Technologies for Catheter Ablation of Atrial Fibrillation Beyond Pulmonary Vein Isolation”. In: *European Cardiology Review* 16 (May 2021), e21.

[16] P. Lee et al. “Low-Cost Optical Mapping Systems for Panoramic Imaging of Complex Arrhythmias and Drug-Action in Translational Heart Models”. en. In: *Scientific Reports* 7.1 (Mar. 2017), p. 43217.

[17] D. Filgueiras-Rama et al. “Long-Term Frequency Gradients During Persistent Atrial Fibrillation in Sheep Are Associated With Stable Sources in the Left Atrium”. In: *Circulation: Arrhythmia and Electrophysiology* 5.6 (Dec. 2012), pp. 1160–1167.

[18] M. Yamazaki et al. “Heterogeneous atrial wall thickness and stretch promote scroll waves anchoring during atrial fibrillation”. In: *Cardiovascular Research* 94.1 (Apr. 2012), pp. 48–57.

[19] S. V. Pandit and J. Jalife. “Rotors and the Dynamics of Cardiac Fibrillation”. en. In: *Circulation Research* 112.5 (Mar. 2013), pp. 849–862.

[20] M. Wellner et al. “Minimal principle for rotor filaments”. In: *Proceedings of the National Academy of Sciences* 99.12 (June 2002), pp. 8015–8018.

[21] P. Lee et al. “In vivo ratiometric optical mapping enables high-resolution cardiac electrophysiology in pig models”. In: *Cardiovascular Research* 115.11 (Sept. 2019), pp. 1659–1671.

[22] C. O’Shea et al. “Cardiac optical mapping - State-of-the-art and future challenges”. In: *The International Journal of Biochemistry & Cell Biology* 126 (Sept. 2020), p. 105804.

[23] Douglas P. Z. “Mechanisms of Clinical Arrhythmias”. In: *Journal of Cardiovascular Electrophysiology* 14.8 (July 2003), pp. 902–912.

[24] C. D. Cantwell et al. “Techniques for automated local activation time annotation and conduction velocity estimation in cardiac mapping”. In: *Computers in Biology and Medicine* 65 (Oct. 2015), pp. 229–242.

[25] S. Hinderer and K. Schenke-Layland. “Cardiac fibrosis – A short review of causes and therapeutic strategies”. In: *Advanced Drug Delivery Reviews* 146 (June 2019), pp. 77–82.

[26] S. Rolf et al. “Electroanatomical mapping of atrial fibrillation: Review of the current techniques and advances”. In: *Journal of Atrial Fibrillation* 7.4 (Dec. 2014), p. 1140.

[27] I. Sim et al. “Left atrial voltage mapping: defining and targeting the atrial fibrillation substrate”. In: *Journal of Interventional Cardiac Electrophysiology* 56.3 (Dec. 2019), pp. 213–227.

[28] K. Nademanee et al. “A new approach for catheter ablation of atrial fibrillation: mapping of the electrophysiologic substrate”. In: *Journal of the American College of Cardiology* 43.11 (June 2004), pp. 2044–2053.

[29] S. Zlochiver et al. “Rotor meandering contributes to irregularity in electrograms during atrial fibrillation”. In: *Heart Rhythm* 5.6 (June 2008), pp. 846–854.

[30] D. D. Correa de Sa et al. “Electrogram Fractionation: The Relationship Between Spatiotemporal Variation of Tissue Excitation and Electrode Spatial Resolution”. In: *Circulation: Arrhythmia and Electrophysiology* 4.6 (Dec. 2011), pp. 909–916.

[31] T. Ashihara et al. “The Role of Fibroblasts in Complex Fractionated Electrograms During Persistent/Permanent Atrial Fibrillation: Implications for Electrogram-Based Catheter Ablation”. In: *Circulation Research* 110.2 (Jan. 2012), pp. 275–284.

[32] F. Atienza et al. “Mechanisms of Fractionated Electrograms Formation in the Posterior Left Atrium During Paroxysmal Atrial Fibrillation in Humans”. In: *Journal of the American College of Cardiology* 57.9 (Mar. 2011), pp. 1081–1092.

[33] A. Verma et al. “Approaches to Catheter Ablation for Persistent Atrial Fibrillation”. In: *New England Journal of Medicine* 372.19 (May 2015), pp. 1812–1822.

[34] K. C.K. Wong et al. “No Benefit of Complex Fractionated Atrial Electrogram Ablation in Addition to Circumferential Pulmonary Vein Ablation and Linear Ablation: Benefit of Complex Ablation Study”. In: *Circulation: Arrhythmia and Electrophysiology* 8.6 (Dec. 2015), pp. 1316–1324.

[35] Y. J. Lin et al. “Nonlinear Analysis of Fibrillatory Electrogram Similarity to Optimize the Detection of Complex Fractionated Electrograms During Persistent Atrial Fibrillation”. In: *Journal of Cardiovascular Electrophysiology* 24.3 (Mar. 2013), pp. 280–289.

[36] Y. J. Lin et al. “Benefits of Atrial Substrate Modification Guided by Electrogram Similarity and Phase Mapping Techniques to Eliminate Rotors and Focal Sources Versus Conventional Defragmentation in Persistent Atrial Fibrillation”. In: *JACC: Clinical Electrophysiology* 2.6 (Nov. 2016), pp. 667–678.

[37] O. Berenfeld et al. “Spatially Distributed Dominant Excitation Frequencies Reveal Hidden Organization in Atrial Fibrillation in the Langendorff-Perfused Sheep Heart”. In: *Journal of Cardiovascular Electrophysiology* 11.8 (Aug. 2000), pp. 869–879.

[38] F. Atienza et al. “Real-time dominant frequency mapping and ablation of dominant frequency sites in atrial fibrillation with left-to-right frequency gradients predicts long-term maintenance of sinus rhythm”. In: *Heart Rhythm* 6.1 (Jan. 2009), pp. 33–40.

[39] J. Ng and J. J. Goldberger. “Understanding and Interpreting Dominant Frequency Analysis of AF Electrograms”. In: *Journal of Cardiovascular Electrophysiology* 18.6 (June 2007), pp. 680–685.

[40] K. Umapathy et al. “Phase Mapping of Cardiac Fibrillation”. In: *Circulation: Arrhythmia and Electrophysiology* 3.1 (Feb. 2010), pp. 105–114.

[41] J. Chen. “Dynamics of wavelets and their role in atrial fibrillation in the isolated sheep heart”. In: *Cardiovascular Research* 48.2 (Nov. 2000), pp. 220–232.

[42] C. Y. Lin et al. “Comparison of phase-mapping and electrogram-based driver mapping for catheter ablation in atrial fibrillation”. In: *Pacing and Clinical Electrophysiology* (Dec. 2018), pace.13573.

[43] M. Haissaguerre et al. “Driver Domains in Persistent Atrial Fibrillation”. In: *Circulation* 130.7 (Aug. 2014), pp. 530–538.

[44] S. M. Narayan et al. “Treatment of atrial fibrillation by the ablation of localized sources: CONFIRM (Conventional Ablation for Atrial Fibrillation With or Without Focal Impulse and Rotor Modulation) trial”. In: *Journal of the American College of Cardiology* 60.7 (Aug. 2012), pp. 628–636.

[45] T. Nitta et al. “Concurrent multiple left atrial focal activations with fibrillatory conduction and right atrial focal or reentrant activation as the mechanism in atrial fibrillation”. In: *The Journal of Thoracic and Cardiovascular Surgery* 127.3 (Mar. 2004), pp. 770–778.

[46] N.M.S. De Groot et al. “Electropathological Substrate of Longstanding Persistent Atrial Fibrillation in Patients With Structural Heart Disease: Epicardial Breakthrough”. In: *Circulation* 122.17 (Oct. 2010), pp. 1674–1682.

[47] G. Lee et al. “Epicardial wave mapping in human long-lasting persistent atrial fibrillation: transient rotational circuits, complex wavefronts, and disorganized activity”. In: *European Heart Journal* 35.2 (Jan. 2014), pp. 86–97.

[48] W. J. Rappel and S. M. Narayan. “Theoretical considerations for mapping activation in human cardiac fibrillation”. In: *Chaos: An Interdisciplinary Journal of Nonlinear Science* 23.2 (June 2013), p. 023113.

[49] J. M. Miller et al. “Initial independent outcomes from focal impulse and rotor modulation ablation for atrial fibrillation: multicenter FIRM registry”. In: *Journal of Cardiovascular Electrophysiology* 25.9 (Sept. 2014), pp. 921–929.

[50] K. Shivkumar et al. “Acute termination of human atrial fibrillation by identification and catheter ablation of localized rotors and sources: first multicenter experience of focal impulse and rotor modulation (FIRM) ablation”. In: *Journal of Cardiovascular Electrophysiology* 23.12 (Dec. 2012), pp. 1277–1285.

[51] J. S. Steinberg et al. “Focal impulse and rotor modulation: Acute procedural observations and extended clinical follow-up”. In: *Heart Rhythm* 14.2 (Feb. 2017), pp. 192–197.

[52] B. Bellmann et al. “Identification of active atrial fibrillation sources and their discrimination from passive rotors using electrographical flow mapping”. In: *Clinical Research in Cardiology: Official Journal of the German Cardiac Society* 107.11 (Nov. 2018), pp. 1021–1032.

[53] J. Seitz et al. “AF Ablation Guided by Spatiotemporal Electrogram Dispersion Without Pulmonary Vein Isolation: A Wholly Patient-Tailored Approach”. In: *Journal of the American College of Cardiology* 69.3 (Jan. 2017), pp. 303–321.

[54] S. Honarbakhsh et al. “Development, in vitro validation and human application of a novel method to identify arrhythmia mechanisms: The stochastic trajectory analysis of ranked signals mapping method”. In: *Journal of Cardiovascular Electrophysiology* 30.5 (May 2019), pp. 691–701.

[55] S. Choudry et al. “RADAR: A Multicenter Food and Drug Administration Investigational Device Exemption Clinical Trial of Persistent Atrial Fibrillation”. In: *Circulation. Arrhythmia and Electrophysiology* 13.1 (Jan. 2020), e007825.

[56] M. S. Guillem et al. “Noninvasive localization of maximal frequency sites of atrial fibrillation by body surface potential mapping”. In: *Circulation. Arrhythmia and Electrophysiology* 6.2 (Apr. 2013), pp. 294–301.

[57] M. Rodrigo et al. “Body surface localization of left and right atrial high-frequency rotors in atrial fibrillation patients: a clinical-computational study”. In: *Heart Rhythm* 11.9 (Sept. 2014), pp. 1584–1591.

[58] M. J. M. Cluitmans et al. “In Vivo Validation of Electrocardiographic Imaging”. In: *JACC. Clinical electrophysiology* 3.3 (Mar. 2017), pp. 232–242.

[59] L. R. Bear et al. “How Accurate Is Inverse Electrocardiographic Mapping? A Systematic In Vivo Evaluation”. In: *Circulation. Arrhythmia and Electrophysiology* 11.5 (May 2018), e006108.

[60] H. S. Oster et al. “Electrocardiographic imaging: Noninvasive characterization of intramural myocardial activation from inverse-reconstructed epicardial potentials and electrograms”. In: *Circulation* 97.15 (Apr. 1998), pp. 1496–1507.

[61] C. Ramanathan et al. “Noninvasive electrocardiographic imaging for cardiac electrophysiology and arrhythmia”. In: *Nature Medicine* 10.4 (Apr. 2004), pp. 422–428.

[62] P. S. Cuculich et al. “Noninvasive characterization of epicardial activation in humans with diverse atrial fibrillation patterns”. In: *Circulation* 122.14 (Oct. 2010), pp. 1364–1372.

[63] H. Pereira, S. Niederer, and C. A. Rinaldi. “Electrocardiographic imaging for cardiac arrhythmias and resynchronization therapy”. In: *EP Europace* 22.10 (Aug. 2020), pp. 1447–1462.

[64] Texas Heart Institute. *Heart anatomy*. URL: `https://www.texasheart.org/heart-health/heart-information-center/topics/heart-anatomy/` (visited on 01/06/2022).

[65] R. Jaeschke. *McMaster textbook of internal medicine 2019/20*. Kraków, Poland: Medycyna Praktyczna, 2019.

[66] L. Sörnmo and P. Laguna. *Bioelectrical Signal Processing in Cardiac and Neurological Applications*. Elsevier Academic Press, 2005.

[67] N. L. Ko Ko et al. “Atypical atrial flutter: review of mechanisms, advances in mapping and ablation outcomes”. In: *Current Opinion in Cardiology* 37.1 (Jan. 2022), pp. 36–45.

[68] Borys Surawicz and Timothy K. Knilans. *Chou’s Electrocardiography in Clinical Practice*. Elsevier, 2008.

[69] A. M. Patel et al. “Atrial tachycardia after ablation of persistent atrial fibrillation: identification of the critical isthmus with a combination of multielectrode activation mapping and targeted entrainment mapping”. In: *Circulation. Arrhythmia and Electrophysiology* 1.1 (Apr. 2008), pp. 14–22.

[70] G. Moubarak et al. “Incidence of atrial fibrillation during very long-term follow-up after radiofrequency ablation of typical atrial flutter”. In: *Archives of Cardiovascular Diseases* 102.6-7 (July 2009), pp. 525–532.

[71] A. L. Waldo and G. K. Feld. “Inter-relationships of atrial fibrillation and atrial flutter mechanisms and clinical implications”. In: *Journal of the American College of Cardiology* 51.8 (Feb. 2008), pp. 779–786.

[72] Y. Hung et al. “Atrial Tachycardias After Atrial Fibrillation Ablation: How to Manage?” In: *Arrhythmia & Electrophysiology Review* 9.2 (Aug. 2020), pp. 54–60.

[73] U. Schotten et al. “Pathophysiological mechanisms of atrial fibrillation: a translational appraisal”. In: *Physiological Reviews* 91.1 (Jan. 2011), pp. 265–325.

[74] G.K. Moe and J.A. Abildskov. “Atrial fibrillation as a self-sustaining arrhythmia independent of focal discharge”. In: *American Heart Journal* 58.1 (July 1959), pp. 59–70.

[75] J. L. Cox et al. “Successful surgical treatment of atrial fibrillation. Review and clinical update”. In: *JAMA* 266.14 (Oct. 1991), pp. 1976–1980.

[76] M. Haïssaguerre et al. “Spontaneous initiation of atrial fibrillation by ectopic beats originating in the pulmonary veins”. In: *The New England Journal of Medicine* 339.10 (Sept. 1998), pp. 659–666.

[77] C. Pappone et al. “Circumferential radiofrequency ablation of pulmonary vein ostia: A new anatomic approach for curing atrial fibrillation”. In: *Circulation* 102.21 (Nov. 2000), pp. 2619–2628.

[78] L. Gepstein, G. Hayam, and S. A. Ben-Haim. “A novel method for nonfluoroscopic catheter-based electroanatomical mapping of the heart. In vitro and in vivo accuracy results”. In: *Circulation* 95.6 (Mar. 1997), pp. 1611–1622.

[79] C. Knackstedt, P. Schauerte, and P. Kirchhof. “Electro-anatomic mapping systems in arrhythmias”. In: *Europace: European Pacing, Arrhythmias, and Cardiac Electrophysiology: Journal of the Working Groups on Cardiac Pacing, Arrhythmias, and Cardiac Cellular Electrophysiology of the European Society of Cardiology* 10 Suppl 3 (Nov. 2008), pp. iii28–34.

[80] Z. F. Issa, J. M. Miller, and D. P. Zipes. *Clinical Arrhythmology and Electrophysiology*. Elsevier, 2019.

[81] S. K. S. Huang and J. M. Miller. *Catheter Ablation of Cardiac Arrhythmias*. Elsevier, 2020.

[82] Y.H. Kim et al. “2019 APHRS expert consensus statement on three-dimensional mapping systems for tachycardia developed in collaboration with HRS, EHRA, and LAHRS”. In: *Journal of Arrhythmia* 36.2 (Mar. 2020), pp. 215–270.

[83] U. B. Tedrow and W. G. Stevenson. “Recording and interpreting unipolar electrograms to guide catheter ablation”. In: *Heart Rhythm* 8.5 (May 2011), pp. 791–796.

[84] G. Ndrepepa et al. “Activation time determination by high-resolution unipolar and bipolar extracellular electrograms in the canine heart”. In: *Journal of Cardiovascular Electrophysiology* 6.3 (Mar. 1995), pp. 174–188.

[85] W. G. Stevenson and K. Soejima. "Recording techniques for clinical electrophysiology". In: *Journal of Cardiovascular Electrophysiology* 16.9 (Sept. 2005), pp. 1017–1022.

[86] C. Schmitt, I. Deisenhofer, and B. Zrenner. *Catheter Ablation of Cardiac Arrhythmias*. Steinkopff-Verlag, 2006.

[87] J. G. Andrade. "Cryoablation for atrial fibrillation". In: *Heart Rhythm O2* 1.1 (Apr. 2020), pp. 44–58.

[88] D. Shah. "Electrophysiological evaluation of pulmonary vein isolation". In: *Europace* 11.11 (Nov. 2009), pp. 1423–1433.

[89] S. Shkurovich, A.V. Sahakian, and S. Swiryn. "Detection of atrial activity from high-voltage leads of implantable ventricular defibrillators using a cancellation technique". In: *IEEE Transactions on Biomedical Engineering* 45.2 (Feb. 1998), pp. 229–234.

[90] L. Faes et al. "A method for quantifying atrial fibrillation organization based on wave-morphology similarity". In: *IEEE transactions on bio-medical engineering* 49.12 Pt 2 (Dec. 2002), pp. 1504–1513.

[91] R. P. M. Houben and M. A. Allessie. "Processing of intracardiac electrograms in atrial fibrillation. Diagnosis of electropathological substrate of AF". In: *IEEE engineering in medicine and biology magazine: the quarterly magazine of the Engineering in Medicine & Biology Society* 25.6 (Dec. 2006), pp. 40–51.

[92] V. D. A. Corino et al. "Ventricular activity cancellation in electrograms during atrial fibrillation with constraints on residuals' power". In: *Medical Engineering & Physics* 35.12 (Dec. 2013), pp. 1770–1777.

[93] J. L. Salinet et al. "Analysis of QRS-T subtraction in unipolar atrial fibrillation electrograms". In: *Medical & Biological Engineering & Computing* 51.12 (Dec. 2013), pp. 1381–1391.

[94] P. Bonizzi et al. "Ventricular activity residual reduction in remainder ECGs based on short-term autoregressive model interpolation". In: *2009 36th Annual Computers in Cardiology Conference (CinC)*. ISSN: 2325-8853. Sept. 2009, pp. 813–816.

[95] A. Ahmad et al. "QRS subtraction for atrial electrograms: flat, linear and spline interpolations". In: *Medical & Biological Engineering & Computing* 49.11 (Nov. 2011), pp. 1321–1328.

[96] B. Abdi et al. "Ventricular Activity Signal Removal in Atrial Electrograms of Atrial Fibrillation". In: Mar. 2022, pp. 179–184.

[97] M. Stridh and L. Sörnmo. "Spatiotemporal QRST cancellation techniques for analysis of atrial fibrillation". In: *IEEE transactions on bio-medical engineering* 48.1 (Jan. 2001), pp. 105–111.

[98] C. Vásquez et al. "Atrial activity enhancement by Wiener filtering using an artificial neural network". In: *IEEE transactions on bio-medical engineering* 48.8 (Aug. 2001), pp. 940–944.

[99] J. J. Rieta and F. Hornero. "Comparative study of methods for ventricular activity cancellation in atrial electrograms of atrial fibrillation". In: *Physiological Measurement* 28.8 (Aug. 2007), pp. 925–936.

[100] A. Petrėnas et al. “An echo state neural network for QRST cancellation during atrial fibrillation”. In: *IEEE transactions on bio-medical engineering* 59.10 (Oct. 2012), pp. 2950–2957.

[101] E. K. Roonizi and R. Sassi. “An Extended Bayesian Framework for Atrial and Ventricular Activity Separation in Atrial Fibrillation”. In: *IEEE journal of biomedical and health informatics* 21.6 (Nov. 2017), pp. 1573–1580.

[102] L. Sörnmo. *Atrial Fibrillation from an Engineering Perspective*. Springer, 2018.

[103] G. D. Clifford, F. Azuaje, and P. McSharry. *Advanced Methods And Tools for ECG Data Analysis*. USA: Artech House, Inc., 2006.

[104] S. M. M. Martens et al. “A robust fetal ECG detection method for abdominal recordings”. In: *Physiological Measurement* 28.4 (Apr. 2007), pp. 373–388.

[105] E. Bataillou et al. “Weighted averaging using adaptive estimation of the weights”. In: *Signal Processing* 44.1 (June 1995), pp. 51–66.

[106] M. W. Rivolta, R. Sassi, and M. Vila. “Refined Ventricular Activity Cancellation in Electrograms During Atrial Fibrillation by Combining Average Beat Subtraction and Interpolation”. In: *Annual International Conference of the IEEE Engineering in Medicine and Biology Society. IEEE Engineering in Medicine and Biology Society. Annual International Conference* 2019 (July 2019), pp. 24–27.

[107] M. Valinoti et al. “Towards a repository of synthetic electrograms for atrial activation detection in atrial fibrillation”. In: *Computers in Biology and Medicine* 101 (Oct. 2018), pp. 229–235.

[108] A. L. Goldberger et al. “PhysioBank, PhysioToolkit, and PhysioNet: components of a new research resource for complex physiologic signals”. In: *Circulation* 101.23 (2000), e215–e220.

[109] R. Sassi, V. D. A. Corino, and L. T. Mainardi. “Analysis of surface atrial signals: time series with missing data?” In: *Annals of Biomedical Engineering* 37.10 (Oct. 2009), pp. 2082–2092.

[110] G. W. Botteron and J. M. Smith. “A technique for measurement of the extent of spatial organization of atrial activation during atrial fibrillation in the intact human heart”. In: *IEEE transactions on bio-medical engineering* 42.6 (June 1995), pp. 579–586.

[111] K. M. Ropella et al. “The coherence spectrum. A quantitative discriminator of fibrillatory and nonfibrillatory cardiac rhythms”. In: *Circulation* 80.1 (July 1989), pp. 112–119.

[112] H. J. Sih et al. “A frequency domain analysis of spatial organization of epicardial maps”. In: *IEEE transactions on bio-medical engineering* 42.7 (July 1995), pp. 718–727.

[113] H. J. Sih et al. “A high-temporal resolution algorithm for quantifying organization during atrial fibrillation”. In: *IEEE transactions on bio-medical engineering* 46.4 (Apr. 1999), pp. 440–450.

[114] F. Censi et al. “Non-linear coupling of atrial activation processes during atrial fibrillation in humans”. In: *Biological Cybernetics* 85.3 (Sept. 2001), pp. 195–201.

[115] L. T. Mainardi et al. “Linear and non-linear analysis of atrial signals and local activation period series during atrial-fibrillation episodes”. In: *Medical & Biological Engineering & Computing* 39.2 (Mar. 2001), pp. 249–254.

[116] A. Porta et al. “Conditional entropy approach for the evaluation of the coupling strength”. In: *Biological Cybernetics* 81.2 (Aug. 1999), pp. 119–129.

[117] B. P. Hoekstra et al. “Non-linear time series analysis: methods and applications to atrial fibrillation”. In: *Annali dell'Istituto Superiore Di Sanita* 37.3 (2001), pp. 325–333.

[118] M. Masè et al. “Quantification of synchronization during atrial fibrillation by Shannon entropy: validation in patients and computer model of atrial arrhythmias”. In: *Physiological Measurement* 26.6 (Dec. 2005), pp. 911–923.

[119] S. Zahid et al. “Feasibility of using patient-specific models and the "minimum cut" algorithm to predict optimal ablation targets for left atrial flutter”. In: *Heart Rhythm* 13.8 (Aug. 2016), pp. 1687–1698.

[120] N. Vandersickel et al. “Directed Networks as a Novel Way to Describe and Analyze Cardiac Excitation: Directed Graph Mapping”. In: *Frontiers in Physiology* 10 (2019), p. 1138.

[121] M. Vila et al. “Directed Network Mapping Approach to Rotor Localization in Atrial Fibrillation Simulation”. In: *2021 43rd Annual International Conference of the IEEE Engineering in Medicine Biology Society (EMBC)*. ISSN: 2694-0604. Nov. 2021, pp. 730–733.

[122] M. Vila et al. “Atrial Flutter Mechanism Detection Using Directed Network Mapping”. In: *Frontiers in Physiology* 12 (2021), p. 749635.

[123] A. Neic et al. “Automating image-based mesh generation and manipulation tasks in cardiac modeling workflows using Meshtool”. In: *SoftwareX* 11 (Jan. 2020), p. 100454.

[124] D. Harrild and C. Henriquez. “A computer model of normal conduction in the human atria”. In: *Circulation Research* 87.7 (Sept. 2000), E25–36.

[125] Y. Jiang et al. “An impedance-based catheter positioning system for cardiac mapping and navigation”. In: *IEEE transactions on bio-medical engineering* 56.8 (Aug. 2009), pp. 1963–1970.

[126] G. Luongo et al. “Non-Invasive Characterization of Atrial Flutter Mechanisms Using Recurrence Quantification Analysis on the ECG: A Computational Study”. In: *IEEE transactions on bio-medical engineering* 68.3 (Mar. 2021), pp. 914–925.

[127] V. Jacquemet. “An eikonal approach for the initiation of reentrant cardiac propagation in reaction-diffusion models”. In: *IEEE transactions on bio-medical engineering* 57.9 (Sept. 2010), pp. 2090–2098.

[128] J. Trächtler et al. “Virtualizing clinical cases of atrial flutter in a fast marching simulation including conduction velocity and ablation scars”. In: *Current Directions in Biomedical Engineering* 1.1 (Sept. 2015). Publisher: De Gruyter, pp. 405–408.

[129] M. W. Krueger et al. “Personalization of atrial anatomy and electrophysiology as a basis for clinical modeling of radio-frequency ablation of atrial fibrillation”. In: *IEEE transactions on medical imaging* 32.1 (Jan. 2013), pp. 73–84.

[130] A. Wachter et al. “Mesh structure-independent modeling of patient-specific atrial fiber orientation”. In: *Current Directions in Biomedical Engineering* 1.1 (Sept. 2015). Publisher: De Gruyter, pp. 409–412.

[131] A. Loewe et al. “Influence of the earliest right atrial activation site and its proximity to interatrial connections on P-wave morphology”. In: *Europace: European Pacing, Arrhythmias, and Cardiac Electrophysiology: Journal of the Working Groups on Cardiac Pacing, Arrhythmias, and Cardiac Cellular Electrophysiology of the European Society of Cardiology* 18.suppl 4 (Dec. 2016), pp. iv35–iv43.

[132] J. Malmivuo. “Volume Source and Volume Conductor”. In: *Bioelectromagnetism*. New York: Oxford University Press, 1995.

[133] A. Ferrer et al. “Detailed Anatomical and Electrophysiological Models of Human Atria and Torso for the Simulation of Atrial Activation”. In: *PloS One* 10.11 (2015), e0141573.

[134] M. Courtemanche, R. J. Ramirez, and S. Nattel. “Ionic mechanisms underlying human atrial action potential properties: insights from a mathematical model”. eng. In: *The American Journal of Physiology* 275.1 (July 1998), H301–321.

[135] G. Seemann et al. “Heterogeneous three-dimensional anatomical and electrophysiological model of human atria”. In: *Philosophical Transactions. Series A, Mathematical, Physical, and Engineering Sciences* 364.1843 (June 2006), pp. 1465–1481.

[136] J. Feng et al. “Ionic mechanisms of regional action potential heterogeneity in the canine right atrium”. In: *Circulation Research* 83.5 (Sept. 1998), pp. 541–551.

[137] E. A. Heidenreich et al. “Adaptive macro finite elements for the numerical solution of monodomain equations in cardiac electrophysiology”. In: *Annals of Biomedical Engineering* 38.7 (July 2010), pp. 2331–2345.

[138] P. Jaïs et al. “A deductive mapping strategy for atrial tachycardia following atrial fibrillation ablation: importance of localized reentry”. In: *Journal of Cardiovascular Electrophysiology* 20.5 (May 2009), pp. 480–491.

[139] R. Mantovan et al. “How small could a detectable reentrant circuit be in a localized microreentrant tachycardia?” In: *HeartRhythm Case Reports* 6.4 (Apr. 2020), pp. 222–225.

[140] E. Van Nieuwenhuyse et al. “Evaluation of Directed Graph-Mapping in Complex Atrial Tachycardias”. In: *JACC. Clinical electrophysiology* 7.7 (July 2021), pp. 936–949.

[141] S. M. Shors et al. “A method for determining high-resolution activation time delays in unipolar cardiac mapping”. In: *IEEE transactions on bio-medical engineering* 43.12 (Dec. 1996), pp. 1192–1196.

[142] S. Zeemering et al. “Identification of recurring wavefront propagation patterns in atrial fibrillation using basis pursuit”. In: *Annual International Conference of the IEEE Engineering in Medicine and Biology Society. IEEE Engineering in Medicine and Biology Society. Annual International Conference* 2013 (2013), pp. 2928–2931.

[143] U. Richter et al. “Propagation pattern analysis during atrial fibrillation based on sparse modeling”. In: *IEEE transactions on bio-medical engineering* 59.5 (May 2012), pp. 1319–1328.

[144] A. Alcaine et al. “A Multi-Variate Predictability Framework to Assess Invasive Cardiac Activity and Interactions During Atrial Fibrillation”. In: *IEEE transactions on bio-medical engineering* 64.5 (May 2017), pp. 1157–1168.

[145] D. Luengo et al. “Hierarchical Algorithms for Causality Retrieval in Atrial Fibrillation Intracavitary Electrograms”. eng. In: *IEEE journal of biomedical and health informatics* 23.1 (Jan. 2019), pp. 143–155.

[146] L. Sun et al. “A preliminary study on atrial epicardial mapping signals based on Graph Theory”. In: *Medical Engineering & Physics* 36.7 (July 2014), pp. 875–881.

[147] S. Tao et al. “Ablation as targeted perturbation to rewire communication network of persistent atrial fibrillation”. In: *PloS One* 12.7 (2017), e0179459.

[148] D. Nairn et al. “Comparison of Unipolar and Bipolar Voltage Mapping for Localization of Left Atrial Arrhythmogenic Substrate in Patients With Atrial Fibrillation”. In: *Frontiers in Physiology* 11 (2020), p. 575846.

[149] M. El Haddad et al. “Novel algorithmic methods in mapping of atrial and ventricular tachycardia”. In: *Circulation. Arrhythmia and Electrophysiology* 7.3 (June 2014), pp. 463–472.

[150] M. Takigawa et al. “Revisiting anatomic macroreentrant tachycardia after atrial fibrillation ablation using ultrahigh-resolution mapping: Implications for ablation”. In: *Heart Rhythm* 15.3 (Mar. 2018), pp. 326–333.

[151] D. Frisch et al. “Mapping and Removing the Ventricular Far Field Component in Unipolar Atrial Electrograms”. In: *IEEE transactions on bio-medical engineering* 67.10 (Oct. 2020), pp. 2905–2915.

[152] G. R. Ríos-Muñoz et al. “Real-Time Ventricular Cancellation in Unipolar Atrial Fibrillation Electrograms”. In: *Frontiers in Bioengineering and Biotechnology* 8 (2020), p. 789.

[153] F. G. Cosío. “Atrial Flutter, Typical and Atypical: A Review”. eng. In: *Arrhythmia & Electrophysiology Review* 6.2 (June 2017), pp. 55–62.

[154] T. Maurer et al. “Catheter Ablation of the Superolateral Mitral Isthmus Line: A Novel Approach to Reduce the Need for Epicardial Ablation”. In: *Circulation. Arrhythmia and Electrophysiology* 10.10 (Oct. 2017), e005191.

[155] Y. Cho et al. “The anatomical characteristics of three different endocardial lines in the left atrium: evaluation by computed tomography prior to mitral isthmus block attempt”. In: *EP Europace* 14.8 (2012), pp. 1104–1111.

[156] A. Tolat et al. “Macro-reentrant Single-loop Biatrial Flutter Appearing as Typical Atrial Flutter: Case Study and Review”. In: *J Innov Cardiac Rhythm Manage* 11.11 (2020), pp. 4306–4312.

[157] Y. Lee and S. Lee. “Geometric Snakes for Triangular Meshes”. In: *Computer Graphics Forum* 21.3 (2002), pp. 229–238.

[158] A. Loewe et al. “Patient-Specific Identification of Atrial Flutter Vulnerability-A Computational Approach to Reveal Latent Reentry Pathways”. In: *Frontiers in Physiology* 9 (2018), p. 1910.

[159] E. Van Nieuwenhuyse et al. “Directed graph mapping exceeds phase mapping in discriminating true and false rotors detected with a basket catheter in a complex in-silico excitation pattern”. In: *Computers in Biology and Medicine* 133 (June 2021), p. 104381.

[160] T. Zheng et al. “An automate pipeline for generating fiber orientation and region annotation in patient specific atrial models”. en. In: *Current Directions in Biomedical Engineering* 7.2 (Oct. 2021). Publisher: De Gruyter, pp. 136–139.

[161] C. Nagel et al. “A bi-atrial statistical shape model for large-scale in silico studies of human atria: Model development and application to ECG simulations”. In: *Medical Image Analysis* 74 (Dec. 2021), p. 102210.

[162] D. Nairn et al. *LGE-MRI for diagnosis of left atrial cardiomyopathy as identified in high-definition endocardial voltage and conduction velocity mapping.* Tech. rep. Type: article. medRxiv, Feb. 2022, p. 2022.02.02.22269817.

[163] H. Lehrmann et al. “Novel Electrocardiographic Criteria for Real-Time Assessment of Anterior Mitral Line Block: "V1 Jump" and "V1 Delay"”. In: *JACC. Clinical electrophysiology* 4.7 (July 2018), pp. 920–932.